VŠB – Technical University of Ostrava
Faculty of Electrical Engineering and Computer Science
Department of Telecommunications

Measurement of Droplets Effect on Free Space Optical Link and Mathematical Modelling of Multi-phase Flow

Měření vlivu kapek pro optický bezvlaknový spoj a matematické modelování vícefázového proudění

2018 Bc. Filip Šarlej

VŠB - Technical University of Ostrava
Faculty of Electrical Engineering and Computer Science
Department of Telecommunications

Diploma Thesis Assignment

Student: **Bc. Filip Šarlej**

Study Programme: N2647 Information and Communication Technology

Study Branch: 2612T059 Mobile Technology

Title: Measurement of Droplets Effect on Free Space Optical Link and Mathematical Modelling of Multi-phase Flow
Měření vlivu kapek pro optický bezvlaknový spoj a matematické modelování vícefázového proudění

The thesis language: English

Description:

The aim of student work is to define a multi-phase mathematical model of the water droplets influence on the free space optical link in CFD software application of ANSYS Fluent. Student will be acquainted with mathematical approaches for solving of multi-phase flow. On the basis of defined mathematical model will be evaluated critical locations, where highest concentration of water droplets occurs. Water droplets then have influence on the optical beam parameters (such as attenuation, beam deformation or beam scattering) propagating through acrylate box. For defining of simulation input parameters and creation mathematical model will be used really measured values from experimental research in laboratory conditions with different nozzle types. Experimental measurement of water droplets effect on optical free space link will be also performed by student. This task is of experimental character and obtained results might help to understand better problems connected with modeling of water droplets flow influencing optical free space link in CFD software application.

1. Literary State-of-the-Art of multiphase mathematical modeling theory for rain droplet flowing.

2. Define suitable mathematical model of multiphase flowing of rain droplet in acrylate box.

3. Application of mathematical model in case of size changing of nozzle.

4. Experimental measurement of rain droplets influence on Free Space Optical link.

References:

[1] SALEH, B. E. A. Základy fotoniky. Praha: Matfyzpress, 1995. ISBN 80-85863-00-6

[2] WILFERT, O. Optoelektronika. Elektronické skriptum. Brno: FEKT VUT v Brně, 2008.

[3] ANDREWS, L., PHILLIPS, R., HOPEN, C. Laser Beam Scintillation with Applications. Washington:SPIE Press, 2001.

[4] SHIRAI, T.; DOGARIU, A.; WOLF, E. Directionality of some model beams propagating in atmospheric turbulence. Optics Letters, 2003, Vol. 28, No. 8, pp. 610-612. ISSN 0146-9592.

[5] RICKLIN, J., C.; DAVIDSON, F., M. Atmospheric turbulence effects on a partially coherent Gaussian beam: Implications for free-space laser communication. Journal of the Optical Society of America A: Optics and Image Science, and Vision, 2002, Vol. 19, No 9, pp. 1794-1802. ISSN 1084-7529.

Extent and terms of a thesis are specified in directions for its elaboration that are opened to the public on the web sites of the faculty.

Supervisor: **Ing. Jan Látal, Ph.D.**

Date of issue: 01.09.2017

Date of submission: 30.04.2018

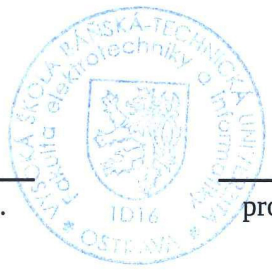

doc. Ing. Miroslav Vozňák, Ph.D.
Head of Department

prof. Ing. Pavel Brandštetter, CSc.
Dean

I hereby declare that this master's thesis was written by myself. I have quoted all the references I have drawn upon.

Ostrava, 30th April 2018 .....

I would like to thank my supervisor Ing. Jan Látal, Ph.D. for guiding and providing helpful feedback. Special thanks goes to doc. Ing. Marian Bojko, Ph.D., and Ing. Aleš Vanderka for valuable advice.

Abstract

Free space optics will emerge alongside major communications technologies as an important player in the field of wireless communications. This technology, like other technologies, has to face the challenges caused by unstable and unfavorable atmospheric conditions that determine the resulting quality of the transmitted signal. The paper is intended to determine the extent of a deterioration of the transmitted signal during rainfall. The precipitation is simulated in laboratory conditions, and the resulting knowledge of the droplet formation is transferred to a mathematical model that helps simulate multiphase flow under given conditions.

Key Words: Free Space Optics, FSO, atmosphere, rain, precipitation, optical beam, modeling, ANSYS, Fluent

Abstrakt

Optické bezvláknové spoje se v budoucnosti vyskytnou po boku majoritních komunikačních technologií jako důležitý hráč na poli bezdrátových komunikací. Tato technologie, stejně jako jiné technologie, musí čelit výzvám pramenícím z nestálých a nepříznivých atmosférických podmínek, které rozhodují o výsledné kvalitě přenášeného signálu. Tato práce má za úkol zjistit míru zhoršení přenášeného signálu během dešťových srážek. Srážkový úhrn je simulován v laboratorních podmínkách a výsledné poznatky o tvorbě dešťových kapek jsou přeneseny do matematického modelu, který napomáhá simulování vícefázového proudění v daných podmínkách.

Klíčová slova: bezvláknové optické spoje, FSO, atmosféra, déšť, srážky, optický svazek, modelování, ANSYS, Fluent

Contents

List of Abbreviations

AFGL	–	Air Force Geological Laboratory
BER	–	Bit Error Rate
BSP	–	British Standard Pipe
CFD	–	Computational Fluid Dynamics
DAQ	–	Data AcQuisition
DES	–	Detached Eddy Simulation
DNS	–	Direct Numerical Simulation
DSD	–	Drop Size Distribution
EVM	–	Eddy Viscosity Models, Error Vector Magnitude
ELES	–	Embedded Large Eddy Simulation
FSO	–	Free Space Optics
FWHM	–	Full Width at Half Maximum
IM/DD	–	Intensity-modulated/direct detection
IR	–	InfraRed
IrDA	–	Infrared Data Association
ITU-R	–	International Telecommunication Union - Radiocommunication Sector
LASER	–	Light Amplification by Stimulated Emission of Radiation
LD	–	Laser Diode
LED	–	Laser Emmiting Diode
LES	–	Large Eddy Simulation
LISA	–	Linearized Instability Sheet Atomization
LOS	–	Line-Of-Sight
MER	–	Modulation Error Ratio
NRZ	–	Non-Return-to-Zero
OOK	–	On-Off keying
OWC	–	Optical Wirelles Communication
PPM	–	Pulse Position Modulation
PSK	–	Pulse Shift Keying
PSD	–	Particle Size Distribution
QAM	–	Quadrature Amplitude Modulation
QPSK	–	Quadrature Phase Shift Keying
RANS	–	Reynolds-Averaged Navier Stokes
RF	–	Radio Frequency

RKE	–	Realizable k–ε
RNG	–	Re-Normalisation Group k–ε
RSM	–	Reynolds Stress Models
RVR	–	Runway Visual Range
RZ	–	Return-to-Zero
S-A	–	Spalart-Allmaras
SAS	–	Scale-Adaptive Simulation
SIM	–	Subcarrier Intensity Modulation
SKW	–	Standard k–ω
SNR	–	Signal to Noise Ratio
SST	–	Shear Stress Transport
SSTKW	–	Shear Stress Transport k–ω
TV	–	TeleVision
USRP	–	Universal Software Radio Peripheral
UV	–	Ultra Violet
VLC	–	Visible Light Communication

List of Symbols

Symbol	Unit/Value	Meaning
A	m^2	Area of a receiver aperture
$\bar{A}$	dB	Sample mean of attenuation
s_A	dB	Sample standard deviation of attenuation
Att_{Geo}	dB	Geometrical attenuation
B	b/s (bps)	Bit rate
c	$m.s^{-1}$	Speed of light in a medium
c_0	$\approx$ 299 700 km/s	Speed of light in free space
C_n^2	$m^{-2/3}$	Refractive index structure parameter
C_{ext}	μm^2	Extinction cross section
g	0.98 m/sec^2	Gravitational constant
$g(v)$	$1/cm^{-1}$	normalized line shape function
G_R	W	Receiver gain
G_T	W	Transmitter gain
h	$\approx 6.626 \cdot 10^{-34}$ J/s	Planck's constant
h_w	m	Height of water volume
k	$\approx 1.38 \cdot 10^{-23}$ J/K	Boltzmann's constant
k_N	m^{-1}	Wave number
l	m	Nozzle/droplet diameter
l_b	m	Lab box length
l_0	m	Optical pathlenght
L	m	Distance
m	-	Refractive index of water
M	dB	Link margin
M_T	-	Transfer matrix
n	-	Refractive index
$n(r)$	$cm^{-3}\mu m^{-1}$	Particle size distribution (PSD)
N	cm^3/atm	Number of molecules of absorbing species
N_C	$1/km^3$	Concentration of the absorbing particles
Oh	-	Ohnesorge number
P_a	atm	Partial pressure of the absorbing gas
P_e	dBm	Power of the emission signal
P_A	atm	Atmospheric pressure
P_R	mW	Signal power at the input of photodetector

Symbol	Unit/Value	Meaning
P_{Syst}	dB	System loss of the equipment
P_T	mW	Transmitter power
P_O	1013 mbar	Reference pressure
Q	l/min or kg/s	Flow rate
r	cm	Radius of raindrop
R	mm/h	Rain rate
R_0	m	Radius of curvature
Re	-	Reynolds number
s	m	Distance from the receiver along optical propagation path
S	cm/molecule	Molecular transition line intensity
S_r	cm/molecule	Receiver sensitivity
t	s	Time
T	s	Period
T_a	-	Transmittance
T_A	K	Atmospheric temperature
T_O	273.15 K	Reference temperature
v	m/s	Jet velocity
V_n	m/s	Maximum speed
V_w	m^3	Volume of water
w_b	m	Lab box width
w_0	m	Transmitter beam radius (half width)
$w(x)$	m	Half width in distance x
We	-	Weber number
z	m	Axial distance
z_R	m	Rayleigh length
β	neper/km	Volume extinction coefficient
φ	radians	Phase
κ	km^{-1}	Attenuation coefficient
κ_M	km^{-1}	Attenuation coefficient of Mie scattering
κ_R	km^{-1}	Attenuation coefficient of Rayleigh scattering
λ	m	Wavelength
η	$1.8 \cdot 10^{-4}$ g/cm	Viscosity of air
∇^2	-	Laplacian operator
μ	-	Shape parameter
μ_f	m^2/s	Dynamic viscosity of the fluid

Symbol	Unit/Value	Meaning
ν	Hz	Frequency
ν_R	-	Receiver efficiency
ν_T	-	Transmitter efficiency
ν_{TP}	-	Transmitter pointing loss factor
ω	radians.s^{-1}	Angular frequency
$\omega(l)$	m	Beam waist at distance l
ω_R	m^2	Rayleigh scattering cross section
ρ	m	Transversal distance from the beam center
ρ_W	1 g/cm^3	Water density
σ	km^2	Cross section
σ_i^2	-	Scintillation index
σ_R	m	Radial variance
τ	-	Optical depth
θ	mrad	Beam divergence

List of Figures

List of Tables

Introduction

Today, the term "wireless" is connected mainly with radio frequency (RF) technologies as a result of the deployment and utilization of RF systems spread all over the world. With the growing popularity of a data-heavy wireless communication, the RF spectrum cannot cover the increasing demand and other options have to be considered for the wireless communication, such as using upper parts of the electromagnetic spectrum - the optical band of the spectrum.

Optical wireless communication is a dynamic research and development area that has generated a plenty of interesting solutions to complicated communication challenges. For example, a high data rate, a high capacity and minimum interference links for both short-range and long-range link in the order of millions of kilometers in the new mission to Mars and other solar system planets. Optical wireless communication is one of the oldest methods that humanity has used for a communication, but nowadays offers advantages such as a high bandwidth capacity, robustness to the electromagnetic interference, inherent security, low power requirements and unregulated spectrum.

Obviously, the data rate, quality of service delivered, and transceiver technologies employed have improved from those early optical wireless technologies. In its many applications, these kinds of communication links have already succeeded in becoming part of our everyday lives in our homes and offices. Optical wireless products are already well familiar, ranging from visible-light communication (VLC), TV (TeleVision) remote control, IrDA (Infrared Data Association) ports to embedded systems and devices of all types, terrestrial and in-building optical wireless Local Area Networks, a network of sensors, inter-satellite and inter-vehicle link applications.

This thesis is aimed at measuring of effects on the free space optical link in unfavorable weather conditions - raining. The logic suggests that this atmospheric state has a negative impact for a propagating optical beam. Its parameters based on the propagation can be extremely influenced. The approach used here is, first, to set up a model of the interaction between an optical wave and the atmospheric particles, especially water droplets.

It is possible to divide the work into two parts. For simulating these effects, special-designed acrylate box with nozzles generating water droplets is used to simulate outside conditions as realistically as possible. Testing and experimental measurement is the most important part of the work to help to find out negative effects of conditions given and evaluate their influence on optical beam parameters.

The second part is focused on a modeling in ANSYS Fluent, the computational fluid dynamics (CFD) software. Values provided by measurement are set up as input parameters for the multi-phase mathematical model created in this CFD software to discover critical concentrated locations in laboratory conditions. Creating model for detection of critical areas helps to the

better understanding of processes while rain condition has the main effects. The final model can be used later for simulation of propagating optical beam in a different modeling software.

1 Atmosphere

The atmosphere is a fluid composed of gases and particles whose physical and chemical properties vary as a function of time, altitude, and geographical location. Although these properties can be highly dependent upon regional conditions, many of the optical properties of the atmosphere can be described to an adequate level by looking at the composition of so-called a *standard atmosphere* [7].

The particulates present in the Earth's atmosphere can be divided into two major classes:

- **Constituents**, i.e. the ones always present in any geographic location, though in variable concentration. Constituents are typically the gases of the Earth's atmosphere (N_2, O_2, water vapor, and others).
- **Components**, i.e. particles that can be present in the Earth atmosphere under certain weather conditions.

The density value, the size relative to the wavelength, and the probability of occurrence of the different particulates are the key impact factors on the wave propagation [1].

1.1 Structure

The atmosphere can be divided into several layers (see Figure 1.1). It is commonly recognized to divide it into troposphere, stratosphere, mesosphere, and thermosphere. Mesosphere and thermosphere together can be also referred to as an ionosphere with a different structure based on day and night [44].

1.2 Gas Concentration

The major optically active molecular constituents of the atmosphere are N_2, O_2, H_2O, and CO_2, with secondary grouping of CH_4, N_2O, CO, and O_3. The most concentrated gases of the terrestrial atmosphere are shown in Table 1.1.

1.3 Temperature

The temperature of the atmosphere varies both with seasonal changes and altitude. The temperature decreases significantly with altitude until the level of the stratosphere is reached where the temperature profile has an inflection point. The U.S. Standard Atmosphere is one of six basic atmospheric models developed by U.S. government; these different models furnish a good representation of the different atmospheric conditions which are often encountered [7].

Table 1.1: List of chosen molecular gases and their typical concentration for the ambient U.S. standard atmosphere [7].

Molecule	Concentration (Volume fraction)
N_2	0.781
O_2	0.209
H_2O	0.0775
CO_2	$3.3 \cdot 10^{-4}$
A	0.0093
CH_4	$1.7 \cdot 10^{-6}$
N_2O	$3.2 \cdot 10^{-7}$
CO	$1.5 \cdot 10^{-7}$
O_3	$2.66 \cdot 10^{-8}$ (variable)

1.4 Pressure

The pressure of the atmosphere decreases with altitude due to the gravitational pull of the Earth and the hydrostatic equilibrium pressure of the atmospheric fluid. The partial pressure of most of the major gases (N_2, O_2, CO_2, N_2O, CO, and CH_4) follows pressure profile shown in Figure 1.1. The concentration of water depends on the temperature due to freezing and is not uniformly mixed in the atmosphere. The partial pressure of ozone also varies with altitude because it is generated in the upper altitudes and near ground level by solar radiation [7].

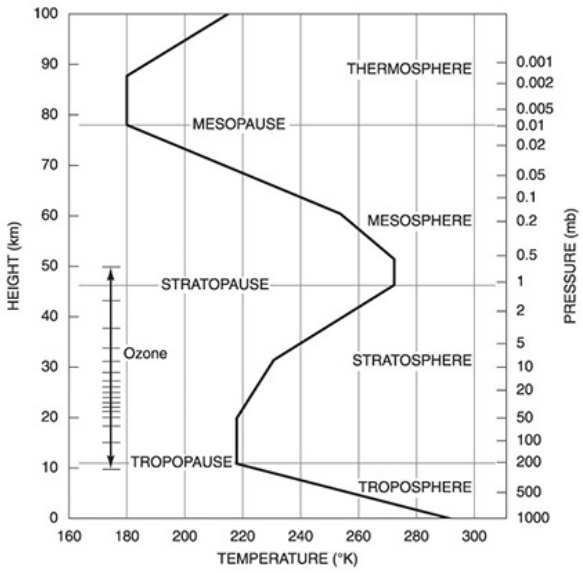

Figure 1.1: Typical vertical profiles of pressure and temperature observed in the atmosphere [7].

1.5 Components

In FSO, the most effective components are liquid and solid water particles. In propagation studies, are typically classified between:

- suspend water particles (fog, haze, ice clouds and water clouds), and
- hydrometeors (rain, snow, graupel, and hail).

Other particles as pollutants are believed to play a marginal role even in highly polluted city areas, as their concentration is not high enough to produce a significant reduction of the visibility. The occurrence of smoke, desert dust, and volcanic ash is rare and/or accidental, hence from the statistical point of view, they are not relevant unless in very specific conditions/sites [1]. The diameter classification is shown in Figure 1.2.

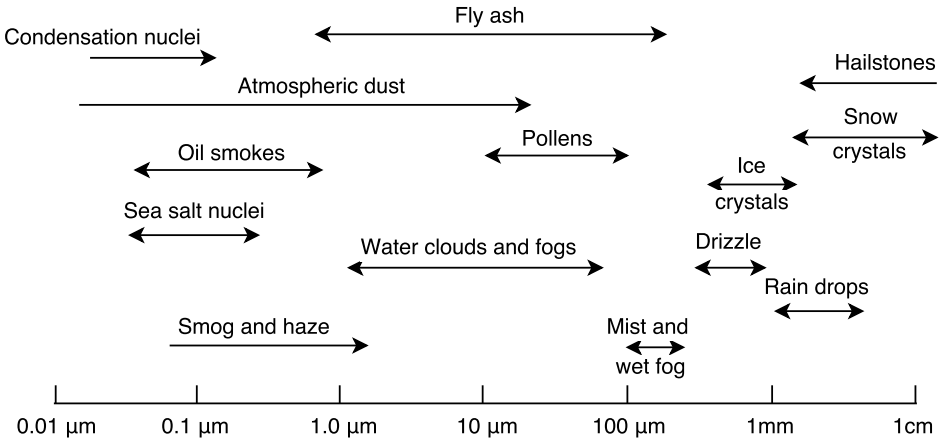

Figure 1.2: Representative diameters of common atmospheric particles [1].

2 Description of Light

The following section focuses on parts of the light description important for better understanding light behavior in free space and for purpose of the thesis - *geometrical* and *wave* optics. Gaussian beam as the basic beam model of a laser diode is described as well.

2.1 Geometrical Optics

Geometrical optics, also called ray optics, is the simplest, oldest and approximate theory of light. The light is described by rays that travel in different optical media in accordance with a set of rules. Ray optics obeys certain *postulates* [18].

- Light travels in the form of rays. The rays are emitted by light and can be observed when they reach an optical detector.

- An optical medium is characterized by a quantity $n \geq 1$, called the refractive index. The refractive index $n = c_0/c$ where c_0 is the speed of light in free space and c is the speed of light in the medium. Therefore, the time taken by light to travel a distance d is $d/c = nd/c_0$. It is proportional to the product nd, which is known as the optical pathlength.

- In an homogeneous medium the refractive index $n(r)$ is a function of the position $r = (x, y, z)$. The optical pathlength along a given path between two points A and B is therefore optical pathlength l_o is given by

$$l_o = \int_A^B n(r)ds, \tag{2.1}$$

  where ds is the differential element of length along the path. The time taken by light to travel from A to B is proportional to the optical pathlength.

- *Fermat's Principle.* Optical rays traveling between two points, A and B, follow a path such that time of travel (or the optical pathlength) between the two points is an extreme relative to neighboring paths. This is expressed mathematically as

$$\delta \int_A^B n(r)ds = 0, \tag{2.2}$$

  where δ, which is read "the variation of", means that the optical pathlength is either minimized or maximized, or is a point of inflection. It is, however, usually a minimum, in which case the light rays travel along the path of least time.

2.1.1 Reflection and Refraction

At the boundary between two media of refractive indexes n_1 and n_2 an incident ray is split into two - a reflected ray and a refracted (or transmitted) ray. The reflected ray obeys the law of reflection, where the reflected ray lies in the plane of incidence and the angle of reflection equals the angle of incidence. The refracted ray obeys the law of refraction, expressed by Snell's law (Equation 2.3). The angle of the refracted ray depends on refractive indexes of both media [18].

$$n_1 \sin\theta_1 = n_2 \sin\theta_2 \tag{2.3}$$

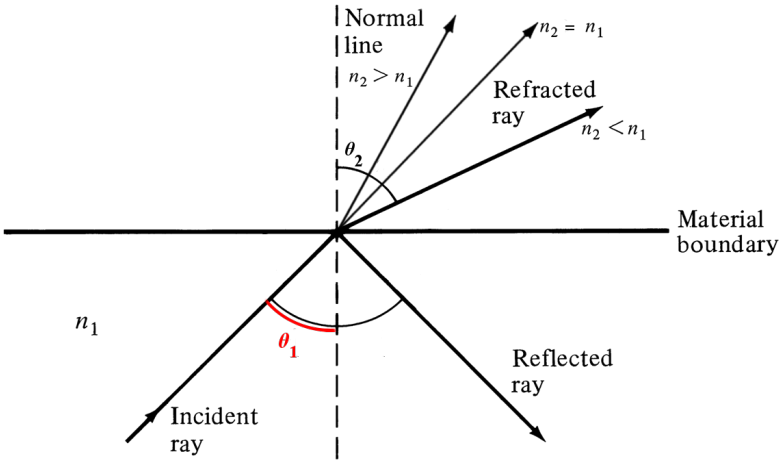

Figure 2.1: Snell's law at the boundary between two media.

2.2 Wave Optics

Light propagates in the form of waves. The wave theory encompasses and extends the geometrical theory. Geometrical optics is the limit of wave optics when the wavelength is infinitesimally short. In free space, light waves travel with a constant speed approximately $c_0 = 299\ 700$ km.s^{-1}. The range of optical wavelengths contains several regions [18]:

- infrared (0.75 to 1000 µm [47]),
- visible (380 to 750 nm),
- ultraviolet (10 to 380 nm).

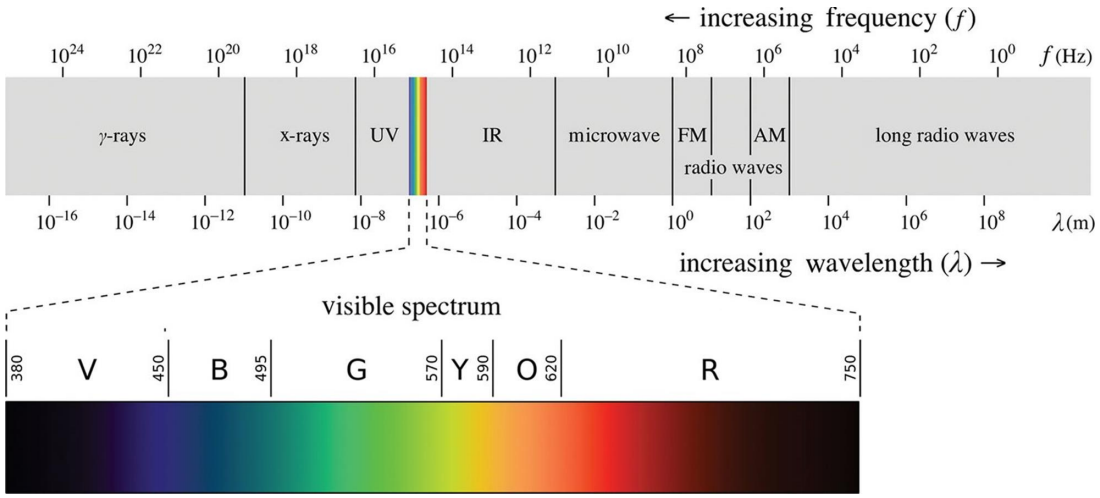

Figure 2.2: Visible part of the electromagnetic spectrum.

2.2.1 Mathematical Description

An optical wave is described mathematically by a real function of position $r = (x, y, z)$ and time t, denoted $u(r, t)$ and known as the wave function. It satisfies a partial differential equation called the wave equation

$$\nabla^2 u - \frac{1}{c^2}\frac{\delta^2 u}{\delta t^2} = 0, \tag{2.4}$$

where ∇^2 is the Laplacian operator which is $\nabla^2 = \delta^2/\delta x^2 + \delta^2/\delta y^2 + \delta^2/\delta z^2$ in Cartesian coordinates. Any function that satisfies Equation 2.4 represents a possible optical wave. At the boundary between two different media, the wave function changes in a way that depends on their refractive indexes [18].

2.2.2 Complex Refractive Index

In a medium of refractive index n, light waves travel with a reduced speed [18]

$$c = \frac{c_0}{n}. \tag{2.5}$$

When light passes through a medium, some part of it will always be attenuated. This can be conveniently taken into account by defining a *complex refractive index* [49]

$$n = \nu + i\kappa, \tag{2.6}$$

where the real part ν is the refractive index and indicates the phase velocity, and the imaginary part κ is called the extinction coefficient — although it can also refer to the mass attenuation coefficient and indicates the amount of attenuation when the electromagnetic wave propagates through the material.

2.2.3 Monochromatic Waves

A monochromatic wave is represented by a wave function with harmonic time dependence [18]

$$u(r,t) = a(r)\cos\left[2\pi\nu t + \varphi(r)\right], \tag{2.7}$$

$$U(r,t) = a(r)\exp\left[j\varphi(r)\right]\exp(j2\pi\nu t), \quad u(r,t) = Re\left\{U(r,t)\right\}, \tag{2.8}$$

where $a(r)$ is amplitude, $\varphi(r)$ is phase, ν is frequency in Hz or cycles/s, $\omega = 2\pi\nu$ is angular frequency in radians.s^{-1}, and $T = 1/\nu$ is period in seconds. The equation 2.8 is known as complex wavefunction, it describes the wave completely, where part $a(r)\exp\left[j\varphi(r)\right]$ is referred to as complex amplitude of the wave. The wavefunction $u(r,t)$ is the real part of the complex wavefunction $U(r,t)$.

Both the amplitude and phase are generally position dependent, but the wavefunction is a harmonic function of time with frequency ν at all positions. Optical waves have frequencies that lie in the range $3 \cdot 10^{11}$ to $3 \cdot 10^{16}$ Hz (see Figure 2.2).

In Figure 2.3 is shown a representation of such a wave. The case (a) represents the wave function $u(t)$ as a harmonic function of time. The complex amplitude $U = \alpha\exp(j\varphi)$ is a fixed phasor - case (b). The complex wave function $U(t) = \exp(j2\pi\nu t)$ is a phasor rotating rotating with angular velocity $\omega = 2\pi\nu$ radians/s - case (c).

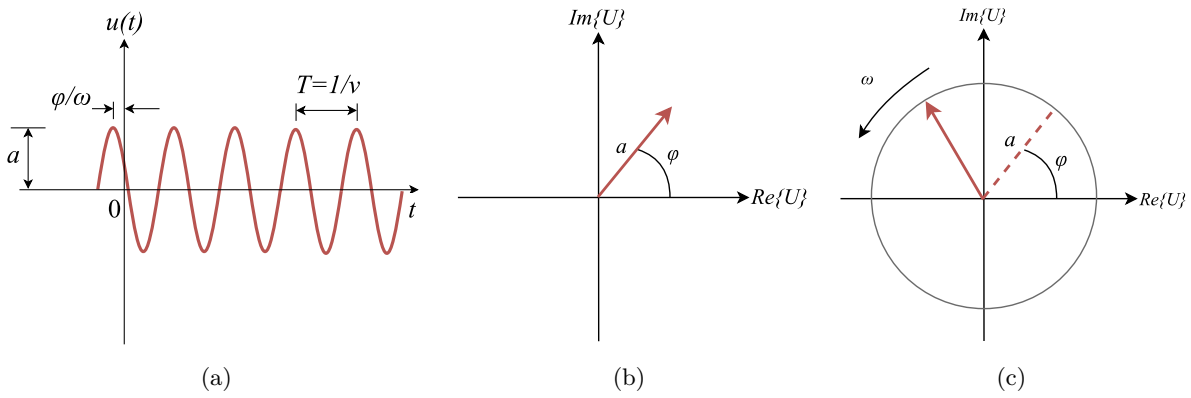

(a) (b) (c)

Figure 2.3: Representation of a monochromatic wave at a fixed position r.

As a monochromatic wave propagates through media of different refractive indexes its frequency remains the same, but its velocity, wavelength, and wave number are changed [18]:

$$c = \frac{c_0}{n}, \quad \lambda = \frac{\lambda_0}{n}, \quad k_N = nk_0, \tag{2.9}$$

and

$$\lambda = \frac{c}{\nu}, \quad k_N = \frac{2\pi}{\lambda}, \tag{2.10}$$

where λ is called the wavelength and k_N is wave number. The representation of the electric and magnetic part of the wave is shown in Figure 2.4. There are several elementary wave types we can distinguish between *plane*, *spherical*, *paraboloidal* and *paraxial* wave [18].

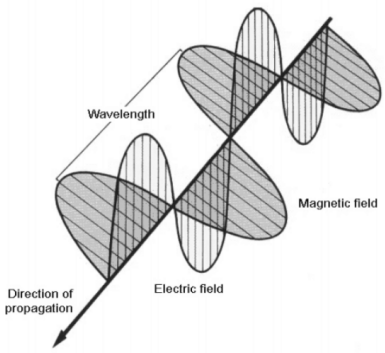

Figure 2.4: Representation of the real components of the electric and magnetic fields along the direction of propagation.

2.3 Gaussian Beam

The Gaussian beam is the basic type of the optical beam, mainly coming from a laser diode. The intensity distribution in the transverse plane corresponds to a circularly symmetric Gaussian function. Optical axis is the axis of symmetry [8].

2.3.1 Characterization

A simple free-space Gaussian beam wave model with parabolic wavefront phase envelope allows a complete characterization of the focusing or diverging characteristics of a laser beam. At $z = 0$ the free-space electric field of a unit amplitude, lowest-order paraxial Gaussian beam propagating predominantly along the z-axis can be represented in the form [28]

$$U(\rho, 0) = \exp\left[-\left(\frac{1}{w_0^2} + \frac{jk}{2R_0}\right)\rho^2\right], \tag{2.11}$$

where w_0 is the transmitter beam radius (beam size), R_0 is the radius of curvature of the phase front, k_N is the optical wave number (Equation 2.10), and $\rho = (x^2 + y^2)^{1/2}$ is a transversal distance from the beam center.

Intensity can be described as [8]:

$$I(\rho, z) = I_0 \left(\frac{w_0}{w(z)} \right)^2 \exp \left(-2 \frac{\rho^2}{w^2(z)} \right), \tag{2.12}$$

where I_0 is maximum intensity, w_0 is a beam half width (in $z = 0$), $w(z)$ is a beam half width in axial distance z (see Figure 2.6). This is valid if distance r is radial.

The beam radius varies along the propagation direction according to

$$w(z) = w^0 \sqrt{1 + \left(\frac{z}{z_R} \right)^2}, \tag{2.13}$$

where z_R is the Rayleigh length

$$z^R = \frac{\pi w_0^2}{\lambda}. \tag{2.14}$$

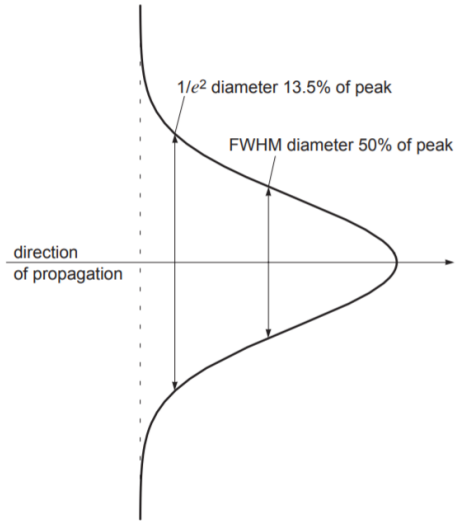

Figure 2.5: Gaussian beam intensity [45].

The full width at half maximum (FWHM) of the intensity profile is ≈1.18 times the Gaussian beam radius $w(z)$ and $1/e^2$ is assumed as a diameter of the beam, half width respectively (see Figure 2.5). Half width increases with an increasing axial distance. This is called *divergence*. For divergence angle in a half width is used following formula:

$$\theta = \frac{\lambda}{2\pi w_0}. \tag{2.15}$$

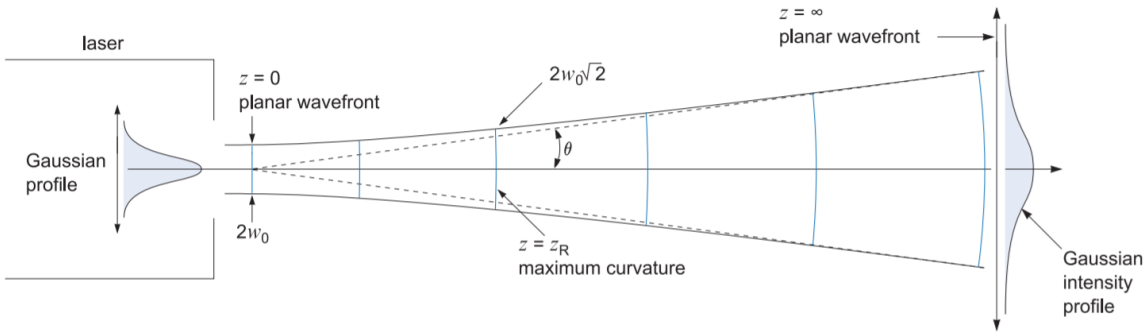

Figure 2.6: Intensity profile changes with propagation distance [45].

2.3.2 Propagation Through Optical System

For the practical use of laser beams, their spatial transformation is important in optical systems, when the beam travels through the composed system (Figure 2.7).

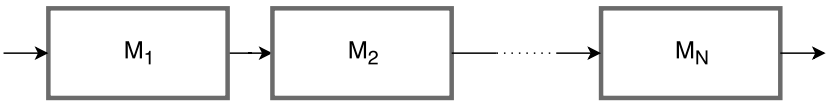

Figure 2.7: Composed optical system.

The description of the bundle transformation can be advantageous using the matrix method used in geometrical optics. Equation with the ray transfer matrix M_T is in a form [46]

$$\begin{bmatrix} x_2 \\ \theta_2 \end{bmatrix} = \begin{bmatrix} A & B \\ C & D \end{bmatrix} \begin{bmatrix} x_1 \\ \theta_1 \end{bmatrix}, \tag{2.16}$$

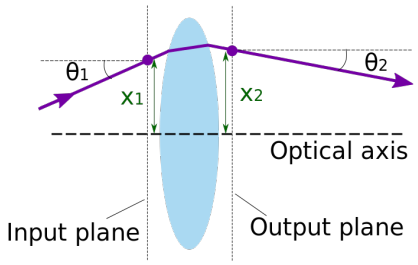

Figure 2.8: Ray transfer matrix input parameters visualization for a lens.

where input ray is given by x_1 distance and angle θ_1 and output by x_1 and θ_2 as shown in Figure 2.8. A, B, C and D are parameters based on a given type of optical object the beam

comes in. For a sphere interface (a case of a water droplet with a given radius of curvature R and refractive indexes n_1 and n_2), the matrix has following values [46] (described in Figure 2.9):

$$\text{Refraction: } M_T = \begin{bmatrix} 1 & 0 \\ (n_1 - n_1)/R & 1 \end{bmatrix}, \quad \text{Reflection: } M_T = \begin{bmatrix} 1 & 0 \\ 2n_1/R & 1 \end{bmatrix}. \tag{2.17}$$

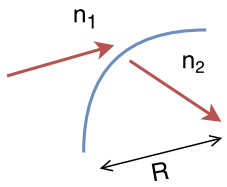

Figure 2.9: Refraction on a spheric interface.

For a composed systems, a final transfer matrix M is a multiple of all matrices [46]:

$$M_T = M_N M_{N-1} \cdots M_2 M_1. \tag{2.18}$$

3 Propagation of Light in the Atmosphere

An optical wave propagating in an unguided medium such as atmosphere has to go through many constituents such as the molecules and aerosols. These constituents cause the optical wave to get scattered and absorbed which in turn results in the degradation and attenuation of received optical signal [10].

The atmospheric attenuation is one of the challenges of the FSO channel, which may lead to signal loss and link failure. The atmosphere not only attenuates the light wave but also distorts and bends it. Transmitted power of the emitted signal is highly affected by scattering and turbulence phenomena. Attenuation is primarily the result of absorption and scattering by molecules and particles (aerosols) suspended in the atmosphere. Distortion, on the other hand, is caused by atmospheric turbulence due to the index of refraction fluctuations. Attenuation affects the mean value of the received signal in an optical link whereas distortion results in variation of the signal around the mean [26].

It is common to separate the interaction with the atmosphere into distinct optical phenomena: molecular absorption, scattering, turbulence and molecular emission. This chapter will focus on general temperate weather conditions, see Section 6 to found out information about rainy conditions.

3.1 Beer-Lambert Law

The transmission of an optical monochromatic light beam through the atmosphere can be expressed by the Beer (also known as Beer-Lambert) law [7]:

$$I(\lambda, t^{'}, x) = I(\lambda, t, 0) \exp\left(-\int_0^x \kappa(\lambda) N(x^{'}, t) dx^{'}\right), \tag{3.1}$$

where $I(\lambda, t^{'}, x)$ is the intensity of the optical beam after passing through a path length of x, $\kappa(\lambda)$ is the optical attenuation or extinction coefficient of the species per unit of species density and length, and $N(x, t)$ is the spatial and temporal distribution of the species density that is producing the absorption, λ is the wavelength of monochromatic light, and the parameter time $t^{'}$ is inserted to remind one of the potential propagation delay, $N(x, t)$ which indicates the spatial and temporal variability of the concentration of the attenuating species since in many experimental cases such variability may be dominant. $\kappa(\lambda)$ uses formula

$$\kappa(\lambda) = \kappa_a(\lambda) + \kappa_R(\lambda) + \kappa_M(\lambda), \tag{3.2}$$

where $\kappa_a(\lambda)$ represents absorption contribution, $\kappa_R(\lambda)$ contribution of Rayleigh scattering and $\kappa_M(\lambda)$ contribution of Mie scattering [7].

3.2 Beam Transmittance

The attenuation experienced by the optical signal when it passes through the atmosphere can be quantified in terms of optical depth τ which correlates with power at the receiver P_R and the transmitted power P_T as the atmospheric transmittance [47]:

$$T_a = \frac{P_R}{P_T} = \exp(-\tau), \tag{3.3}$$

which comes from Beer's law. Optical depth is defined in the same way by [48]:

$$\tau(\lambda) = \int_0^L \kappa(\lambda) dL = \kappa(\lambda) L, \tag{3.4}$$

where L is the transmission distance in km and κ_λ is the total attenuation coefficient (from Equation 3.2):

$$\kappa(\lambda) = \kappa_{am}(\lambda) + \kappa_{Mm}(\lambda) + \kappa_{Rm}(\lambda) + \kappa_{a\alpha}(\lambda) + \kappa_{M\alpha}(\lambda) + \kappa_{R\alpha}(\lambda), \tag{3.5}$$

where κ_{am} and κ_{Mm}, κ_{Rm} are the molecular absorption and Mie with Rayleigh scattering coefficients of atmosphere, respectively, and $\kappa_{a\alpha}$ and $\kappa_{M\alpha}$, $\kappa_{R\alpha}$ are the absorption and Mie with Rayleigh scattering coefficient of aerosol, respectively.

3.3 Absorption

The absorption of the optical radiation by atmospheric molecules is associated with individual optical absorption transition between the quantized energy level of the molecule. The energy levels of a molecule can usually be separated into those associated with:

- rotational (far-IR, microwave spectral region),
- vibrational (near-IR region, means 2 to 20 µm wavelength), or
- electronic energy states (UV-visible region).

Transitions can combine with each other. The overall absorption can be expressed by

$$\kappa_a(\lambda) N(x,t) = S g(v - v_0) N P_a, \tag{3.6}$$

where S is the molecular transition line intensity in cm/molecule, $g(v - v_0)$ is the normalized line shape function in cm, N is the number of molecules of absorbing species per cm^3 per atm, and P_a is the partial pressure of the absorbing gas in atm [7].

Absorption coefficient α is defined at [11] by:

$$\alpha = \sigma N_C, \tag{3.7}$$

where σ is cross section (km^2) and N_C is the concentration of the absorbing particles ($1/km^3$).

In particular, in terrestrial FSO, ***water vapor*** and ***carbon dioxide*** play the major role. The corresponding path attenuation depends on the concentration of the absorber and on the atmospheric conditions [1]. Atmospheric transmittance with marked absorbers are presented in figure 3.1. The atmospheric absorption is a wavelength-dependent phenomenon. The wavelength

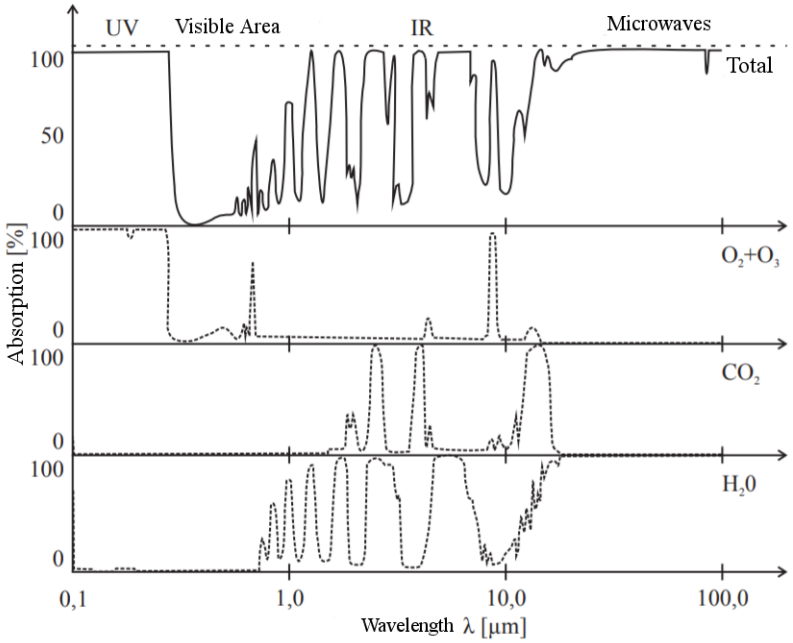

Figure 3.1: Absorption of the atmosphere components [8].

range of FSO is chosen to be affected as less as possible, in other words, to have minimal absorption. This is referred to as atmospheric transmission windows. In such a window, the attenuation due to molecular or aerosol absorption is less than 0.2 dB/km. There are several transmission windows within the range of 700–1600 nm. Majority of FSO systems are designed to operate in the windows of 780–850 and 1520–1600 nm [47]. Practically gas absorption has little impact on terrestrial links in the near-IR windows, whereas it exhibits somewhat higher values in the mid-IR (Table 3.1).

Table 3.1: 10.6 µm attenuation (in dB) due to gas over a horizontal 1 km path at sea level [1].

Atmospheric conditions	Water vapor	CO_2
Summer high-latitude (14 °C, 1008 hPa, 9 mm of H_20)	0.3	0.3
Winter high-latitude (−16 °C, 1011 hPa, 1 mm of H_20)	0.0	0.1
Summer mid-latitude (22 °C, 1013 hPa, 14 mm of H_20)	0.9	0.3
Winter mid-latitude (0 °C, 1019 hPa, 4 mm of H_20)	0.0	0.2
Low-latitude (27 °C, 1012 hPa, 20 mm of H_20)	1.7	0.4

3.4 Scattering

When light travels through any medium, its waveform gets distorted by the particles of this medium causing a loss of signal. It is different than absorption since the energy is redistributed rather than absorbed. It can be understood as a redirection or redistribution of light that can lead to a significant reduction of received light intensity at the receiver location. The intensity of the scattering depends on the size of the particles (scatterers) [11]. Each type can be divided into one of these type of scattering [7]:

- *Elastic scattering.* It does not cause shift of wavelength of incident light (i.e. Mie, Rayleigh scattering).
- *Inelastic scattering.* It causes shift of wavelength of incident light (i.e. Raman scattering).

Section 3.4 focuses on the elastic scattering description.

3.4.1 Rayleigh Scattering

Rayleigh scattering is scattering of the optical radiation due to the displacement of the weakly bound electronic cloud surrounding the gaseous molecule which is perturbed by the incoming electromagnetic (optical) field. A wavelength of the incoming light is much larger than the physical size of the scatterers. For instance, this phenomena makes the color of thy sky blue and the setting or rising sun red. The Rayleigh differential scattering cross section for polarized, monochromatic light is given by [7]:

$$\frac{\mathrm{d}\sigma_R}{\mathrm{d}\Omega} = \left[\frac{\pi^2(n^2-1)^2}{N^2\lambda^4}\right]\left[\cos^2\phi\cos^2\theta + \sin^2\phi\right], \tag{3.8}$$

where n is the index of refraction of the atmosphere, N is the density of molecule, λ is the wavelength of the optical radiation, and ϕ and θ are the spherical coordinate angles of the scattered polarized light referenced to the direction of the incident light. This equation defines that shorter-wavelength light is more scattered out from a propagating beam than the longer wavelengths.

Total Rayleigh scattering cross section can be determined from Equation 3.8 by integrating over 4π steradians to yield [7]:

$$\sigma_R = \left[\frac{8}{3}\right]\left[\frac{\pi^2(n^2-1)^2}{N^2\lambda^4}\right]. \tag{3.9}$$

Another approach to obtain value of molecular coefficient can be found in [27]:

$$\sigma_R(\lambda) = A\lambda^{-4}, \tag{3.10}$$

$$A = 1.09 \cdot 10^{-3}\frac{P_A}{P_0}\frac{T_0}{T_A} \quad (km^{-1}\mu\mathrm{m}^4), \tag{3.11}$$

where P_A is the atmospheric pressure and $P_0 = 1013$ mbar and T_A is the atmospheric temperature and $T_0 = 273.15$ K.

3.4.2 Mie Scattering

Mie scattering is similar to Rayleigh scattering, but appears in an environment with scatterer's size same or similar as the wavelength of the incident light. The scattered radiation experiences more complex functional dependences upon the the optical wavelength and particle size distribution than that seen for Rayleigh scattering. As seen in Figure 3.2, Mie's analysis indicated the clear asymmetry between the forward and backward directions of scattering, where for large particle sizes the forward-directed scattering dominates [7].

Different type of scattering, their originator and given conditions according to Recommendation ITU-R [6] are shown in table 3.2.

Table 3.2: Scattering regimes depending on the scatter, wavelength λ and attenuation coefficient $\kappa(\lambda)$.

	Rayleigh scattering	**Mie scattering**	**Non-selective or geometric scattering**
Conditions	$r \ll \lambda$ $\kappa(\lambda) \sim \lambda^{-4}$	$r \approx \lambda$ $\kappa(\lambda) \sim \lambda^{-1.6}$ to $\kappa(\lambda) \sim \lambda^0$	$r \gg \lambda$ $\kappa(\lambda) \sim \lambda^0$
Type of scatter	Air molecules Haze	Haze Fog Aerosol	Fog Rain Snow Hail

The scattering coefficient can be evaluated according following formula based on visibility and wavelength [27]:

$$\beta_n(\lambda) = \frac{3.91}{V}\left(\frac{\lambda_{nm}}{550}\right)^{-Q}, \tag{3.12}$$

where V is the visibility in km, λ_{nm} is the wavelngth in nm, Q is a factor which depends in the scattering particle size distribution:

- 1.6 for large visibilty ($V > 50$ km),
- for mean visibility ($6 < V < 50$ km),
- 0.585 $V^{1/3}$ for low visibility ($V < 6$km).

3.4.3 Non-Selective Scattering

The final scattering mechanism is called the non-selective scattering. This occurs when the particles are much larger than the wavelength of the radiation. Water droplets and large dust particles can cause this type of scattering. Non-selective scattering gets its name from the fact that all wavelengths are scattered about equally, not only certain "colors". This type of scattering causes fog and clouds to appear white to our eyes because blue, green, and red light are all scattered in approximately equal quantities (blue, green and red light are components of the white light) [9].

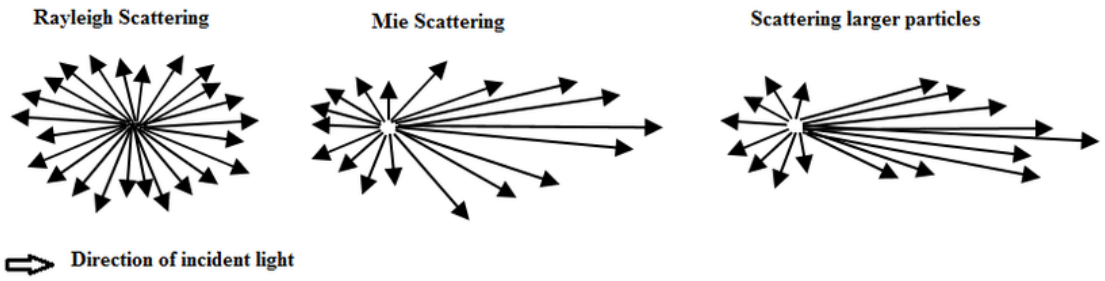

Figure 3.2: Patterns of Rayleigh, Mie and non-selective scattering [12].

3.5 Molecular Emission and Thermal Spectral Radiance

The same optical molecular transition that causes absorption also emit light when they are thermally excited. Since the molecules have a finite temperature T, they will act as blackbody radiators with optical emission. The thermal radiation from the clear atmosphere involves the calculation of the blackbody radiation emitted by each elemental volume of air multiplied by the

absorption spectral distribution of the molecular absorption lines, $\kappa_a(s)$ and then this emission spectrum is attenuated by the rest of the atmosphere as the emission propagates toward the viewer. It is expressed by:

$$I_v = \int_0^s \kappa_a(s) P_\nu(s) \exp\left[-\int_0^s \kappa_a(s')\mathrm{d}s'\right] \mathrm{d}s, \tag{3.13}$$

where the exponential term comes from Beer's law, and $P_v(s)$ is the Planck function given by

$$P_v(s) = \frac{2h\nu^3}{c^2 \exp(\left[\frac{h\nu}{kT(s)}\right] - 1)}. \tag{3.14}$$

In equations, s is the distance from the receiver along optical propagation path, ν is the optical frequency, h is Planck's constant, c is the speed of light, k is Boltzmann's constant, and $T(s)$ is the temperature at position s along the path. As seen in Equation 3.13, each volume element emits thermal radiation $\kappa_a(s)P_\nu(s)$, which is then attenuated by Beer's law. The total emission spectral density is obtained by summing or integrating over all the emission volume elements and calculating the appropriate absorption along the optical path for each element [7].

3.6 Turbulences

Besides the effect of the constituents, the refractive index at each point in the medium varies randomly in time due to the circulation of air in the atmosphere causing variable refractive index. This is simply known as the *turbulence* [10].

In a general point of view, the atmosphere can be described as a viscous fluid that has two distinct states of motion, i.e. laminar and turbulent. In case of turbulent flow, the velocity loses its uniform characteristics due to dynamic mixing and acquire random sub-flows called turbulent eddies. The transition from laminar to turbulent motion is determined by the nondimensional quantity called Reynolds number, discussed in Section 7.1.1 [47].

Atmospheric turbulence is developed mainly by the fluctuation in the temperature, pressure, and humidity but dominated by temperature fluctuations. The overall effect of turbulence on the received optical signal is composed of the wavelength, λ, link length, L, the structure constant, C_n^2 (a measure of how large the refractive index fluctuations are) [10].

The measure of turbulence strength in the atmosphere is given by the plane wave scintillation index described in following section.

3.6.1 Methods of Description

In the evaluation of turbulences effects, the random medium is modeled by eddies of various sizes in the continuum form. The eddies can be though of lenses. The random medium is composed of continuum of lenses starting from a minimum scale size known as the inner scale of turbulence to the maximum scale known as the outer scale of turbulence. The optical wave propagating in this continuum of lenses faces reflection, refraction, scattering diffraction and interference which in turn results in the fluctuations of the amplitude and the phase of the optical wave. The effect of the eddies of all scale sizes are integrated in the power spectrum model of turbulence [10].

The Kolmogorov mathematical model (Figure 3.3) of the atmospheric turbulence and its effects on the optical beam propagation assumes that the fluctuations in the atmospheric parameter are stationary random processes having statistically homogeneous nature. The structure function in the inertial range satisfies the universal two-thirds power law, i.e., it follows $r^{2/3}$ dependence, where r refers to the spatial scale defined as:

$$r = |\vec{r_1} - \vec{r_2}|, \quad l_0 \leq r \leq L_0, \tag{3.15}$$

where $\vec{r_1}$ and $\vec{r_2}$ refer to position vectors at two points separated by distance r in space.

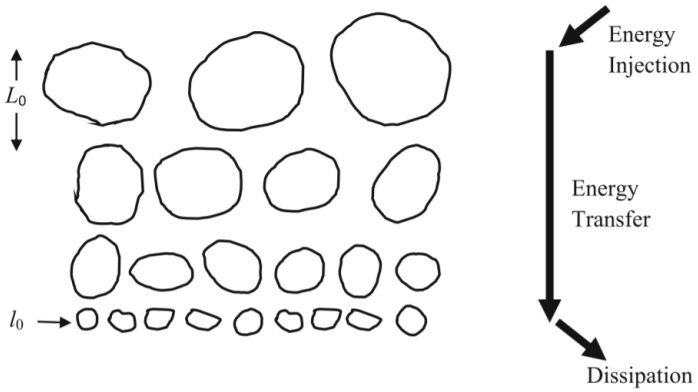

Figure 3.3: Kolmogorov model where L_0 and l_0 are the outer and inner scale of turbulent eddies, respectively [47].

3.6.2 Scintillation

If the eddy size is of the order of beam size, then the eddies will act like a lens that will focus and de-focus the incoming beam and broaden the beam leading to irradiance fluctuations at the receiver and the process is called scintillation. Scintillations cause the loss of signal-to-noise ratio

and result in deep random signal fades. The effect of scintillation can be reduced by employing techniques like multiple transmit/receive antennae, aperture averaging, etc. [10], [47].

Scintillation may be the most noticeable one for FSO systems. Light traveling through scintillation will experience intensity fluctuations, even over relatively short propagation paths. The scintillation index, σ_i^2 describes such intensity fluctuation as the normalized variance of the intensity fluctuations given by [26]:

$$\sigma_i^2 = \frac{\langle I^2 \rangle}{\langle I \rangle^2} - 1, \tag{3.16}$$

where $I = |E|^2$ represents the signal irradiance (or intensity). Scintillation index for plane waves comes from Rytov approximation and is known as

$$\sigma_i^2 = 1.24 C_n^2 k^{7/6} L^{11/6}, \tag{3.17}$$

(seen with 1.23 constant as well) where k_N is the wave number (Equation 2.10). Turbulent regime in the atmosphere is weak, moderate, strong and extremely strong when σ_i^2 is $\ll 1, \sim 1, > 1$ and $\gg 1$, respectively [10].

Rytov approximation is one of the approximations, a value of attenuation caused by turbulences can be expressed by [8]:

$$\gamma = 2 \cdot \sqrt{23.17 C_n^2 k^{7/6} L^{11/6}}. \tag{3.18}$$

The expression for the variance for large fluctuations is as follows [29]:

$$\sigma_{high}^2 = 1.0 + 0.86 (\sigma_i^2)^{-2/5}. \tag{3.19}$$

3.6.3 Beam Wander

If the size of eddies are larger than the transmitter beam size, it will deflect the beam as a whole in a random manner from its original path (Figure 3.4). This phenomenon is called beam wander, and it effectively leads to pointing error displacement of the beam that causes the beam to miss the receiver [47].

So far, many papers has focused on the analytical expression of beam wandering. For a beam in the presence of large cells of turbulence compared to the beam diameter, geometrical optics can be used to describe the radial variance σ_r, as a function of wavelength and distance L by [29] as follows:

$$\sigma_r = 1.83 C_n^2 \lambda^{-1/6} L^{17/6}. \tag{3.20}$$

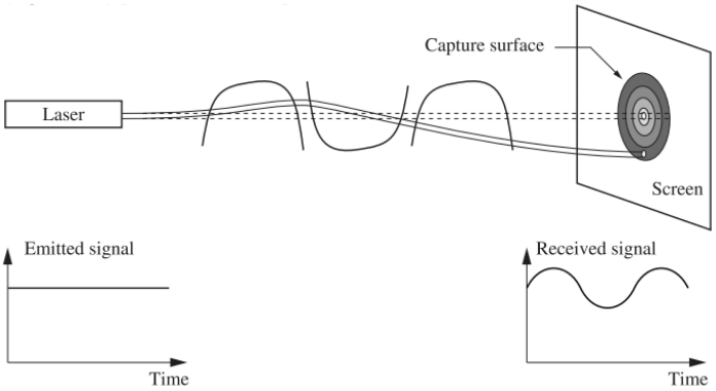

Figure 3.4: Deviation of a beam under the influence of turbulence cells larger than the beam diameter [27].

3.6.4 Incoherent Beam

When a coherent laser source beam wave propagates through turbulence, its coherence property is distributed that makes the beam much less coherent. In other words, coherence radius of the beam, which is defined as the radius of the area over which the optical field remain correlated, becomes smaller as the beam propagates in the turbulent medium [10].

3.6.5 Beam Spreading

If the eddy size is smaller than the beam size, then a small portion of the beam will be diffracted and scattered independently. This will lead to a reduction in the received power density and will also distort the received wavefront (Figure 3.5). However, the effect of turbulence-induced beam spreading will be negligible if the receiver aperture diameter is kept greater than the size of first Fresnel zone[1] $\sqrt{R/k}$. In this case, the only effect will be due to turbulence-induced beam wander effect and scintillation effect [47].

Beam spreading describes the broadening of the beam size at a target beyond the expected limit due to diffraction as the beam propagates in the turbulent atmosphere. The following description is in the case of a Gaussian beam, at a distance l from the source, when the turbulence is present. Then the irradiance of the beam averaged in time is:

$$I(l,r) = \frac{2P_0}{\pi\omega_{eff}^2(t)} exp\left(\frac{-2r^2}{\omega_{eff}^2(t)}\right), \tag{3.21}$$

where P_0 is total beam power in W and r is the radial distance from the beam center.

[1]Concentric prolate ellipsoidal regions of space between and around a transmitting and receiving system.

The beam will experience a degradation in quality with a consequence that the average beam waist in time will be $\omega_{eff}(l) > \omega(l)$. To quantify the amount of beam spreading, describes the effective beam waist average as:

$$\omega_{eff}(l)^2 = \omega(l)^2(1+T), \tag{3.22}$$

where $\omega(l)$ is the beam waist that after propagation distance L is given by:

$$\omega(l)^2 = \left[\omega_0^2 + \left(\frac{2L}{k\omega_0}\right)^2\right] \tag{3.23}$$

In which ω_0 is the initial beam waist at $L = 0$, T is the additional spreading of the beam caused by the turbulence. As seen in other turbulence figure of merits, T depends on the strength of turbulence and beam path. Particularly, T for horizontal path, one gets:

$$T = 1.33\sigma_i^2\Lambda^{5/6}, \tag{3.24}$$

where

$$\Lambda = \frac{2L}{k\omega^2(t)}. \tag{3.25}$$

The effective waist, $\omega_{eff}(l)$, describes the variation of the beam irradiance averaged over long term.

As seen in other turbulence figure of merits, $\omega_{eff}(l)^2$ depends on the turbulence strength and beam path. Due to the fact that $\omega_{eff}(l) > \omega(l)$ beam will experience a loss that at beam center will be equal [26]:

$$L_{BE} = 20\log\left(\frac{\omega(l)}{\omega_{eff}(l)}\right). \tag{3.26}$$

Final result effect of small and big turbulences are shown in Figure 3.6.

3.6.6 Other Effects

Degradation of the optical beam wave due to turbulence arises due to the random fluctuations of the phase as well which cause the phase front of the optical wave get distorted. The phase fluctuations also become the reason for the angle of arrival fluctuations. Large angle of arrival fluctuations degrades the reception of the optical signal especially when the field of view of the receiver is narrow [10].

Turbulence also has an effect on the effective radius of curvature of the optical beam that degrades the focusing of the beam on the required spot. Other parameters which are degraded

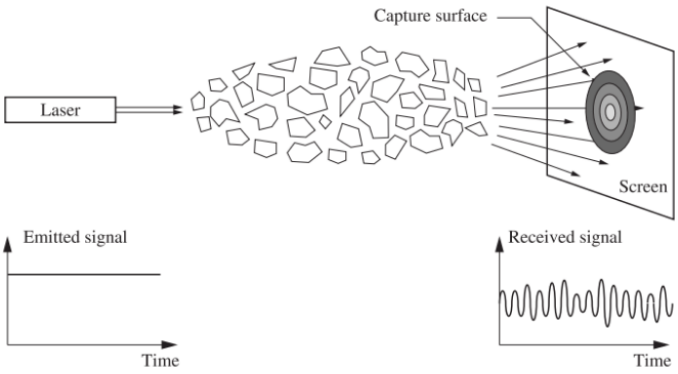

Figure 3.5: Deviation of a beam under the influence of turbulence cells smaller than the beam diameter [27].

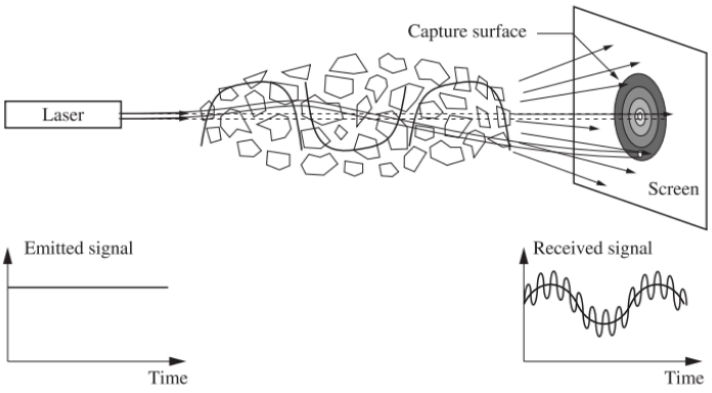

Figure 3.6: Effects of various sized constituents on a laser beam propagation [27].

by the presence of turbulence are the propagation factor, also known as the M^2 factor, being regarded as a beam quality factor [10].

3.7 Geometric Losses

The geometric path loss for an FSO link depends on the beam-width of the optical transmitter θ, its path length L and the area of the receiver aperture A_r. The transmitter power, P_r is spread over an area of $\pi(L\theta)^2/4$. The geometric loss is the ratio of the surface area of the receiver aperture to the surface area of the transmitter beam at the receiver. Since the transmit beams spread constantly with increasing range at a rate determined by the divergence, geometric loss

depends primarily on the divergence as well as the range and can be determined by the formula stated as [26]:

$$Loss = \frac{d_2^2}{|d_1 + (L\theta)|^2}, \tag{3.27}$$

where d_2 is the diameter receiver aperture (unit: m), d_1 is the diameter transmitter aperture (m) and θ is the beam divergence (mrad).

According to [27], the loss is given by

$$Loss = \frac{\frac{\pi}{4}(d\theta)^2}{S_{capture}}, \tag{3.28}$$

where d is the transmitter - receiver distance and $S_{capture}$ is the capture area of the receiver (m^2). Geometric path loss is present for all FSO links and must always be taken into consideration in the planning of any link. This loss has a fixed value for a specific FSO deployment scenario; it does not vary with time, unlike the loss due to rain attenuation, fog, haze or scintillation [26].

3.8 Total Attenuation

The total attenuation is a combination of atmospheric attenuation in the atmosphere and geometric loss (atmospheric turbulence excluded) and is given by the following equation [26]:

$$\frac{P_r}{P_t} = \frac{d_2^2}{|d_1 + (L\theta)|} \exp(-\beta L), \tag{3.29}$$

where P_t is the transmitted power, P_r is the received power, and β is the total scattering coefficient.

3.9 Visibility Runway Visual Range

Visibility was defined originally for meteorological needs. It defined as (Kruse model) means of the length where an optical signal of 550 nm is reduced to 2% of its original value. However, this estimation is influenced by many subjective and physical factors. The essential meteorological quantity, namely the transparency of the atmosphere, can be measured objectively and it is called the Runway Visual Range (RVR) or the meteorological optical range [26].

4 Free Space Optical Communication

Free space optical systems are terrestrial point-to-point OWC (Optical Wireless Communication) system operating at the near IR frequencies. These systems offer a cost-effective link with data rates, i.e. 10 Gbps per wavelength. FSO links face a number of challenges that will affect its wide usage. These challenges are related to the atmospheric conditions (fog, turbulence, and rain - which is a topic of this thesis), which will affect the link availability at all times. FSO can be also used in indoor environments (i.e. big organizations) to provide high bandwidth connectivity in multi-point scenarios [1].

4.1 General Description

FSO is a line-of-sight[2] technology that uses lasers to provide optical bandwidth connections or FSO is an optical communication technique that propagates the light in free space means air, outer space, vacuum, or something similar to wirelessly transmit data for telecommunication and computer networking. FSO is capable to transfer data, voice and video communications through the air, allowing optical connectivity without requiring fiber-optic cable or securing spectrum licenses.

It operates between the 700 – 1600 nm wavelengths bands and use O/E[3] and E/O converters. FSO requires light, which can be focused by using either light emitting diodes (LEDs) or LASERs (light amplification by stimulated emission of radiation). The use of lasers is a simple concept similar to optical transmissions using fiber-optic cables; the only difference is the transmission media. Light travels through air faster than through glass, so it is able to classify FSO as optical communications at the speed of light. FSO communication is considered as an alternative to radio relay link LOS communication systems.

4.2 Optical Wireless Channel

FSO communication consists three stages (Figure 4.1):

- *transmitter* usually considered as an optical source 1-laser diode (LD) or 2-light emitting diode (2-LED) to send of optical radiation through the atmosphere obeys the Beer-Lambert law 3.1,
- *free space transmission channel* where exist the turbulent eddies (cloud, rain, smoke, gases, temperature variations, fog and aerosol), and
- *receiver* to process the received signal.

[2]LOS - a method based on waves traveling in a direct path from the source to the receiver
[3]Optical/Electrical

Typical links are between 300 m and 5 km (in troposphere), although longer distances can be deployed such as 8 – 11 km are possible depending on the speed and required availability [26]. Nowadays, it is possible to reach bit rates around Gbps for short distances (a few kilometers) [8]. An example of the structure of FSO equipment is shown in Figure 4.2 containing receiving and transmitting part for a duplex (two-way) communication.

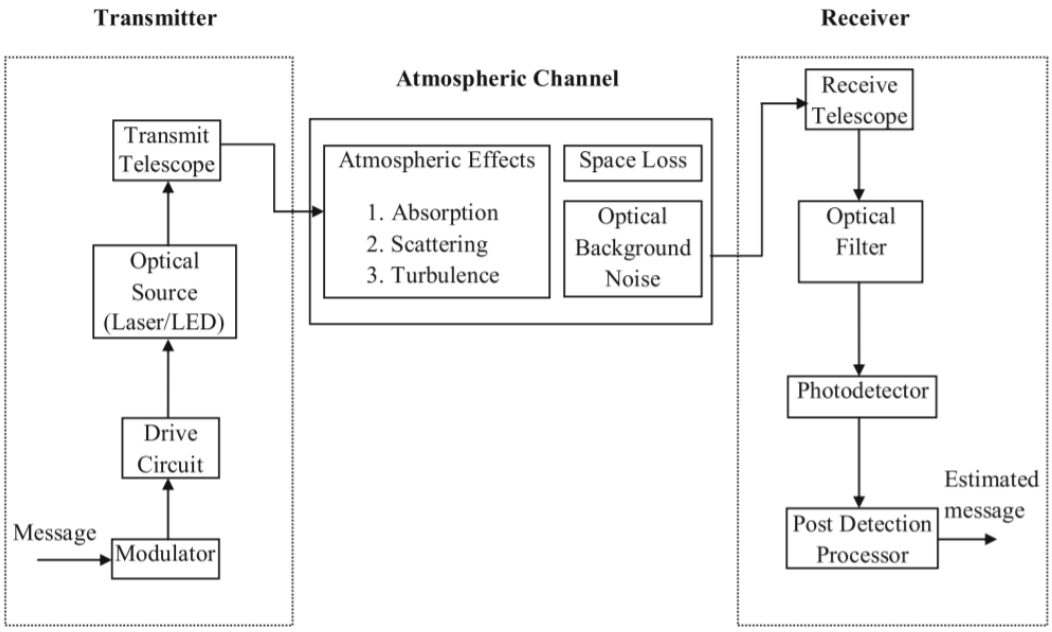

Figure 4.1: Terrestrial FSO block diagram.

4.2.1 Optical Sources

The transmission wavelength is correlated with one of the atmospheric windows. Suitable atmospheric windows are around 850 nm and 1550 nm in the shorter IR wavelength range. In the longer IR spectral range, some wavelength windows are present between 3–5 micrometers (especially 3.5–3.6 micrometers) and 8–14 micrometers. The availability of suitable light sources in these longer wavelength ranges is pretty limited. In addition, most sources need low temperature cooling, which limits their use in commercial telecommunication applications. Other factors that impact the use of a light source include price and availability of commercial components, transmission power, lifetime, modulation capabilities, eye safety, physical dimensions and compatibility with other transmission media such as fiber [26].

Electrical input is a network traffic into pulses of invisible light representing 1s and 0s. The transmitter, which consists of two main parts: an interface circuit and source driver circuit,

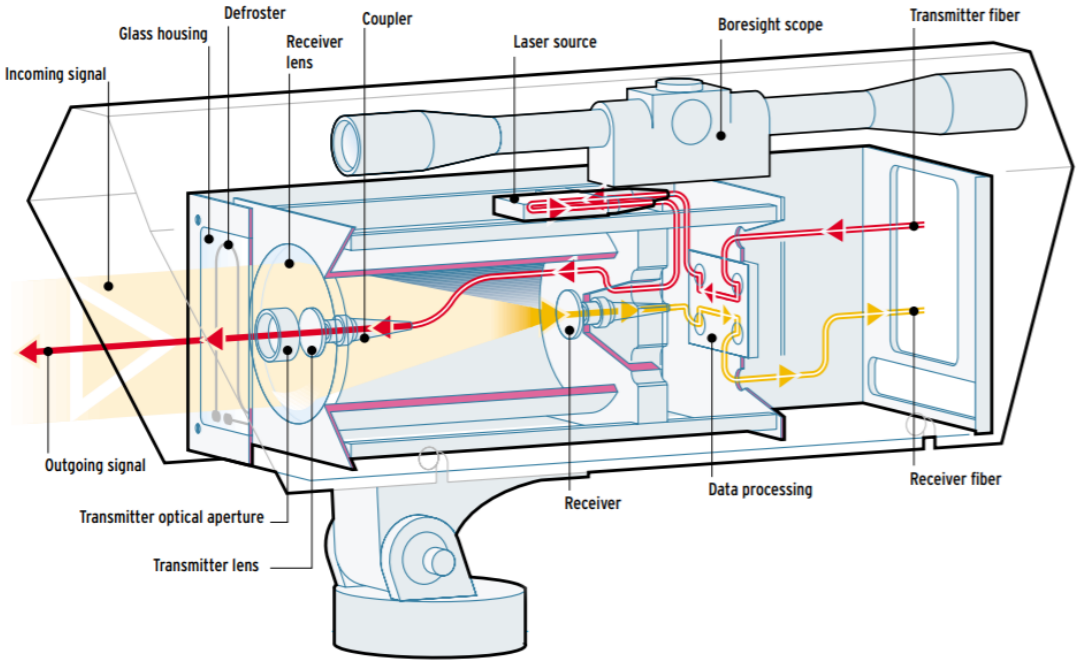

Figure 4.2: Example of equipment for FSO link [8].

converts the input signal to an optical signal suitable for transmission. The drive circuit of the transmitter transforms the electrical signal to an optical signal by varying the current following through the light source. The information signal modulates the field generated by the optical source. The modulated optical field then propagates through a free-space path before arriving at the receiver [20].

The optical part of the transmitter involves source and a telescope assembly. The telescope can be designed by using lenses or a parabolic mirror. The telescope narrows the beam and project it towards the receiver. In practical applications, the beam divergence if the transmission beam varies between a few hundred microradiants and a few miliradiants [29].

4.2.2 Optical Detectors

The transmitted light is picked up at a receiver side by using a lens or a mirror. The received light is focused on a photodetector. For practical purposes, the projected beam size at the receiving end is much larger than the size of receiving optics and part of the light energy is lost [29].

In the receiver side, transmitted data realizes inverse operations i.e., photo detector converts the optical signal back into an electrical form. In other words, a receiver at the other end of the link collects the light using lenses and/or mirrors. Received signal converted back into fiber or

copper and connected to the network. Reverse direction data transported the same way (full duplex) [20].

Photodetectors (the most used types of detectors in FSO are PIN diodes and Avalanche Photo Diodes) made of semiconductors are either photoresistances, current or voltage generators. When they are illuminated, the values of the resistance, the current or the voltage depend on the incident radiant power. In the case of semiconductor devices, a part of the incident power is absorbed in the detector volume: each photon whose energy is higher or equal to the energy band gap is absorbed and dissociated a pair of carriers. An electron and a hole are therefore released in the conduction and the valence bands respectively [27]:

$$E_{photonabsorbed} = h\nu \geq \frac{1.24}{\lambda}, \tag{4.1}$$

where E unit is eV and h is Planck's constant.

4.3 Signal Link Calculation

To be able to transmit data through any communication channel, signal link values has to be count as the most valuable part of developing the channel. For FSO systems, the basics obey [47]:

$$P_R = P_T(G_T\nu_T\nu_{TP})\left(\frac{\lambda}{4\pi R}\right)^2(G_R\nu_R\nu_\lambda), \quad \text{(W)} \tag{4.2}$$

where

- P_R - signal power at the input of photodetector,
- P_T - transmitter power,
- ν_T and ν_R - efficiences of transmitter and receiver optics, respectively,
- G_T - gain of the transmitting optics,
- G_R - gain of the receiving optics,
- ν_{TP} - transmitter pointing loss,
- $\left(\frac{\lambda}{4\pi R}\right)^2$ space loss where R is the link distance, and
- ν_λ narrowband filter transmission factor.

For link calculation, link margin is also used for expressing of required input power [27].

4.4 Modulation Schemes

The modulation schemes can be divided into two categories: baseband intensity modulation and subcarrier intensity modulation. The most used method used for the detection of the optical signal is *direct detection*. When the intensity-modulated signal is detected by a direct detection

receiver, the scheme is known as intensity-modulated/direct detection (IM/DD) and is common in FSO systems [47].

In a subcarrier intensity modulation (SIM) scheme, the radio-frequency (RF) electrical subcarrier signal is pre-modulated with the information signal. The electrical subcarrier can be modulated using any modulation scheme like binary PSK, QAM etc. (discussed in this section).

In FSO, we can often meet with On-Off keying, Pulse-Position Modulation (PPM), Phase-Shift Keying (PSK), Quadrature amplitude modulation (QAM) and their derivation. The overview is shown in Figure 4.3.

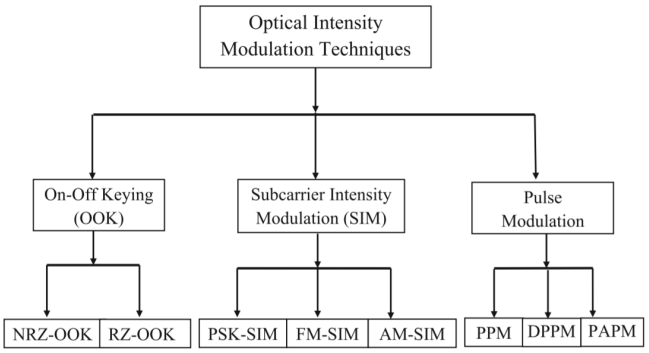

Figure 4.3: Modulation techniques used in FSO [47].

4.4.1 On-Off Keying

The dominant form of signaling used in optical communication systems was On-Off keying (OOK), because the transmitter and receiver hardware is relatively simple and fiber optic networks generally operate at high signal-to-noise ratios with small dynamic range requirements and well-controlled signal levels at the receivers. OOK is a form of intensity modulation in which binary information is represented by the presence or absence optical signal energy within the symbol. At the receiver, the "1" or "0" logical decision is determined by the received symbol energy being above or below a predetermined threshold. The optimum threshold balances the probability of 0 and 1 errors, and is dependent on the received signal power and noise statistics [28]. Non-return-to-zero (NRZ) and return-to-zero (RZ) line codes - encoding mechanisms of OOK are shown in Figure 4.4.

4.4.2 Pulse Position Modulation

Pulse position modulation (PPM) is a modulation technique mainly to increase transmission efficiency in the FSO systems. PPM is an orthogonal baseband modulation technique and has been studied extensively in optical communications for its superior power efficiency compared to

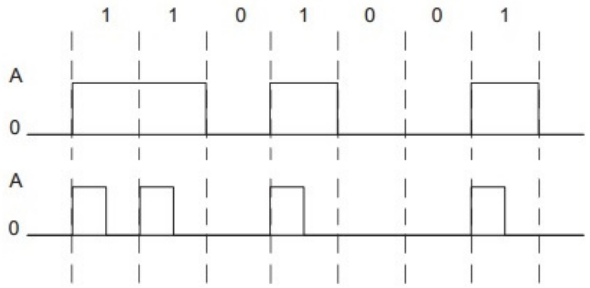

Figure 4.4: OOK modulation - NRZ and RZ line codes.

any other baseband modulation techniques. The technique can improve the power efficiency of OOK, but at the expense of an increased bandwidth requirement and greater complexity. The factor of superior power efficiency makes it well suited for handheld devices which requires low consumption [30].

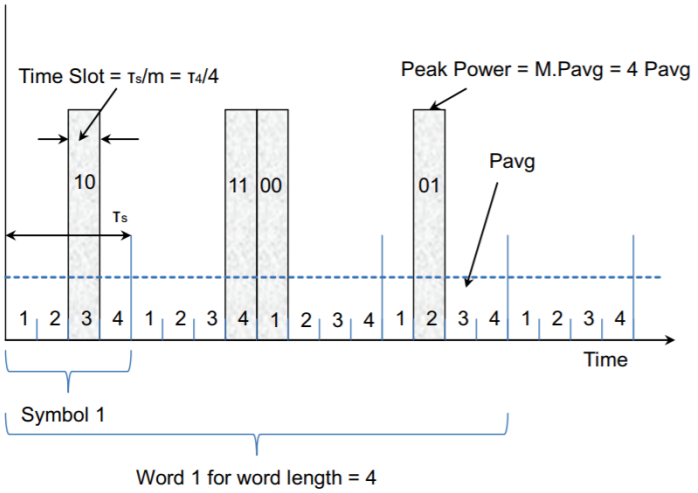

Figure 4.5: Representation of an information bit 10110001 for a 4-PPM format. PPM pulse position modulation.

In this scheme, a PPM symbol consists of a single pulse of one slot duration within L ($= 2^M$ where $M > 0$ is an integer) possible time slots with the remaining slots being empty. Information is sent by transmitting a non-zero optical intensity in a single time slot, while other slots remain dark. Each block of $\log_2 M$ data bits is mapped to one of M possible symbols [30]. An example of the representation of an information bit 10110001 for 4-PPM is shown in Figure 4.5.

4.4.3 PSK, ASK and QAM

The general principle of quadrature modulation used with M-ary PSK and M-ary QAM can be generalized to include both amplitude and phase modulation. Based on diversion of these parts, we talk about *phase shift keying* and *amplitude shift keying*. To combine advantages of both approaches, the *quadrature amplitude modulation* was introduced [39].

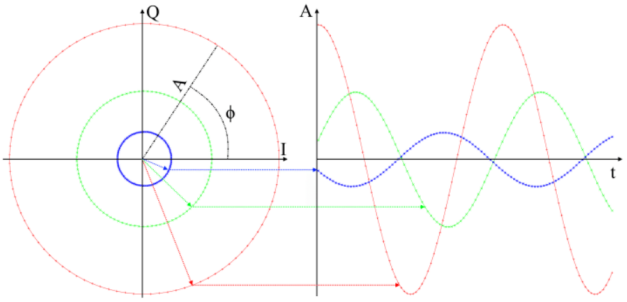

Figure 4.6: PSK/ASK transforming to I/Q plane for sine wave [40].

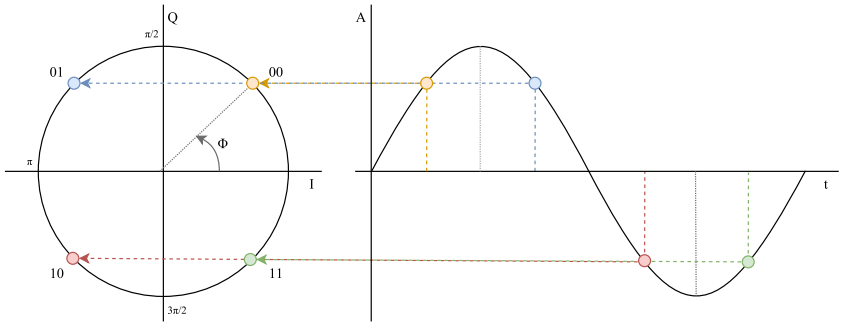

Figure 4.7: QPSK sampling.

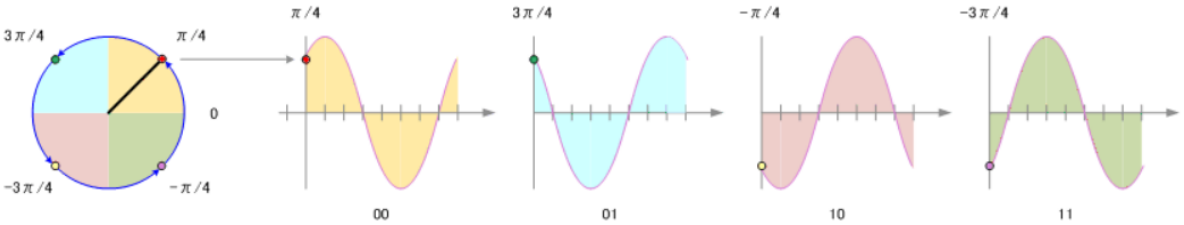

Figure 4.8: QPSK sampling - final wave shapes for given bits [41].

Change phase and amplitude are shown in Figure 4.6. The received signal is captured in a form of I/Q (constellation) diagram. If the wave varies in amplitude A or ϕ component, the resulting data point changes its place in the diagram. For instance, quadrature phase shift keying

(QPSK) modulation format is able to transmit two bits due to four available states caused by changing the phase (Figures 4.7 and 4.8).

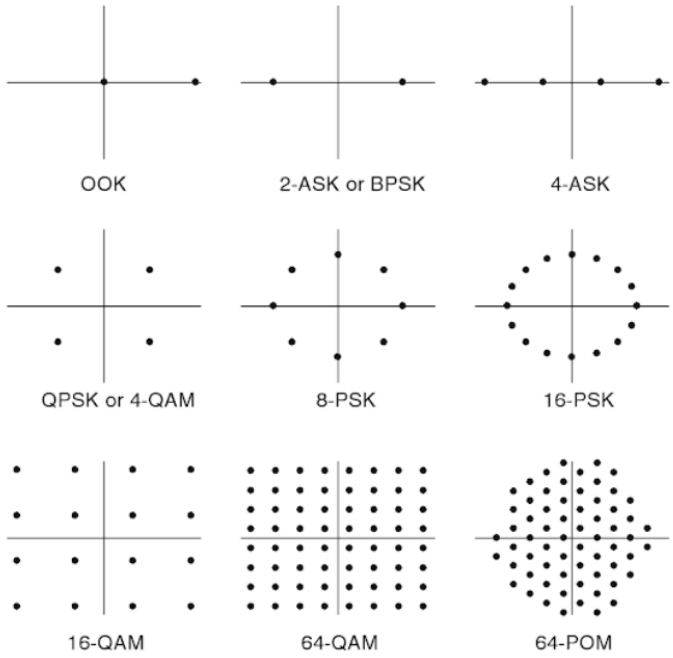

Figure 4.9: Constellation diagrams for different amplitude and phase shift keying [39].

4.5 Quality Measurement

4.5.1 Signal-Noise Ratio

The noise contributions come from all possible sources which include signal shot noise, dark current noise, thermal/Johnson noise in the electronics following the photo detector, and the background noise. The average value can be expressed by [28]:

$$SNR = \frac{SNR_0}{\sqrt{\frac{P_{S0}}{P_S} + \sigma_I^2(D) SNR_0^2}}, \tag{4.3}$$

where SNR_0 is the ratio in absence of turbulence, P_{S0} is the signal power in the absence of atmospheric effects, the mean input signal power P_S and $\sigma_I^2(D)$ is the aperture-averaged scintillation index.

According to [26], with turbulence, the SNR is expressed as follows:

$$SNR = \left(0.31 C_n^2 k^{7/6} l^{11/6}\right)^{-1}, \tag{4.4}$$

In the model, it is assumed that the surface area of the photo detector is large enough so that the effective SNR includes the beam spreading effect, thus the effective SNR is defined as:

$$SNR_{eff} = \frac{SNR}{1 + 1.33\sigma_i^2 \left[\frac{2l}{k\omega(l)^2}\right]^{5/6}}. \tag{4.5}$$

4.5.2 Bit Error Ratio

When the information is sent by digital transmission, the desired message is converted to binary symbols (bits). The transmission of digital bits over the optical link is then done on a bit-by-bit basis (binary encoding). The real performance measure in digital communications is provided not directly by the SNR, but rather by the probability of error, also referred to as BER.

Bit Error Ratio (BER) is generally defined in telecommunications as:

$$BER = \frac{N_{ErrB}}{N_B}, \tag{4.6}$$

where N_{ErrB} is amount of receiver bits with error and N_B is amount of all received bits. It can be defined also as the probability that an error may occur in a bit in the pulse train, i.e., a "1" bit turns into a "0" bit or vice versa. For commercial telecommunications applications, BER=10^{-9} is a typical required value. In general, the BER is expressed by [28]:

$$BER = \frac{P(0|1)}{2} + \frac{P(1|0)}{2}, \tag{4.7}$$

where $P(0|1)$ is the probability of mistaken "0" for "1", and $P(1|0)$ is the probability of mistaken "1" for "0" (conditional probabilities). The 1/2 multiplicative factor comes from the fact that, in a general digital communication system, "0" and "1" are almost equally distributed.

For FSO links with an On-Off keying modulation scheme in BER can be written as

$$BER = \frac{\exp(-SNR/2)}{(2\pi SNR)^{0.5}}. \tag{4.8}$$

By [28], BER is given by

$$BER = \frac{1}{2} \int p_I(s) erfc\left(\frac{SNRs}{2\sqrt{2}i_S}\right) \mathrm{d}s, \tag{4.9}$$

where $p_I(s)$ is the probability distribution of irradiance, i_S is the instantaneous signal current whose mean value, and SNR is the average SNR in presence of turbulence defined earlier.

4.5.3 Modulation Error Ratio

Modulation error ratio (MER) is a measure of the sum of all interference effects occurring on the communication (transmission) path [38]. MER indicates the accuracy of the modulation, which can be interpreted in the I/Q diagram [39].

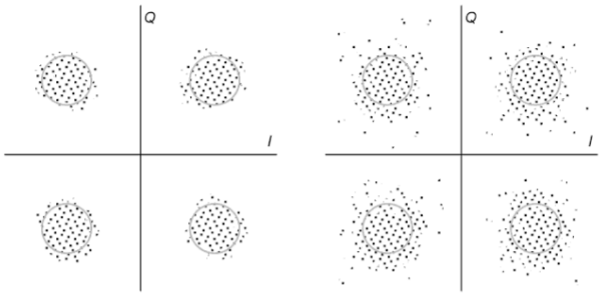

Figure 4.10: The different MER example [39].

Example of MER of QPSK modulation is shown in Figure 4.10. The first diagram shows an acceptable MER, on the other side the second one might cause misinterpretation due to larger variations of the received data. Generally, the less value is, the worse signal quality can be achieved. MER value is equal to [57]:

$$MER = \frac{\sum_{j=1}^{N}(\tilde{I}_j^2 + \tilde{Q}_j^2)}{\sum_{j=1}^{N}\left[(I_j - \tilde{I}_j)^2 + (Q_j - \tilde{Q}_j)^2\right]}, \tag{4.10}$$

where I_j is the I component of the j-th symbol received, Q_j is the Q component of the j-th symbol received, $\tilde{I}_j$ is the ideal I component of the j-th symbol received and, $\tilde{I}_j$ is the ideal Q component of the j-th symbol received.

4.5.4 Error Vector Magnitude

Error vector magnitude (EVM, see Figure 4.11) needs to save the position of the symbol given from the carrier wave in the output of the demodulator. This result is then compared with the theoretical location of the symbol in the I/Q diagram. The error in the position (distance difference) is shown on a percentage scale. EVM is related to the MER, and in practice, it describes the SNR of the digitally modulated signal in dB scale [39].

4.6 Eye Diagram

The most common way of representing digital signals is through the eye diagram (Figure 4.12). The eye diagram is widely used in all digital signals. In an eye diagram, many cycles of the

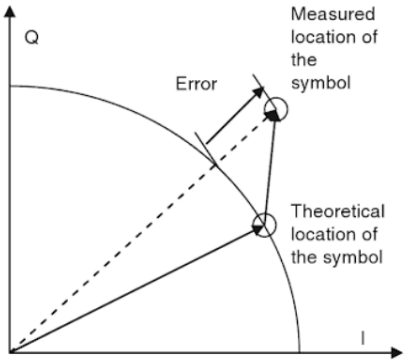

Figure 4.11: The principle of the error vector magnitude (EVM) [39].

signal are superimposed on top of each other, which highlights certain features otherwise not readily visible. It is a tool for showing long pattern dependencies in a signal. As a result, it characterizes the "quality" of the signal and to what extent a particular signal deviates from an "ideal" digital signal. Note that the eye diagram for an ideal digital signal is a rectangle [56].

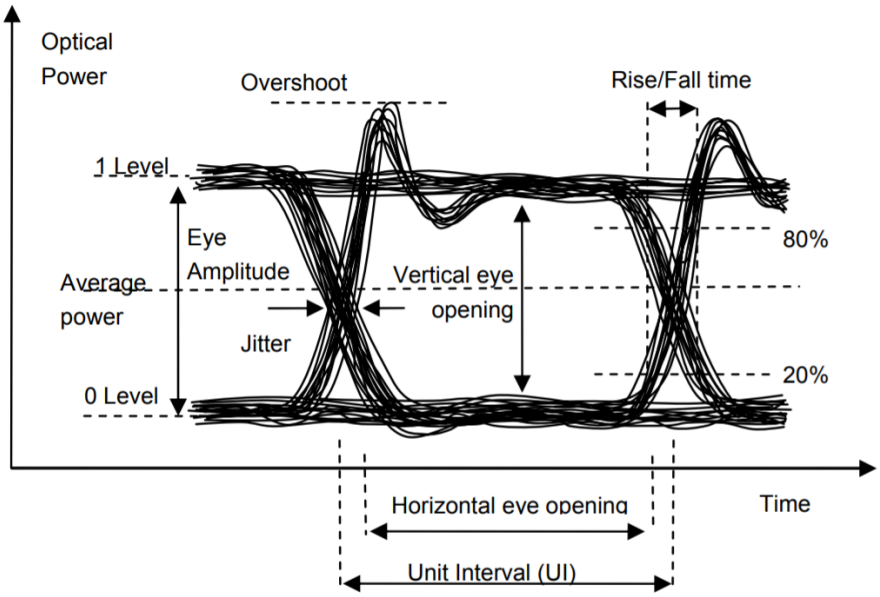

Figure 4.12: Eye diagram [56].

5 Description Of Rain

5.1 Microscopical Characterization

It is useful to focus on rain droplet description in microscopical approach and their spatial deployment. Generally, droplets are not formed in a shape of a sphere, but they are flattened. As the size increases, they get distorted, their shape is well approximated by oblate spheroids [1]. The flat base pulls out with an increasing radius to 4 mm to Pruppacher-Pitter shape shown in Figure 5.1.

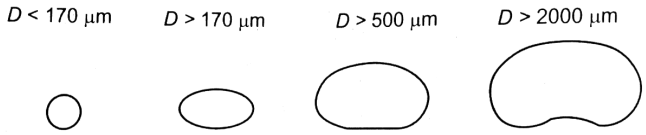

Figure 5.1: Rain droplet shapes depending on the diameter [17].

The size of raindrops ranges from hundreds of μm to about 4 mm in radius, but the size really depends on the actual atmospheric conditions (see Figure 5.2). Larger drops are hydrodynamically unstable and tend to break up and merge together again [1]. The wind has also an effect to a raindrop shape. It makes drop tilted [17].

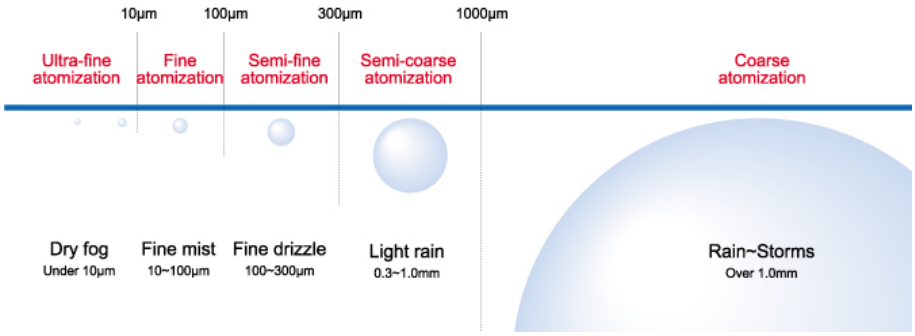

Figure 5.2: Classification of droplet size [37].

5.1.1 Velocity

The terminal velocity of falling drops (in stagnant air increases) with the drop size at a decreasing rate, reaching the maximum (about 9 m/s) at a radius of 2–3 mm. Beyond this size, the velocity slightly decreases. Finally, as the drop grows further, it breaks up. An analytical approximation of the terminal velocity of raindrops, as a function of the equivalent drop radius

in mm (equivolumetric sphere), is [2]:

$$v_t(r) = 9.65 - 10.3\, e^{-1.2r} \quad \text{(m/s)}. \tag{5.1}$$

Limiting speed of raindrop is also expressed by [26]:

$$V_a = \frac{2r^2 \rho g}{9\eta}, \tag{5.2}$$

where ρ is water density, g is gravitational constant, η is viscosity of air, and r is the radius of raindrop.

5.1.2 Rain Rate

Rain rate R is a measure of the intensity of rain by calculating the volume of rain that falls to the ground in a given interval of time. The rain rate is expressed in units of length (depth) per unit time (mm/hr), which is the depth of rain captured in a collection vessel per unit time.

From the terminal velocity and the PSD (Particle Size Distribution), it is possible to calculate the rain rate R, which is the basic meteorological and easily interpreted information for evaluating rain intensity and path attenuation [1]

$$R = 4.8 \cdot 10^{-3} \pi \int_{r_{min}}^{r_{max}} r^3 v_t(r) n(r) dr \quad \text{(mm/h)}, \tag{5.3}$$

for droplet radius r, where $n(r)$ is called *Raindrop Size Distribution*. According to [26], R can be expressed by

$$R = n(r) 1.33 (\pi r^3) V_a, \tag{5.4}$$

where V_a is the limit speed precipitation and r is the radius of raindrop (cm).

5.1.3 Raindrop Size Distribution

A precise description of spatial deployment in volume unit is difficult and it can be achieved using statistic model. Number of raindrops in a given volume (cubic meter) can be described by PSD or DSD (RainDrop Size Distribution) function $N(D)$ or $n(r)$ - numerousness drops of diameter D or radius r respectively. An accepted analytical form of PSD of rain is the gamma distribution whose general expression derived from Marshall-Palmer formula is [1]:

$$n(r) = N_0 r^{\mu} e^{-\Lambda r} \quad (\text{m}^{-3}\text{mm}^{-1}), \tag{5.5}$$

where μ is the shape parameter, which approximately ranges between -3 and 8, whereas N_0 and Λ are given by [1]:

$$N_0 = 6 \cdot 10^4 \mathrm{e}^{(3.2-\ln 5)\mu - \ln 5} \quad (\mathrm{m}^{-3}\mathrm{mm}^{-1-\mu}), \tag{5.6}$$

$$\Lambda = 0.2 \left[\frac{R}{33.31 N_0 5^{1+\mu} \Gamma(4.67+\mu)} \right]^{-\frac{1}{4.67+\mu}} \quad (\mathrm{mm}^{-1}) \ , \tag{5.7}$$

where $\Gamma(4.67+\mu)$ is function of Gamma distribution. Usually accepted value by [27] is $N_0 = 16 \cdot 10^3$ $\mathrm{m}^{-3}\mathrm{mm}^{-1}$. There is a need to mention the Gamma distribution is not the only model describing Raindrop Size Distribution. Other models include e.g. Exponential distribution, Constant μ gamma distribution, Constrained gamma distribution or Log-normal distribution [5].

5.2 Area Distribution

There are different types of rain with different spatial scales that range from a few kilometers in diameter to a few ten's of kilometers. Among these types, two major ones are *stratiform*, characteristic for its low intensity distributed all over the area (usually lower than 10 mm/h) with no lightning, and *convective*, characteristic for its high rain intensity, is generally heavy due to large drop size [17]. The example of measured flat rainfall distribution is shown in Figure 5.3.

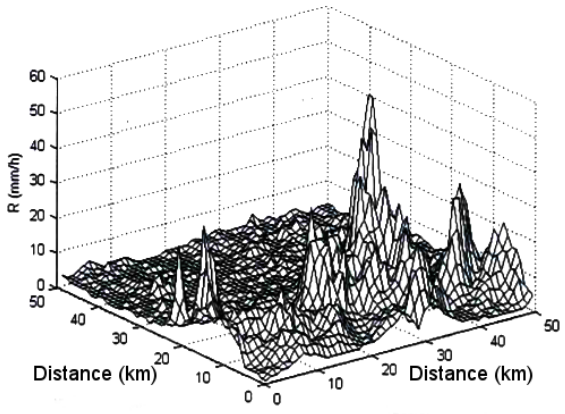

Figure 5.3: Flat rainfall distribution in a given time moment during one rainfall event [17].

5.2.1 Annual Precipitation

Precipitation (rainfall) very differs based on the specific geographical location (Figure 5.5). For instance, the mean annual one-minute rainfall rates in the eastern Malaysia range between 84.7

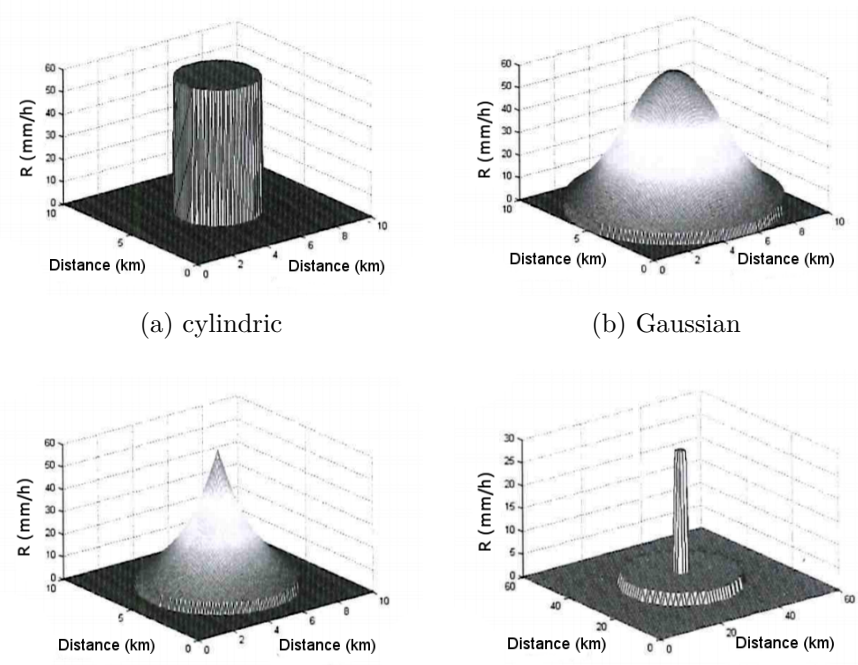

(a) cylindric (b) Gaussian

(c) exponential (d) Assis-Einloft

Figure 5.4: Flat rainfall distribution [17].

and 153.9 mm.h^{-1} for 0.01 % exceedance [51]. For Czechia, $R_{0.01}$ value is approximately 25 mm/h [17].

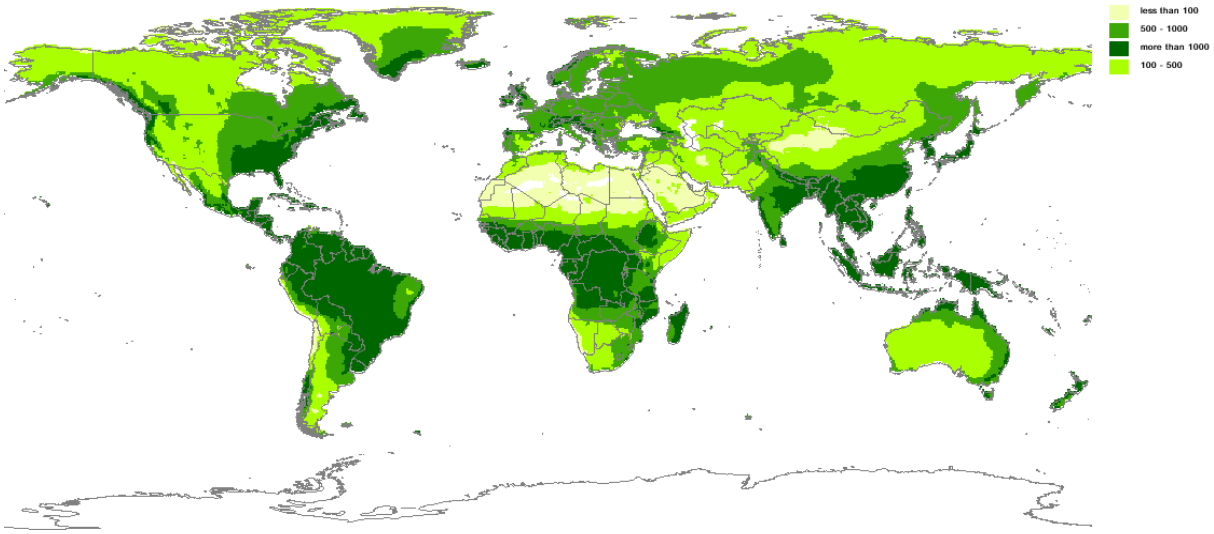

Figure 5.5: Mean annual precipitation 1950-2000 (mm/year) [54].

5.2.2 Exceedance

The term *exceedance* is explained in Figure 5.6 by so-called exceedance curves of rain rate computed using 13-year hourly rainfall records. The y values (commonly denoted as 'p') represent the percentage time of the year that a given rain rate is exceeded. The exceedance curve for the 13 years begins at 15 % of the year. This indicates that on an average the site experienced rain for 1314 h of the year [53].

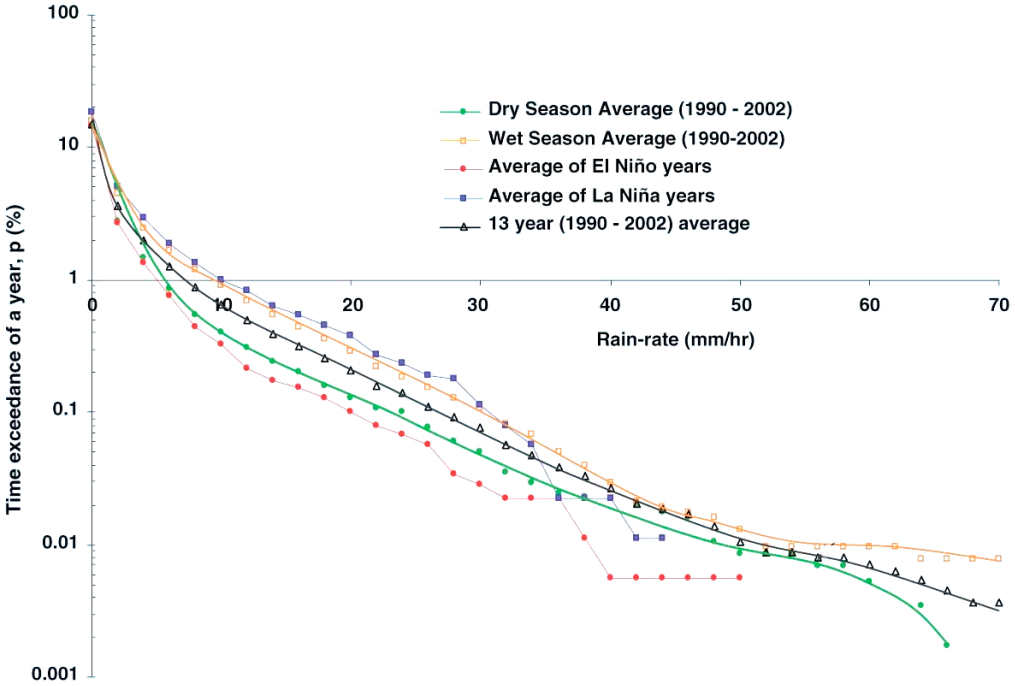

Figure 5.6: Example of rain rate exceedance curves in Suva, Fiji [53].

6 Effects of Rainy Weather Conditions on Optical Beam

The transmission of optical waves through the atmosphere can be noticeably influenced by adverse rainy weather. Despite of favorable conditions, the Earth's atmosphere is not an ideal medium for propagating optical waves. Only a few atmospheric windows are suitable for FSO due to the selective absorption by gases and water vapor. In clear sky conditions, the turbulence induced by temperature gradients results into random intensity fluctuations and loss of wavefront coherence. Finally, the interaction with solid and liquid water particles in adverse weather generates signal fades deep enough to produce link outage.

Rain is the most frequent weather impairment in temperate climate and it is the cause of various degradations when the wavelength becomes comparable to the drop size. Rain attenuation at optical bands is wavelength independent because the raindrop are much larger than the wavelength. Specific attenuation is usually estimated from the rain rate. Calculations show a high sensitivity to the PSD [1].

6.1 Applied Theories

Generally, the electromagnetic wave can be influenced by water droplet in two ways[17].

- *Attenuation.* The first one is describing droplet as lossless dielectric while incoming energy is absorbed. It can be referred as is a semi-conduct substance, where propagating wave inducts shifted currents causing temperature losses - attenuation of electromagnetic wave.

- *Scattering.* Inducted currents in droplets create secondary waves causing scattering to undesirable directions. This phenomenon causes attenuation in direction of propagating waves, and also a polarization plane spinning, i.e. creation of transverse polarization [17]. The scattering in rain (non-selective scattering) is independent on wavelength, and it does not introduce significant attenuation in wireless infrared links, scattering globally affects mainly on microwave and radio systems that transmit energy at longer wavelengths [26].

Using statistical methods is necessary considering random rainfall processes - both in time and in a space. It can be achieved by two different ways:

- *microscopic approach*, describing interaction between electromagnetic wave and raindrop of defined dimensions and shape and extending this description for the large number of drops placed in a given volume according to statistic method, and

- *macroscopic approach*, comes from longtime measuring of rainfall intensities and relative attenuation, when empiric models are created in relation of these quantities applicable for specific destination and for annual or month required probabilities of service availability

or rainfall occurrences [17]. The attenuation produced by rainfall increases linearly with rainfall rate [47].

6.2 Energy Losses by Particulates

Fog and rain consist of particles with identical optical properties. Their shape is spherical or can be parametrized with the radius r of an equivalent (i.e., equivolume) sphere. When an electromagnetic wave, traveling through a homogeneous medium as the air, enlightens a particle, part of the energy is absorbed by the particle and dissipated into heat and part is scattered. The scattered field is well approximated by a spherical wavefront, at a distance $R < r^2/\lambda$, begin λ the wavelength. The power flux subtracted from a plane wave propagating through a layer of randomly distributed particles is usually calculated by adding the contributors of the individual scatterers, through the *volume extinction coefficient*:

$$\beta(\lambda) = 10^{-3} \int_{r_1}^{r_2} C_{ext}(r, \lambda) n(r)\, \mathrm{d}r, \quad \text{(neper/km)} \tag{6.1}$$

where $n(r)$, namely the *particle size distribution* (PSD), represents the number of particles per unit of radius increment, C_{ext} is the *extinction cross section* of the particle, defined as the quantity that, once multiplied by the incident power density, returns the total power subtracted to the incoming wave and r is radius in µm.

The attenuation (i.e. the decrease in the energy flux) experienced by a plane wave traveling along the z/direction through a slab of length L, filled with with scatterers, which PSD is described by $n(r)$, is given by

$$I(z) = I_0 \exp\left\{\left[-\int_{r_1}^{r_2} C_{ext}(r) n(r)\, dr\right]\right\} z = I_0 \exp(-\beta z), \tag{6.2}$$

where I_0 is the incoming energy flux at $z = 0$. Equation 6.2, also referred to as Beer-Lambert law 3.1, gives the energy flux of the outgoing wave, when evaluated at $z = L$. The above equation clarifies the physical meaning of β, which is also called *specific attenuation*. In optics, the concept of transitivity (transmittance, see Equation 3.3) is used instead of β. It is defined as the fraction of energy flux transmitted through the lossy layer

$$T_a(z) = \frac{I(z)}{I_0} = \exp(-\beta z). \tag{6.3}$$

Two fundamental assumption are behind Equation 6.1 and 6.2.

1. *Independent scattering.* The interaction between the incident wave and each particle can be studied as if the other scatterers were not present. By consequence, the intensities of the scattered waves rather than their complex amplitude must be added. The above hypothesis is fulfilled if the distance among the particles is much larger than the wavelength, if they are randomly distributed in space and if the configuration is non-stationary in time. This is the case of atmospheric particles, which resemble a random population of scatterers, mixed up by wind and turbulence.

2. *Multiple scattering effects are negligible.* Each scatterer experiences a different disturbance composed by incident wave, attenuated by the previous particle layers along the propagation direction, and by the scattered waves. If the latter contribution is negligible, the light incident on each particle is well approximated by the original wave [10].

6.3 Attenuation

Equation 6.1 from section 6.2 is used for water particulates. It can be evaluated in dB/km as well by [3]:

$$\gamma = 4.343 \int C_{ext}(D, \lambda, m) n(D)\, \mathrm{d}D, \quad (\mathrm{dB/km}) \tag{6.4}$$

with C_{ext} in mm^2, diameter D in mm, wavelength λ in mm and the complex refractive index of water m. As previous chapters described, if particles are big ($r > 10\lambda$), which is definitely the case of raindrops and snowflakes in the optical region, then geometric optics rules: the incident wave is constituted by rays that obey to the classical laws of reflection, refraction, and diffraction. In such case, C_{ext} approaches twice the geometrical cross section of the particle, i.e. in the case of a sphere [1]:

$$C_{ext} = 2\pi r^2. \tag{6.5}$$

Based on Equation 6.4 the general form of specific rain attenuation equation, Equation 6.6 derived using power law approach to obtain power law coefficient using curve fitting or point matching techniques to find the values of a and b (often seen also as k and α). This making it in a simple power law formula and specific attenuation depends only on the rain rate R as follow:

$$\gamma = a \cdot R^b \quad (\mathrm{dB/km}). \tag{6.6}$$

Values for a and b depend on frequency, elevation of path Θ and polarizing tilt τ (for horizontal polarization $\tau = 0$ rad, for vertical polarization $\tau = \phi/2$ and for circle one $\tau = \phi/4$) and can be estimated by:

$$a = \frac{[a_H + a_V + (a_H - a_V)\cos^2\Theta \cos 2\tau]}{2}, \tag{6.7}$$

$$b = \frac{[a_H b_H + a_V b_V + (a_H b_H - a_V b_V)\cos^2\Theta\cos 2\tau]}{2a}. \tag{6.8}$$

Values of a_H, b_H, a_V and b_V comes from ITU-R Recommendation [43], but they are limited to frequencies from 1 to 1 000 GHz.

Several models are defined to fit given atmospheric conditions based on location and the current state of a weather. These empiric models were developed based on regression analysis and other methods of measured rain intensities (mm/h) and rain attenuation (dB) in their respected areas. Table 6.1 shows the values of a and b for these models [3], [14].

Table 6.1: a and b values of specific rain attenuation models of FSO.

Model	a	b	Country/Climate
Carbonneau	1.076	0.67	France/Temperate
Japan	1.58	0.63	Japan/Temperate
Grabner-Kvicera (Martin)	0.231	0.7	Prague (CZ)/Temperate
Samir	2.03	0.74	Malaysia/Tropical
Suriza	0.4195	0.8486	Malaysia/Tropical
Fiser-Brazda	1.6	0.63	Milesovka (CZ)/Temperate

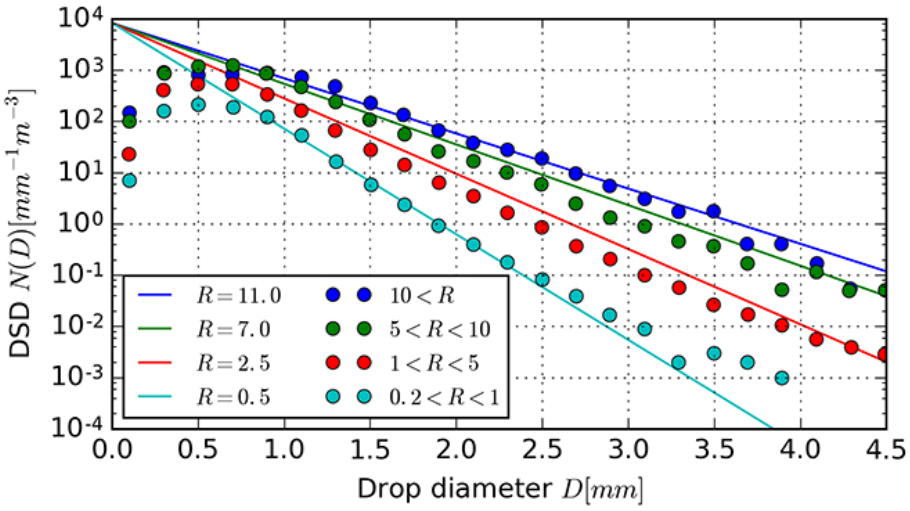

Figure 6.1: DSD measured in Czechia (one year measurement, rain rate R is the parameter of particular sets of points). Lines represent the theoretical value [13].

Comparisons of specific rain attenuation models shown in Figure 6.2 Carbonneau and Japan models recommended by ITU gave average attenuation compare with other models. Values for a and b can be also specific for RF spectrum, as shown in [13].

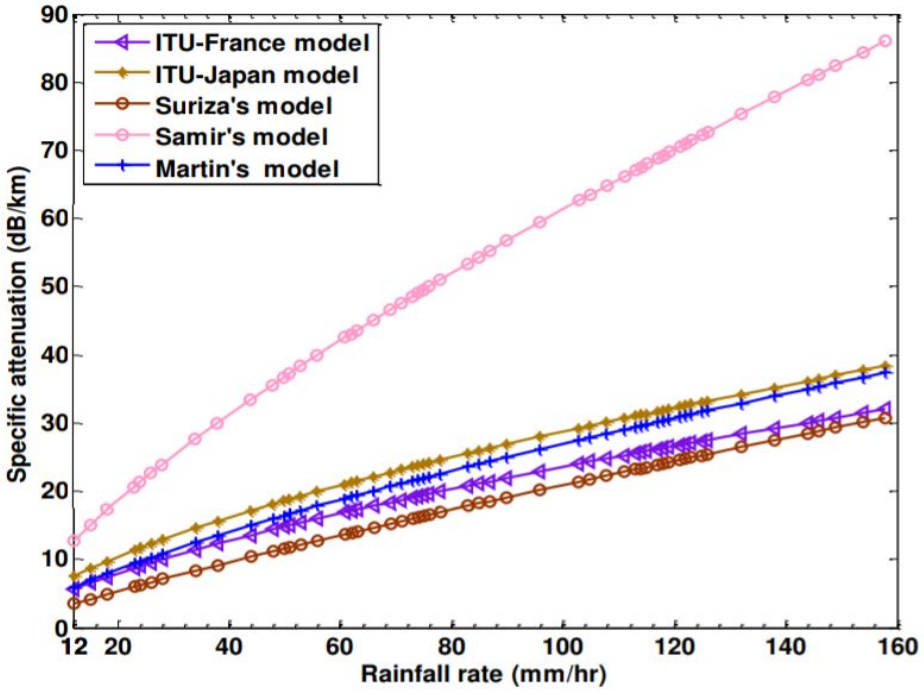

Figure 6.2: Comparison of specific ran attenuation of different FSO models [3].

In Table 6.2 estimated attenuation were calculated based on experimental measurements. These loses are given by a number of software systems prepared by the Air Force Geological Laboratory (AFGL) at Hanscom Air Force Base. This data can help to estimate the range between laser repeater stations as well as give us a measure of BER. Importantly, it is the major challenge that laser communications face because the laser links must at times operate in inclement weather [19]. Another description provided by [27] is shown in Table 6.3, where the relation between attenuation and the precipitation rate is shown.

Table 6.2: Estimated attenuation by the Air Force Geological Laboratory.

Rain rate (mm/h)	Wavelength (µm)	Attenuation (dB) at distance (km)		
		1	10	100
5	0.53, 1.06	1.6	16	160
25	0.53, 1.06	4.2	42	420
75	0.53, 1.06	7.0	70	700

Table 6.3: Relation between attenuation and the precipitation rate.

Attenuation	Relation	980 and 1550 nm
Drizzle or light rain ($R < 3.8$)	$0.509R^{0.63}$	0.79 dB/km ($R = 2$)
Mean rain ($3.8 < R < 7.6$)	$0.319R^{0.63}$	0.88 dB/km ($R = 5$)
Strong rain (storm) ($R > 7.6$)	$0.163R^{0.63}$	1.08 dB/km ($R = 20$)
Rain (Marshall-Palmer)	$0.365R^{0.63}$	1.56 dB/km ($R = 10$)
Rain (Carbonneau)	$1.076R^{0.67}$	5.06 dB/km ($R = 10$)

Table 6.4: Visibility range based on rain rate

Rainfall type	Rain rate (mm/h)	Visibility range, V (km)
Heavy rain	25	1.9–2
Medium rain	12.5	2.8–40
Light rain/drizzle	0.25	18–20

According to [47], the rain attenuation for FSO links can be approximated by empirical formula:

$$\gamma = \frac{2.8}{V}, \tag{6.9}$$

where V is visibility range in km and its values based on rain rate is (see Table 6.4).

6.3.1 Anomalous Diffraction

It was formulated an approximated theory called anomalous diffraction for the large values of the size parameter and with spheres of refractive index close to one (in magnitude), which is the optical case of liquid water. An empirical correction produces errors on Q_{ext} (dimensionless parameter called *extinction efficiency*) within 30 % in the range $1.01 \leq \nu \leq 2.00$ and $0 \leq \kappa \leq 10$, in complex refractive index for any value of r/λ. The anomalous diffraction is a good approximation to calculate the attenuation by water particles from the optical band to the mid-IR range [1].

6.3.2 Scattering

Scattering due to rainfall is called non-selective scattering, this is because the radius of raindrops (100–1000 µm) is significantly larger than the wavelength of typical FSO systems. The laser is able to pass through the raindrop particle, with less scattering effect occurring. The haze particles are very small and stay longer in the atmosphere, but the rain particles are very large and stay shorter in the atmosphere. This is the primary reason that attenuation via rain is less

than haze. On the other hand, RF wireless technologies that use frequencies above approximately 10 GHz are adversely impacted by rain and little impacted by fog. This is because of the closer match of RF wavelengths to the radius of raindrops, both being larger than the moisture droplets in fog. The rain scattering coefficient can be calculated using Stroke Law [26]:

$$\beta_{rainscat} = \pi r^2 n(r) Q_{scat} \left(\frac{r}{\lambda}\right), \tag{6.10}$$

where r is the radius of raindrop (cm), N_a represents the raindrop distribution (cm $^{-3}$) and Q_{scat} stands for the scattering coefficient.

According to [27], the scattering cross section is equal to 2 for raining conditions and the scattering coefficient equals:

$$\beta_{rainscat} = 10^5 \int_0^\infty 2\pi r^2 \frac{dn(r)}{dr} dr, \tag{6.11}$$

where $n(r)dr$ is Raindrop Size Distribution (see Equation 5.5)

6.3.3 Longterm Statistical Models

Another approach to calculate the attenuation caused by rain is with usage longterm measuring experimental paths and rainfall intensities with a rain gauge or meteorological radars. Based on this approach rain attenuation can be estimated for a given area and required a time of availability [17].

Due to inhomogeneous of rain, while propagating along the path, the rain might not fall into the entire propagating path. Cause some portion of the link to be affected. This is so-called effective path link, which defines as the intersection between rain cell and path length. It is confirmed from this definition that the effective path length is smaller than total actual path [3].

According to ITU recommendation[4], the total path attenuation exceeded for 0.01% of the time can be estimated also with 6.6 by:

$$A_{0.01\%}(dB) = \gamma \cdot d_{eff} = a \cdot R_{0.01}^b \cdot d_{eff}, \tag{6.12}$$

where γ is the specific rain attenuation in dB/km and d is total path length in km, r is reduction (distance) factor, $R_{0.01}$ is rainfall intensity in mm/h (measured after the first minute) exceed for 0.01% of the time and d_{eff} is effective path length. There are many models has been developed to estimate the value of r based on rain intensity, total path length or both of them [3]. It is possible to choose statistic for *average year* or for so-called *the worst month*.

Recommendation ITU-R P.837 [15] provides the rainfall rate $R_{(p)}$ (mm/h) exceeded for any given percentage of the average year, p, and for any location, and Equation 6.6 provides the specific attenuation exceeded for the time percentage p.

6.3.4 Light Behavior Propagating Through Droplet

As already mentioned, when an electromagnetic wave, traveling through a homogeneous medium as the air, enlightens a particle, part of the energy is absorbed by the particle and dissipated into heat and part is scattered. When a plane wave propagating in the vacuum enters a homogeneous region of space with complex refractive index $n = \nu - i\kappa$, it undergoes changes in its velocity, phase, and direction depending on ν, and, at the same time, if $\kappa > 0$, it is attenuated.

The optical properties of water are strongly wavelength dependent throughout the spectrum considered. In the visible and the IR up to about 2 µm, water behaves almost as a transparent dielectric ($1.306 < \nu < 1.339$ and $\kappa < 10^{-3}$). ν increases throughout the mid-IR and roughly doubles with respect to the visible region at the lower edge of the millimeter wave range, whereas κ grows by several orders of magnitude and becomes on the order of unity around 100 µm [1].

In a geometrical point of view, e.g. in case of rainbow phenomena, the sunlight is refracted and decomposed to colors of the visible spectrum, since the refraction index is spectrum-dependent (see Figure 6.3).

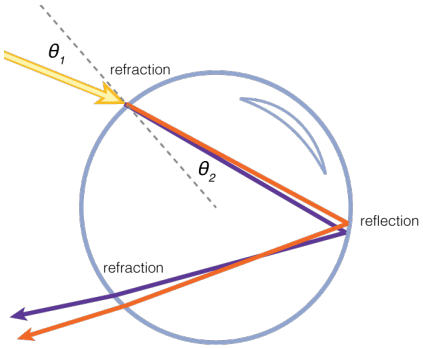

Figure 6.3: Sunlight behavior on water droplet.

But it is not a case of FSO, since this technology uses narrow monochromatic sources of light, not white sunlight composed of the spectrum of colors. As the laser beam propagates through the rainfall, the beam is being wandered as described in Section 3.6. The example trajectory is shown in Figure 6.4.

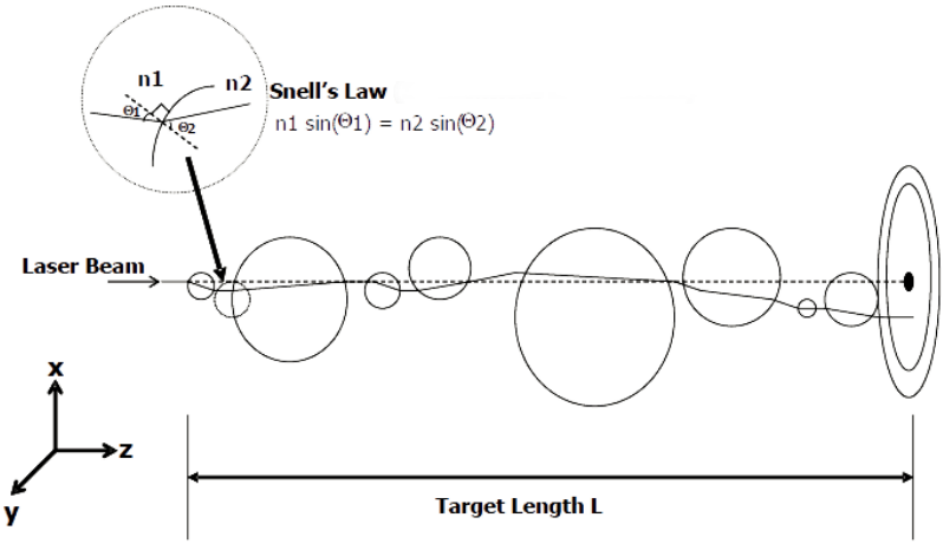

Figure 6.4: Laser beam propagation through droplets.

6.4 Architecture Impact

Rain intensity also has a significant impact based on using specific network architecture. As the paper by Vavoulas et al. proves [16], the increase of rain intensity from light rain to medium rain significantly increases the number of required nodes by a factor of 3 with using a network with node distribution model (multiple-hop FSO network, where the nodes are distributed at fixed positions on a given path-link). When the rain conditions worsen, this factor further increases to 5. An extreme amount of precipitation (> 90 mm/h) requires a high density node deployment, so it is critical to collect the rainfall rate data at different intervals of the year in order to achieve a trade-off between network availability and the number of required nodes to achieve low values of isolation probability P_{iso}. See the impact of rain attenuation is in Figure 6.5.

The most fundamental modulation schemes used in optical wireless systems are on–off keying (OOK) and pulse position modulation (PPM). For the OOK and PPM scheme, the experimental measuring was made with different rain rates [16].

Table 6.5: Number of required nodes and supported data rate for $P_{iso} = 10^{-3}$ and $P_e = 10^{-6}$.

	OOK			PPM		
	1 Mbps	100 Mbps	1 Gbps	1 Mbps	100 Mbps	1 Gbps
$R = 2.5$ mm/h	24	32	38	22	29	34
$R = 12.5$ mm/h	60	75	86	57	70	79

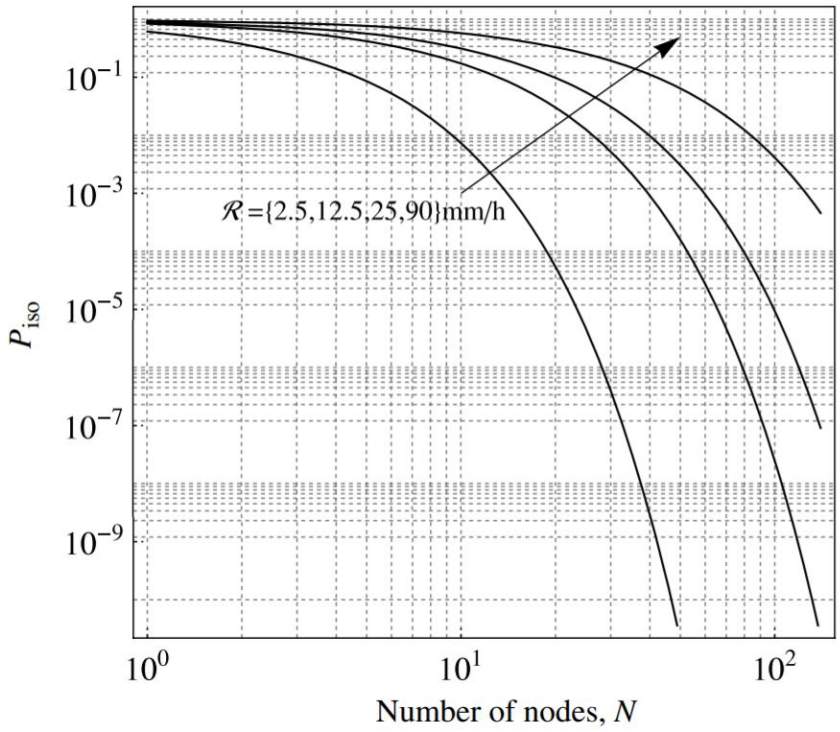

Figure 6.5: Node isolation probability versus number of nodes and rain conditions [16].

Table 6.5 displays the required number of nodes in order to cover a network length of $L = 50$ km assuming the previously mentioned modulation schemes and achieved probability of error, $P_e = 10^{-6}$. In general, the use of PPM is more profitable as the supported data rate increases for a given weather condition.

6.4.1 Possible Solutions of Power Loss

If the optical path is negatively influenced by unfavorable conditions, there is essential need to use adaptive optics that is able to control the output optical power to reach the detector and therefore compensate for the power fluctuations due to turbulence and other atmospheric phenomena in an urban scenario. Several techniques were proposed, such as a spatial transmitter or receiver diversity, adaptive beam forming based on the wavefront phase error measurement, wavelength diversity, multiple-beam communication or new modulation technique [55].

7 Mathematical Modeling of the Environment

7.1 Fluid Parameters

7.1.1 Reynolds Number

The Reynolds number (Re) is the ratio of inertial forces to viscous forces and is a parameter for predicting if a flow condition will be laminar or turbulent. By [51], it can be interpreted that when the laminar forces are dominant ($Re < 1000$) they are sufficient enough to keep all the fluid particles in layers. When the viscous forces dominate ($Re > 1000$) then the flow is turbulent (particles swirl). Values for classifying of flows in a special conditions is provided also by [50]. Number is given by [51]:

$$Re = \frac{dV_n\rho_g}{\nu_f}, \tag{7.1}$$

where d is a characteristic linear dimension (aerosol diameter when dealing with spray system) in m, V_n is the maximum speed of the object relative to the fluid (the gas velocity in m/s), ρ_g is the gas density (kg/m^3), and μ_f is the dynamic viscosity of the fluid (gas, kg/m·s).

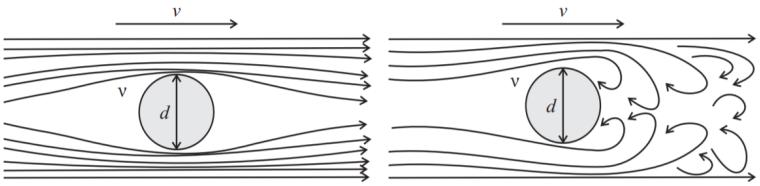

Figure 7.1: Laminar and turbulent flow [8].

7.1.2 Weber Number

The Weber number in the gas and liquid is defined as the ratio of aerodynamic force to the force generated by surface tension and given by [33]:

$$We = \frac{\rho v^2 l}{\sigma}, \tag{7.2}$$

where v is the jet velocity, l is the nozzle/droplet diameter, ρ is density, and σ represents the surface tension.

7.1.3 Ohnesorge Number

The Ohnesorge number is defined as the ratio between viscous forces and surface tension forces and has the form [33]:

$$Oh = \frac{\sqrt{We}}{Re}, \tag{7.3}$$

7.2 Turbulent Models

Since the laboratory model fulfills concept and criteria of turbulent flow, following chapter includes a brief description of main turbulent models used for numerical prediction. Each model is available in ANSYS Fluent software used for modeling described in Section 7.3.

7.2.1 Reynolds-Averaged Navier-Stokes Models

Models are based on time-averaged equations of motion for fluid flow. The idea is Reynolds decomposition, whereby an instantaneous quantity is decomposed into its time-averaged and fluctuating quantities. There are a lot of models based on RANS categorized into several groups. RANS models fall into one of two main groups. Eddy Viscosity Models (EVM) and Reynolds Stress Models (RSM). Following list contains models available in ANSYS Fluent software. Some of them can be applicable with Detached Eddy Simulation models in the software as well [21].

- Eddy Viscosity Models,
  - Spalart-Allmaras (S-A) Model (One-Equation Model),
  - k–ε Model Family (One-Equation or Two-Equation Models),
    - Standard k–ε Model,
    - Realizable k–ε (RKE) model,
    - RNG k–ε (RNG) model.
  - k–ω Model Family,
    - Standard k–ω (SKW) model,
    - Shear Stress Transport k–ω (SSTKW) Model.
  - k-kl-ω Model (Three-Equation Model),
  - Transition SST model.
    - Intermittency Transition Model.
- Reynolds Stress Models,
- Unsteady RANS.
  - Scale-Adaptive Simulation (SAS).

7.2.2 Large Eddy Simulation

Turbulent flows are characterized by eddies with a wide range of length and time scales. The largest eddies are typically comparable in size to the characteristic length of the mean flow (for example, shear layer thickness). The smallest scales are responsible for the dissipation of turbulence kinetic energy. In LES, large eddies are resolved directly, while small eddies are modeled. Large eddy simulation (LES) therefore falls between DNS and RANS in terms of the fraction of the resolved scales. ANSYS Fluent offers Embedded Large Eddy Simulation (ELES) with improved techniques [21].

7.2.3 Detached Eddy Simulation

The DES models, often referred to as the hybrid LES/RANS models, combine RANS modeling with LES for applications such as high-Re external aerodynamics simulations. The computational costs, when using the DES models, is less than LES computational costs, but greater than RANS. ANSYS Fluent offers five different models for the detached eddy simulation: the Spalart-Allmaras model, the realizable - model, the BSL - model, the SST - model, and the Transition SST model [21].

7.3 Multi-phase Flow

7.3.1 General Description

The term multi-phase flow is used to refer to any fluid flow consisting of more than one phase or component. Virtually every processing technology must deal with the multiphase flow. The ability to predict the fluid flow behavior of these processes is central to the efficiency and effectiveness of processes. Multiphase flows are also a ubiquitous feature of our environment whether one considers rain, snow, fog, avalanches, mudslides, sediment transport, debris flows, and countless other natural phenomena [22].

A large number of flows encountered in nature and technology are a mixture of phases. Physical phases of matter are gas, liquid, and solid, but the concept of phase in a multiphase flow system is applied in a broader sense. In multiphase flow, a phase can be defined as an identifiable class of material that has a particular inertial response to an interaction with the flow and the potential field in which it is immersed. For example, different-sized solid particles of the same material can be treated as different phases because each collection of particles with the same size will have a similar dynamical response to the flow field [21].

7.3.2 Classification

7.3.2.1 Topologies

Two general topologies of multiphase flow can be usefully identified as *disperse flows* (or *discrete*) and *separated flows*. By disperse flows we mean those consisting of finite particles, drops or bubbles (the disperse phase) distributed in a connected volume of the continuous phase. Separated flows consist of two or more continuous streams of different fluids separated by interfaces [22].

7.3.2.2 Regimes

Multiphase flow regimes can be grouped into four categories categorized by type of reacting fluids: gas-liquid or liquid-liquid flows; gas-solid flows; liquid-solid flows; and three-phase flows [21].

7.3.3 Flow Models

A persistent theme of multiphase flows is the need to model and predict the behavior of those flows and the phenomena. There are three ways in which such models are explored [22]:

1. experimentally, through laboratory-sized models equipped with appropriate instrumentation,
2. theoretically, using mathematical equations and models for the flow, and
3. computationally, using the power and size of modern computers to address the complexity of the flow.

For a purpose of this paper, computational modeling based on mathematical equations is the default tool for modeling rainy conditions of the experimental box described in Section 8.1. Section 7.3 is focused on computational modeling using software ANSYS Fluent.

7.3.4 Approaches to Multiphase Modeling

Advances in computational fluid mechanics have provided the basis for further insight into the dynamics of multiphase flows. Currently there are two approaches for the numerical calculation of multiphase flows: the *Euler-Lagrange approach* and the *Euler-Euler approach*. More details about both of these approaches can be found at ANSYS Fluent Theory Guide [21].

7.3.4.1 The Euler-Lagrange Approach

The Lagrangian discrete phase model in ANSYS Fluent follows the Euler-Lagrange approach. The fluid phase is treated as a continuum by solving the Navier-Stokes equations, while the dispersed phase is solved by tracking a large number of particles, bubbles, or droplets through

the calculated flow field. The dispersed phase can exchange momentum, mass, and energy with the fluid phase [21].

This approach is made considerably simpler when particle-particle interactions can be neglected, and this requires that the dispersed second phase occupies a low volume fraction, even though high mass loading ($m_{particles} \geq m_{fluid}$) is acceptable. The particle or droplet trajectories are computed individually at specified intervals during the fluid phase calculation. This makes the model appropriate for the modeling of spray dryers [21].

For applications such as these, particle-particle interactions can be included using the Discrete Element Model and Collision and Droplet Coalescence Model, where ANSYS Fluent provides an option for estimating the number of droplet collisions and their outcomes in a computationally efficient manner [21].

7.3.4.2 The Euler-Euler Approach

In the Euler-Euler approach, the different phases are treated mathematically as interpenetrating continua. Since the volume of a phase cannot be occupied by the other phases, the concept of phasic volume fraction is introduced. These volume fractions are assumed to be continuous functions of space and time and their sum is equal to one. Conservation equations for each phase are derived to obtain a set of equations, which have a similar structure for all phases. These equations are closed by providing constitutive relations that are obtained from empirical information, or, in the case of granular flows, by application of kinetic theory. In ANSYS Fluent, three different Euler-Euler (grouped directly in Multiphase category) models are available: the volume of fluid (VOF) model, the mixture model, and the Eulerian model [21].

8 Experimental Measurement

A rainfall system was designed using special nozzles designed for industrial use, such as container cleaning, etc. for an observing the behavior of the optical beam in simulated rainy conditions. A set of three nozzles were used which differed in the size of the sprayed particles.

8.1 Simulation-Experimental Lab Box Environment

8.1.1 Droplet Distribution

To be able to applicate experimental model in this paper, the description of a nozzle is used for similarity with the generating raindrop in nature while rainy conditions take main effects. According to the empirical observing of the fluid injection, the convective type can be assumed as a default state (see Section 5.2). The flat rain distribution cannot be clearly determined.

Nozzle injections (like spray, its multi-phase flows are well documented in many sources and can be used as reference) are formed when the interface between a liquid and a gas becomes deformed and droplets of liquid are generated. These then migrate out into the body of the gas. Sometimes the gas plays a negligible role in the kinematics and dynamics of the droplet formation process; this simplifies the analyses of the phenomena. The unsteady, turbulent motions in the gas generate ligaments of liquid that project into the gas and the breakup of these ligaments creates the spray. The jet may be laminar or turbulent when it leaves the nozzle [22].

8.1.2 Assembly

Two ready made polymethyl methacrylate boxes placed next to each other were used to create the rain fall with an inserted metal tube structure to attach the water nozzles. This construction is inserted into the box and wrapped around with a transparent foil to prevent water leakage out of the box. The box plays a role as a big "rain gauge" to help to compute the total amount of precipitation known as *rain rate*. To not waste the water, it flows into a vat which makes it circulate with no jolt of water. Water is pumped through the water pump into the water supply, which starts with a regulator controlled by an application created by National Instruments^{TM} LabVIEW. It is a virtual instrumentation program that is able to create a number of real-time applications with the help of special libraries and hardware devices that make communication between the PC and the component. For the experimental needs, the DAQ USB 6001 was used, see manual [32], where analog controller output, one analog input for pressure measurement and a digital pulse counter for flow measurement were used. From the controller, the water passes through a flowmeter to monitor the amount of water entering the nozzles. The flow meter produces a rectangular pulse that passes the DAQ card through the water passage and evaluates the amount of water in the program that depends on the number of given pulses. Four

branches for each box were used where three nozzles end and one branch is used for pressure sensing. The nozzles are mounted on sliding mounts to optimize the coverage by drops. The schematic diagram of a half of the assembled box is shown in Figure 8.1.

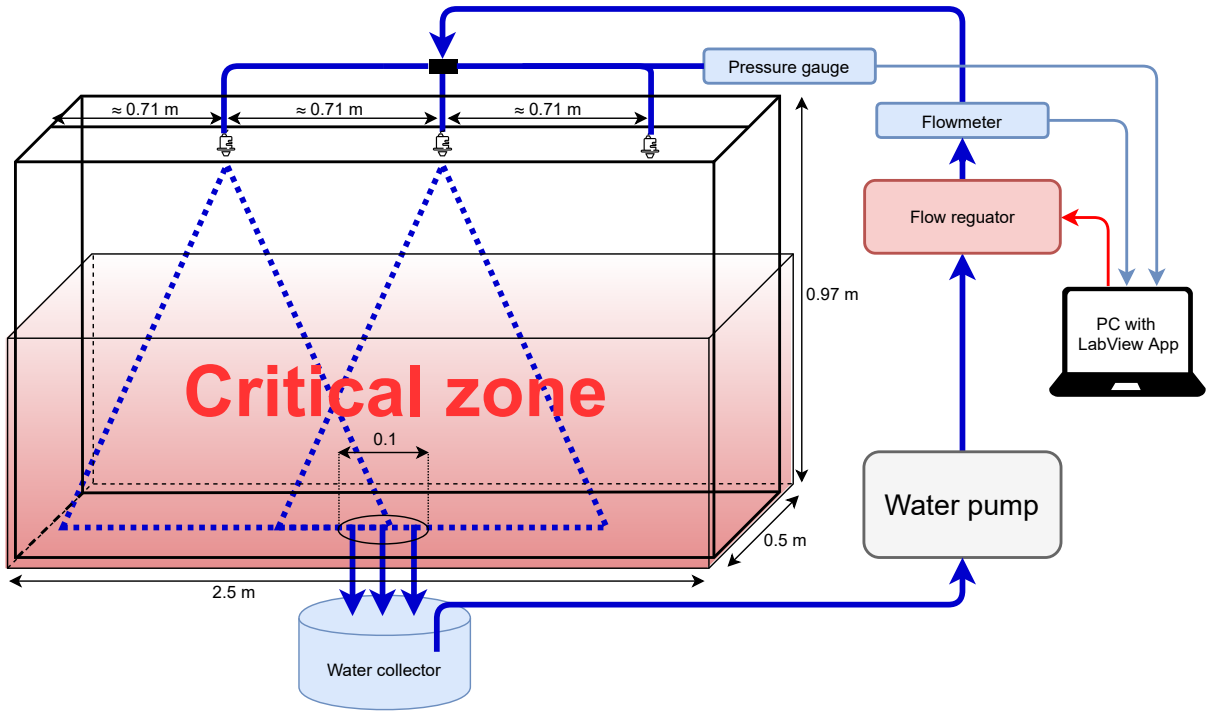

Figure 8.1: Chart of the one lab box (dimensions in m).

Sensors

In order to measure the atmospheric conditions within the box, a set of sensors based on the IoT system was used - Arduino platform with the BME280 module for measuring atmospheric temperature, humidity and pressure. The MQTT protocol was used for communication with LabVIEW application.

Types of Used Nozzles

For simulating as many different types of rain as possible, the experiment was based on three different nozzle types for industrial purposes. Overview of chosen HYDRO SPARE PARTS nozzle series called FP-FulcoJet^{TM} Full Cone Nozzle [31] is shown in a Table 8.1.

Other Equipment

The following components were required for the experiment. The Gardena 5000/5 garden water pump with a maximum pressure of 5 bar and other components such as hoses and fasteners were

Figure 8.2: Used nozzle types.

Table 8.1: Default values of used nozzles (BSP - British Standard Pipe as a reference).

Nozzle	Thread	Color	Cone Angle at 1 bar	Flow Rate (l/min of Water at 20 °C)							
				Pressure (bar)							
				0.5	1	2	3	4	5	7	10
90B1FP1	1/8" BSP	Orange	30°	0.32	0.46	0.64	0.79	0.91	1.02	1.21	1.44
90B1FP3	1/8" BSP	Lime Green	50°	0.97	1.37	1.93	2.37	2.74	3.06	3.62	4.32
90B1FP3.5	1/8" BSP	Terracotta	60°	1.13	1.60	2.26	2.76	3.19	3.57	4.22	5.05
90B2FP6.5	1/4" BSP	Purple	50°	2.10	2.96	4.19	5.13	5.93	6.63	7.84	9.37

purchased to pump water. Siemens SSD31 was used as the electronic controller, which allows an opening to be set with a voltage of 0 to 10 V.

The flowmeter operates on the principle of generating rectangular pulses to calculate the current flow rate or the total flow rate. In addition, a pressure gauge B+B Thermo-Technik DRTR-AL-10V-R10B was attached.

Flow Rate Control Application

For the monitoring purposes, control application in LabVIEW environment was used (see Appendix C.1). Flow rate can be regulated and monitored as well as the current value of pressure.

8.2 High-Speed Camera Capturing

Capturing photographs (Figure 8.3) for measuring real droplets is useful for getting values used later for modeling purposes (see Section 9). It was enabled to approximate a diameter of the water drop by using the Fiji program to measure distance with a known reference length. Editor GIMP was used to improve the quality of final images. Droplet diameter for 90B2FP6.5 nozzle ranges approximately from 300 to 3000 µm. By Figure 5.2, the drop sizes can be classified as a light rain and/or a rain-storm.

8.3 Methodology

Droplet effects are examined by MER value of the modulation for the selected modulation that is set in the LabVIEW environment, and using the USRP device. Two USRPs (model 2920 by National Instruments^{TM}) were used, one as a modulator and the other for subsequent

Figure 8.3: High-speed camera image of water nozzle (type 90B2FP6.5).

demodulation, and obtaining values for a given modulation. The OOK was observed. For several rain rates given by flow rate and nozzle size, they were subsequently evaluated for their resistance to particular rainy conditions.

Light described in Communication channel were measured for 5 minutes for the modulation with given bit rate and rain rate, from which the mean MER was obtained by an exploration analysis to be used to compare the individual conditions, as well as hypotheses to determine a statistical significance.

8.3.1 Communication Channel

Above the path of the optical beam, six nozzles were placed (three in each box) for creating raindrops. They affected the light itself and increased attenuation. Both optical source and detector were placed in the critical area shown in Figure 8.1.

On-Off keying was chosen as a testing modulation. Modulation was measured for five minutes and evaluated. Three nozzle types were used for the final experiment since the nozzle with the smallest orifice did not generate adequate DSD comparable to real rain conditions. The modulator handled laser diodes with a length of 650 nm (type L-SLD6510A).

Diagram of the communication channel can be seen in Figure 8.4.

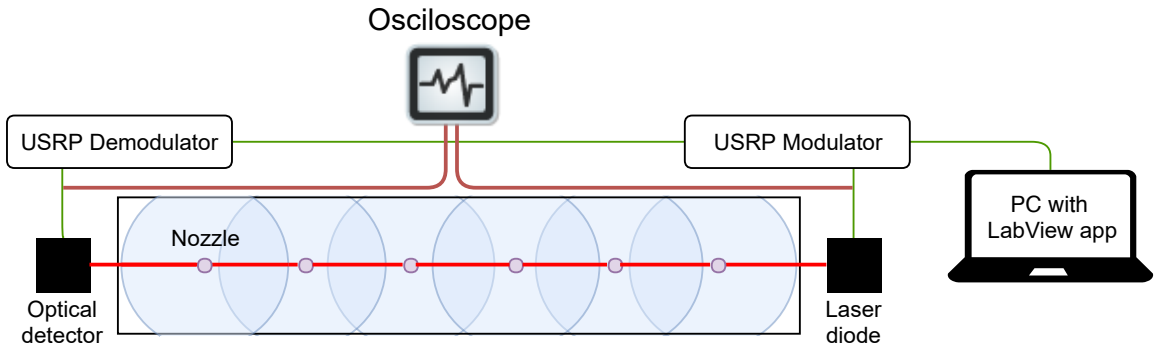

Figure 8.4: Optical path - box upper view.

8.3.2 Rain Rate Measuring

To be able to calculate the real value of the rain rate, it is necessary to obtain it from the mass flow rate measured by the application described in the Section 8.1.2.

To convert l/min to mm/h, it was needed to found out the height of a rainfall water volume in the box for 1 hour. For the flow rate $Q = 1$ l/min, $Q = 60 \cdot 1$ l/h $= 60$ l/h $= 0.06$ m^3/h. For box dimensions (width $w_b = 0.5$ m, length $l_b = 5$ m), a volume of water $V_w = 0.06$ m^3 and unknown height of the water volume h_w, the volume of water is given by:

$$V_w = w_b l_b h_w, \quad h_w = \frac{V_w}{w_b l_b}, \quad h_w = 0.024 \text{ m}. \tag{8.1}$$

To sum up, the mass flow $Q = 1$ l/min equals a rain rate $R = 24$ mm/h for given laboratory conditions.

8.3.3 Atmospheric Conditions

Atmospheric condition measuring was done by the sensor set described in Section 8.1.2. Reference values are shown in Table 8.2.

Table 8.2: Mean values of atmospheric parameters for 90B2FP6.5.

	64	80	120	144
Temperature (°C)	21.54	20.92	20.90	20.33
Humidity (%)	99.58	99.80	99.88	99.94
Pressure (hPa)	993.80	993.95	994.02	994.28

8.4 Measuring and Evaluation

For a sample analysis (valid for the modulation), following values are set as default:

- nozzle 90B2FP6.5,
- rain rate $R = 120$ mm/h,
- bit rate $B = 10$ Mbps,

unless otherwise stated.

8.4.1 Power Attenuation

Each value was averaged from 2000 samples to measure the power level. Measured data is presented in Table 8.3.

As described in 8.5 and 8.6, the increasing nozzle's orifice should decrease the attenuation caused by the decreasing count of generated water droplets from this nozzle. But the 3.5 type is attenuated the most. Explanation of this situation could be a collapse of the cone model since less pressure caused by decreased mass flow rate has a degradation impact for the shape of the generated droplet area; it changes from hollow to solid (full cone) type (See Figure 9.8). In case of changing the rain rate, the power laws apply. With increasing amount of water, the received power decreases.

Table 8.3: Attenuation of received power by rainy conditions (dB).

	R (mm/h)	64	80	120	144
90B1FP3	$\bar{A}$	0.38	0.58	1.21	1.68
	s_A	0.02	0.02	0.03	0.04
	Sample count	66	71	75	59
90B1FP3.5	$\bar{A}$	0.56	0.70	1.24	1.65
	s_A	0.02	0.04	0.03	0.03
	Sample count	73	72	73	72
90B2FP6.5	$\bar{A}$	0.30	0.41	0.70	0.78
	s_A	0.03	0.03	0.03	0.03
	Sample count	73	68	66	68

Theoretical Verification

In order to use very high values of rain rates, available in the certain parts of the world, Malaysian Samir formula (Table 6.1) were used for verification of measured values. Using Equation 6.6 for 90B2FP6.5 were obtained results (see Table 8.4).

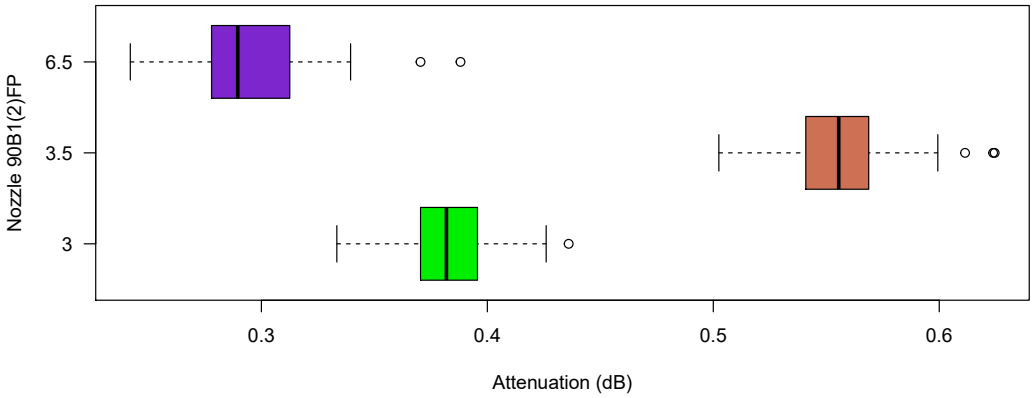

Figure 8.5: Attenuation for $R = 63$ mm/h.

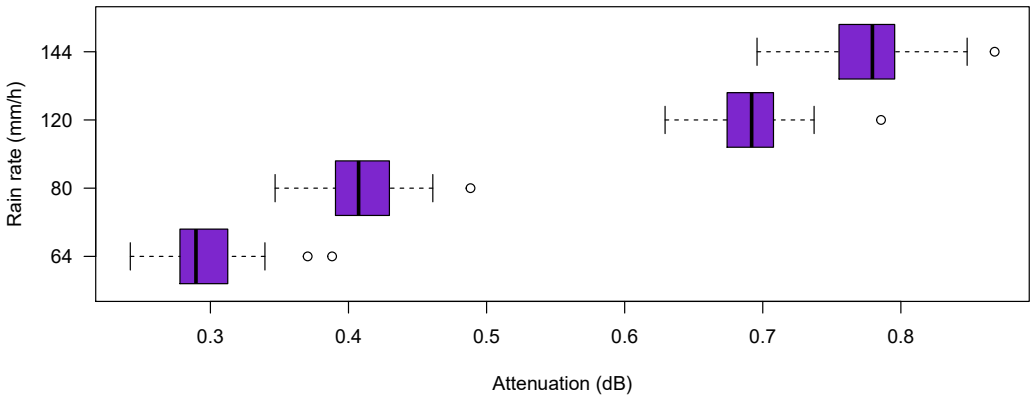

Figure 8.6: Attenuation for 90B2FP6.5 nozzle.

Table 8.4: Comparison of theoretical and measured values.

R (mm/h)	60	80	120	144
A (dB)	0.3	0.41	0.7	0.78
Theoretical Value (dB/km)	44.06	51.97	70.16	80.29
Measured Value (dB/km)	60	82	140	156

8.4.2 Modulation Degradation

A closer look at the match of results will be provided by the statistical analysis for the modulation degradation. It is necessary to execute several steps:

1. exploration analysis,
2. normality test,
3. homogeneity of variance test (homoscedasticity),
4. analysis of variance test,
5. post-hoc analysis (if needed).

If all data groups meet normality and homoscedasticity assumptions, ANOVA mean value test may be used, otherwise, a nonparametric Kruskal-Wallis median test. If the zero hypotheses, H_0, of the individual tests are not met, the alternative hypothesis, H_A, is accepted as a result of the analysis. Each measurement consists of 300 samples. MER values are shown in Table 8.5. For other bit rates, see Figure D.1 in Appendix.

Table 8.5: Overview of MER values (dB) for all types of nozzles and precipitations, $B = 10$ Mbps.

	R (mm/h)	64	80	120	144
90B1FP3	$\bar{M}$	15.5	13.7	13.0	13.0
	s_M	1.6	1.2	0.8	0.7
90B1FP3.5	$\bar{M}$	16.4	14.8	13.2	12.8
	s_M	1.9	1.5	1.0	0.8
90B2FP6.5	$\bar{M}$	20.5	18.3	14.5	14.0
	s_M	3.2	2.6	1.8	1.5

Droplet size dependence on MER

In some cases, null hypothesis of normality of MER values was rejected at the confidence level 0.05 based on Shapiro-Wilk test (Table 8.6).

According to Kruskal-Wallis test, the type of rain (droplet size) affects significantly the resulting MER values. All groups are statistically significantly different, except for 90B1FP3 and 90B1FP3.5 for $R = 120$ mm/h. It should be noted that outliers were not removed and had an effect on the result normality of data. Graphical representation of data for the example condition can be seen in Figure 8.7 and 8.8.

Table 8.6: P-values of Shapiro-Wilk normality test for MER with variance tests, $B = 10$ Mbps (Droplet size dependence).

	Rain rate R (mm/h)			
Nozzle	63	80	120	144
90B1FP3	< 0.001	< 0.001	0.055	0.115
90B1FP3.5	0.04	< 0.001	0.064	0.006
90B2FP6.5	< 0.001	< 0.001	< 0.001	0.034
Kruskal-Wallis test	< 0.001	< 0.001	< 0.001	< 0.001

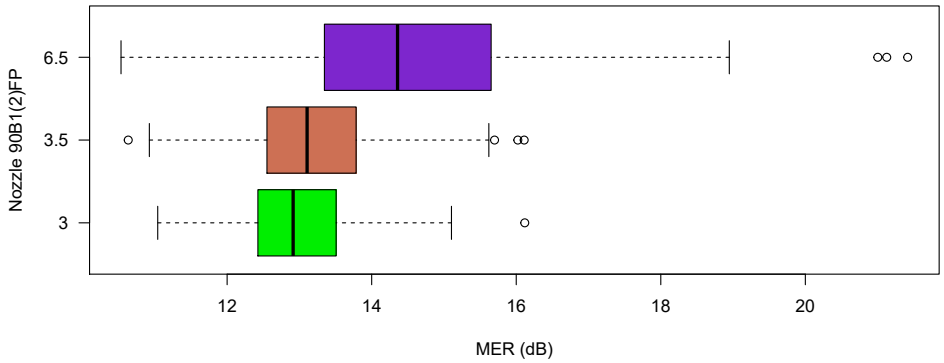

Figure 8.7: MER for $R = 120$ mm/h, $B = 10$ Mbps.

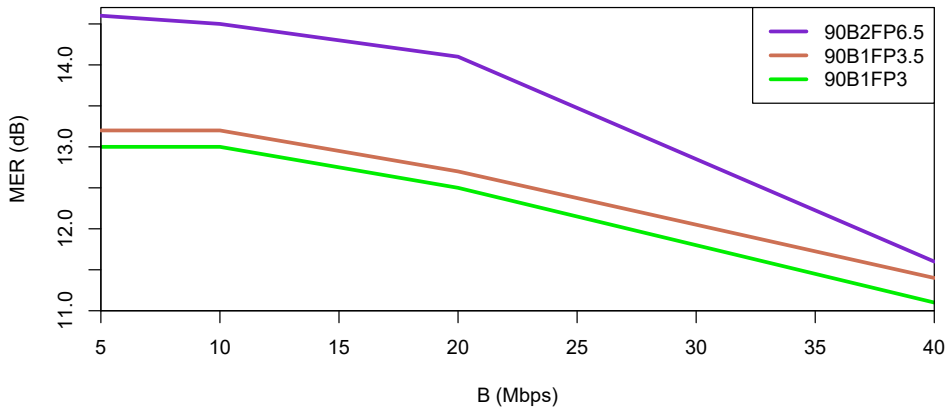

Figure 8.8: MER dependence on bit rate for all nozzles, $R = 120$ mm/h.

Rain rate dependence on MER

In some cases, null hypothesis of normality of MER values was rejected at the confidence level 0.05 based on Shapiro-Wilk test (Table 8.7).

Table 8.7: P-values of Shapiro-Wilk normality test for MER with variance tests, $B = 10$ Mbps (rain rate dependence).

	Nozzle		
Rain rate (mm/h)	90B1FP3	90B1FP3.5	90B2FP6.5
63	< 0.001	0.04	< 0.001
80	< 0.001	< 0.001	< 0.001
120	0.055	0.064	< 0.001
144	0.115	0.006	0.034
Kruskal-Wallis test	< 0.001	< 0.001	< 0.001

According to Kruskal-Wallis test, the intensity of rain affects significantly the resulting MER values. All groups are statistically significantly different, except for $R = 120$ mm/h and $R = 144$ mm/h for 90B1FP3, and $R = 120$ mm/h and $R = 144$ mm/h for 90B1FP6.5. It should be noted that outliers were not removed and had an effect on the result normality of data. Graphical representation of data for the example condition can be seen in Figure 8.9.

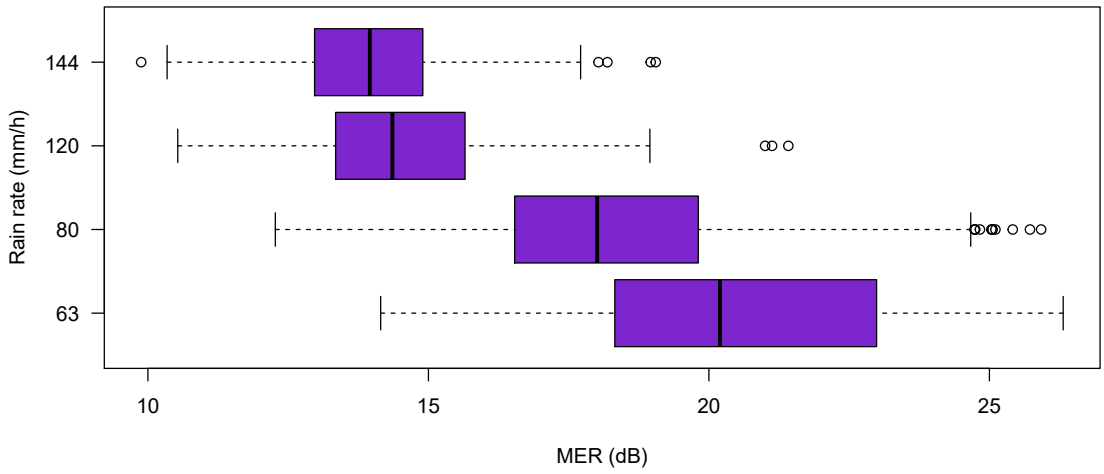

Figure 8.9: MER for 90B1FP6.5, $B = 10$ Mbps.

Bit rate dependence on MER

In some cases, null hypothesis of normality of MER values wes rejected at the confidence level 0.05 based on Shapiro-Wilk test (Table 8.8).

Table 8.8: P-values of Shapiro-Wilk normality test for MER with variance tests, $R = 120$ mm/h.

	Nozzle		
Bit rate (Mbps)	90B1FP3	90B1FP3.5	90B2FP6.5
5	0.186	0.527	0.002
10	0.064	0.055	< 0.001
20	0.044	0.359	0.339
40	0.491	0.870	< 0.001
Kruskal-Wallis test	< 0.001	< 0.001	< 0.001

According to Kruskal-Wallis test, the data bit rate affects significantly the resulting MER values in some cases. All groups are statistically significantly different, except for $B = 5$ Mbps and 10 Mbps for all types of nozzles ($R = 120$ mm/h). It should be noted that outliers were not removed and had an effect on the result normality of data. Graphical representation of data for the example condition can be seen in Figure 8.10 and 8.11.

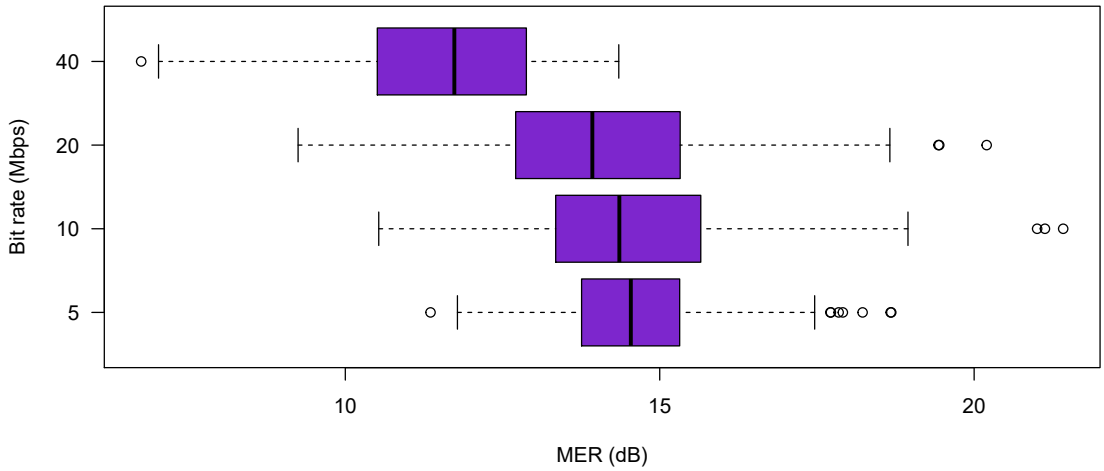

Figure 8.10: MER for 90B1FP6.5, $R = 120$ mm/h.

Visual Evaluation

The evaluation of the results was carried out by assessing the modulation quality diagrams.

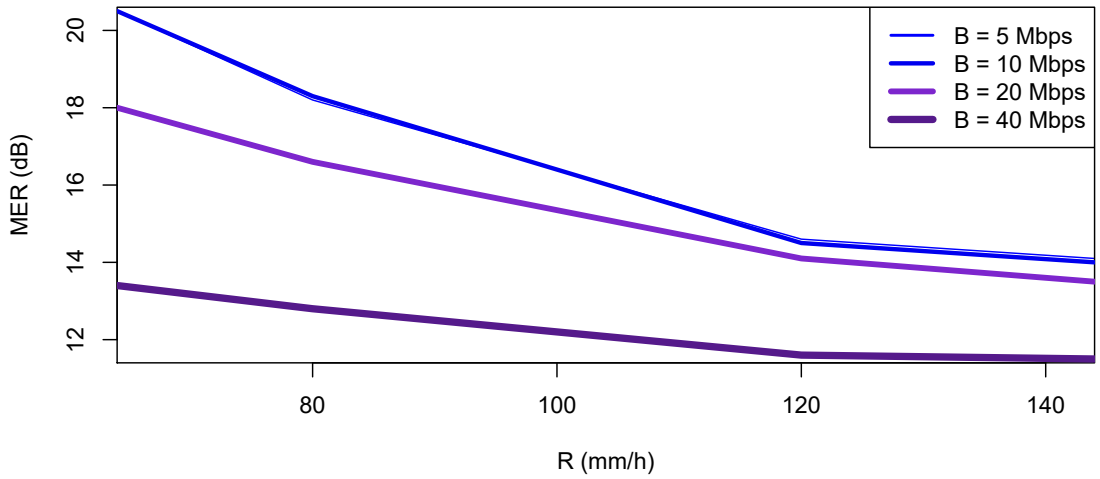

Figure 8.11: MER dependence on rain rate for 90B1FP6.5.

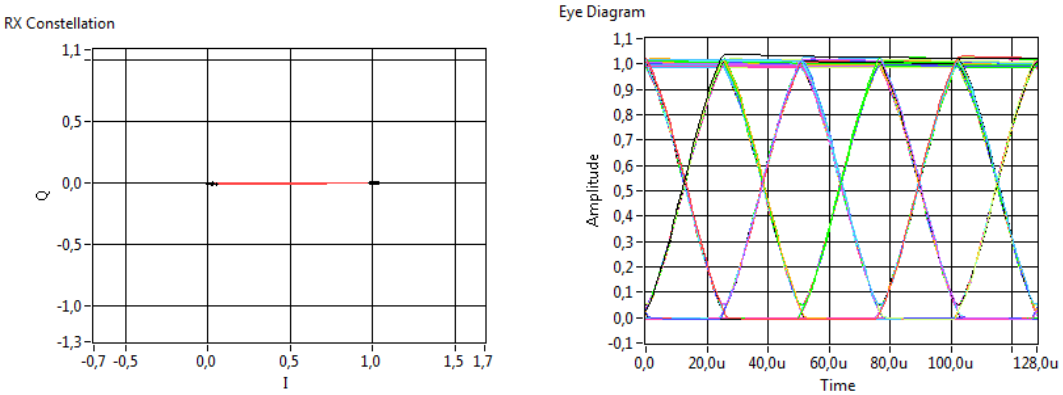

Figure 8.12: Modulation degradation reference, $R = 0$ mm/h, $B = 10$ Mbps.

The reference state in Figure 8.12 can be compared with the state for 90B1FP6.5, $R = 120$ mm/h, $B = 10$ Mbps in Figure 8.13 and signal comparison in Figure 8.14. For more graphical representations of data degradation, see Appendix D.

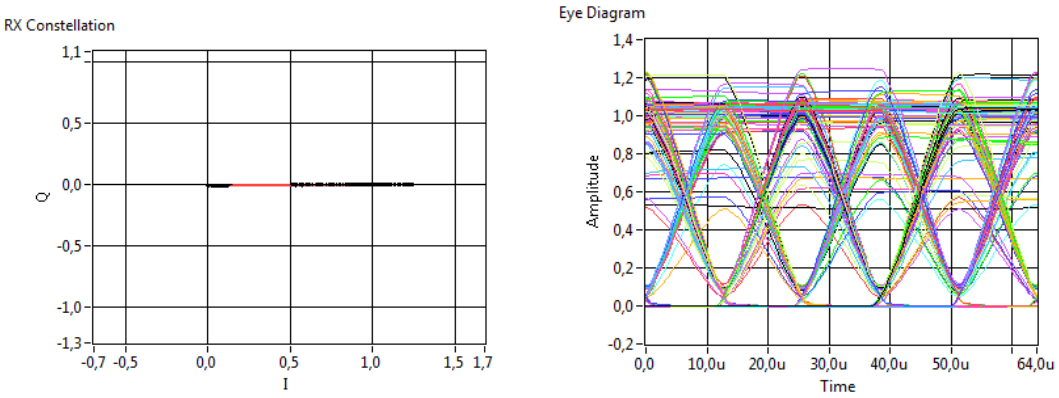

Figure 8.13: Evaluation of modulation degradation for 90B1FP6.5, $R = 120$ mm/h, $B = 10$ Mbps.

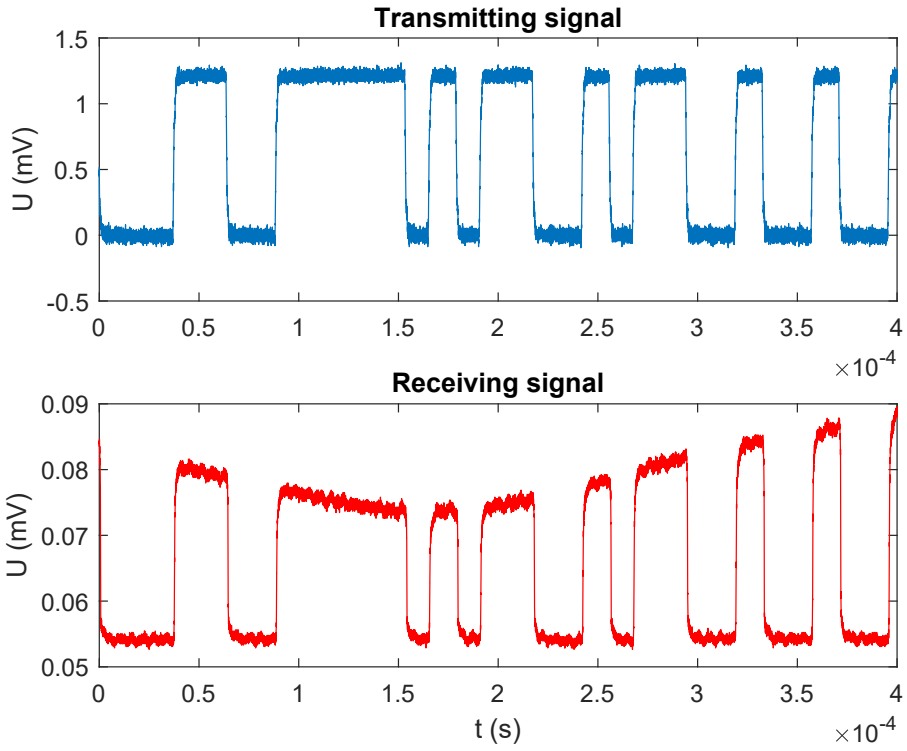

Figure 8.14: Signal degradation, $R = 120$ mm/h by 90B1FP3, $B = 10$ Mbps.

9 Modeling in CFD Simulation Software

This section focuses on modeling approaches related to the computational fluid dynamics (CFD) software. ANSYS Fluent was selected for simulation process for its complexity. Main techniques are going to be explained for this particular software.

9.1 Liquid Spray Description

9.1.1 Droplet Flow

Droplet flow is the gas-liquid flow of discrete fluid droplets in a continuous gas. They are present in a broad range of applications in atmospheric fluid dynamics. Droplet industrial flow examples include absorbers, atomizers, combustors, cryogenic pumping, dryers, evaporation, gas cooling, and scrubbers [21].

In numerical simulations involving liquid–gas flows, according to [23], the Eulerian–Lagrangian method is widely used because of its advantages in predicting turbulent diffusion, droplet breakup, droplet-gas, and droplet–droplet interactions. But the previous chapter about Euler-Lagrange approach describes, this type is used only when particle-particle interactions can be neglected in ANSYS Fluent and if the interaction is needed, it is possible to include Discrete Element Model.

The Euler-Lagrange model employs the Eulerian formulation for the carrier (gas) fluid and the Lagrangian formulation for the dispersed phase (droplets). It is needed to choose an appropriate turbulent model and intensity as well.

9.1.2 Discrete Phase Modeling

Fluent allows simulating a discrete second phase (water droplet in the case) in a Lagrangian frame of reference. This second phase consists of spherical particles dispersed in the continuous phase (an air). ANSYS Fluent computes the trajectories of these discrete phase particles, as well as heat and mass transfer to/from them. The coupling between the phases and its impact on both the discrete phase trajectories and the continuous phase flow can be included too [42].

9.1.3 Primary and Secondary Breakup

According to general descriptions, the flow arising from an injector (nozzle) consists of two (or more) different regions of multi-phase flow.

Figure 9.1 shows the control volume zones of nozzle spray injection with diameter 2.75 mm in which small droplets are formed. The first one, primary breakup zone, where droplets are formed by the breakup of ligaments and mother droplets. Furthermore, in the secondary breakup zone

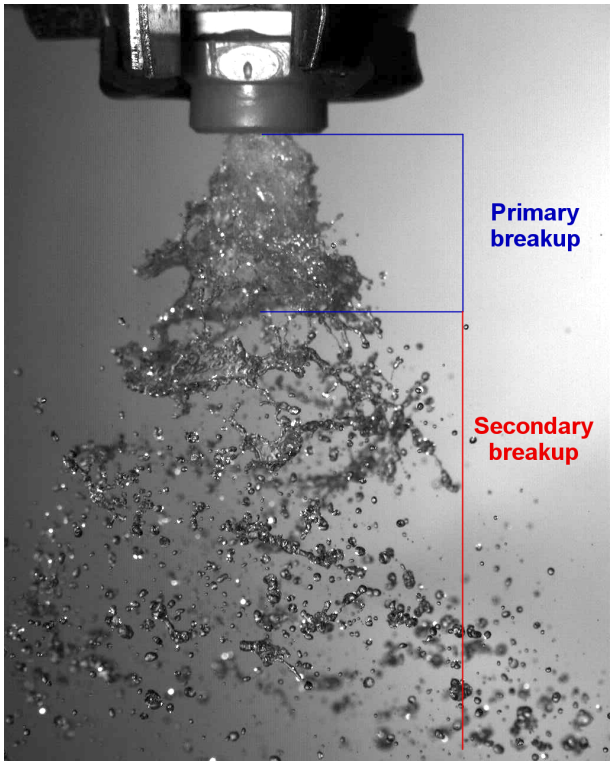

Figure 9.1: Droplet breakup zones.

the phenomena like turbulence and collision affect the formation and distribution of droplets [34]. Types, count and size of these zones depend on the inlet pressure as shown in [35].

The external and internal forces present on the surface of the liquid core create perturbations and oscillations, which can result in the disintegration and breakup of the liquid column into small droplets. This breakup mechanism is referred to as primary. Some defined breakup types can be categorized based on three non-dimensional parameters that include the Weber number, the Reynolds number, and the Ohnesorge number described in Section 7.3 [33].

9.1.3.1 Coupling

Different types of coupling are described in Figure 9.2. One-way coupling refers to models which take into account only the effect of the carrier flowfield at the discrete phase. Two-way coupling is caused by the interaction between the two phases is mutual – the carrier phase influences the dispersion and preferential accumulation of the droplets, which in turn modulate the carrier flowfield. In a more detailed model, however, in addition to the coupling between the carrier fluid and droplets, the droplet-droplet interactions and interactions (such as collisions) should be considered, as the situation prevails in conditions with high loading density of droplets, such

as dense sprays. This is referred to as the four-way coupling in the modeling of multiphase fluid dynamics [23].

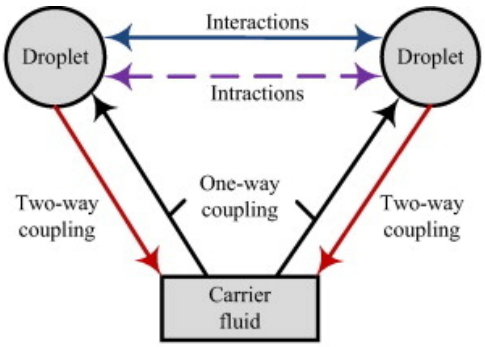

Figure 9.2: Particle coupling.

9.2 Implementation in ANSYS Fluent

Software Ansys FLUENT 18.2 was selected for simulation purposes. According to official websites [36], the software is the most-powerful computational fluid dynamics (CFD) tool available, including well-validated physical modeling capabilities to deliver fast, accurate results across the widest range of CFD and multiphysics applications. It contains the broad physical modeling capabilities needed to model flow, turbulence, heat transfer, and reactions for industrial applications.

ANSYS offers a free academic version for study purposes. The only limitation of this version is the number of cells to 512 000 generated in a mesh (discussed in Section 9.2.4). Due to this limitation, it was decided to model only one lab box to keep sufficient level of the mesh quality, in other words, to keep the mesh dense as much as possible.

9.2.1 Input Hypothesis and Parameters

Simulations were executed for most extreme available conditions (full flow rate given by water pump).

To prove turbulent flow, calculation of Reynolds number was needed. For standard air with temperature 22 °C is $\mu_f = 1.8301 \cdot 10^{-5}$ kg/m ·s, $\rho_g = 1.1965$ kg/m^3, estimated mean droplet diameter $d = 0.001$ m and $V_n = 1.97$ m/s (V_n calculated for water flow in pipe with diameter 0.0025 mm and mass flow rate $Q = 7$ l/min):

$$Re = \frac{dV_n\rho_g}{\mu_f} = \frac{0.001 \cdot 1.97 \cdot 1.1965}{1.8301 \cdot 10^{-5}} \approx 129 \tag{9.1}$$

According to [42], if *Re* is between 1 and 1000, it is in the transition regime. The estimated turbulent intensity is approximately 1%.

Available parameters include:

- Box dimensions including hydraulic diameter.
- Flow rate with a need to be recalculated to proper units.
- Water pressure.
- Cone angle.
- Water droplet size range.

9.2.2 Environment

In a general point of view, Fluent is launched via Workbench environment. It is a general tool used not only for Fluent computing but for a wide range of components. Working with Workbench is based on analysis systems dropped to a virtual desktop. One of the *Fluid Flow (Fluent)* system is shown in Figure 9.3. To obtain results, all previous steps is necessary to accomplish, namely **making up geometry**, **meshing**, **setting up a solution**, and **evaluating results**.

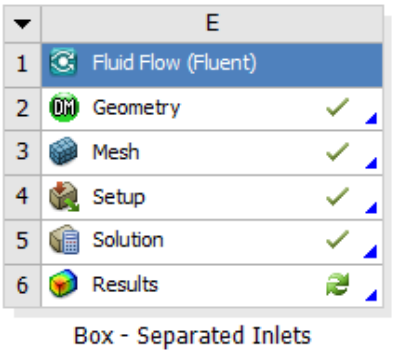

Figure 9.3: Fluid Flow (Fluent) analysis system.

9.2.3 Creating Geometry

Software *Design Modeler* as the part of Workbench is used for creating the simulation geometry. Obvious parameters needed to create an appropriate model is dimensions of the box and coordinates of water nozzles in the box. The next step was to define a shape of spreading of water droplets. Taking photographs by the high-speed camera (See Section 8.2) helped to estimate the cone angle (approximately 60° for 90B2FP6.5 nozzle as seen in Figure 9.4). Finally, the total volume of spray injection is a unite of three cone bodies intersected with box block body.

Boolean operation and Extrude tool were the main steps taken in geometry creating. The final result is shown in Figure 9.5.

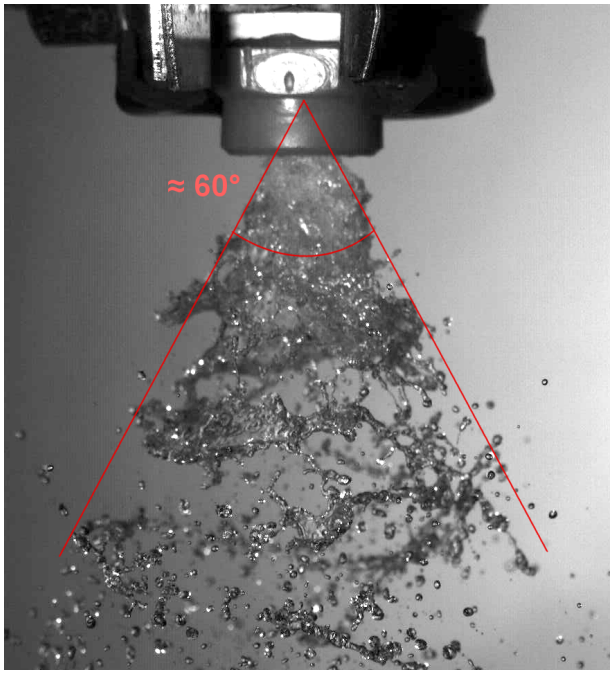

Figure 9.4: Detailed view of the spray angle.

The reason for creating and defining the influenced area is adjusting the different mesh properties for each body created in geometry. The area of spray injection can be set with a high number of computing cells.

9.2.4 Generating Mesh

For the precise calculation and simulation, a mesh with the high density should be made up for each generated body in the previous step, and *Meshing* tool is used. The important step in meshing is choosing so-called *Named Selections*, used as the computational geometric part in Setup.

As already mentioned, cell limit in the academic version of the software gives an obstacle to creating a high-density mesh. On the other hand, more cells consume more computational time. The high density was applied on the influenced area (unite of cones). The model uses tetrahedral cell shape. Final mesh contains around 511 000 cells (see Figure 9.6 and 9.7 with named selections).

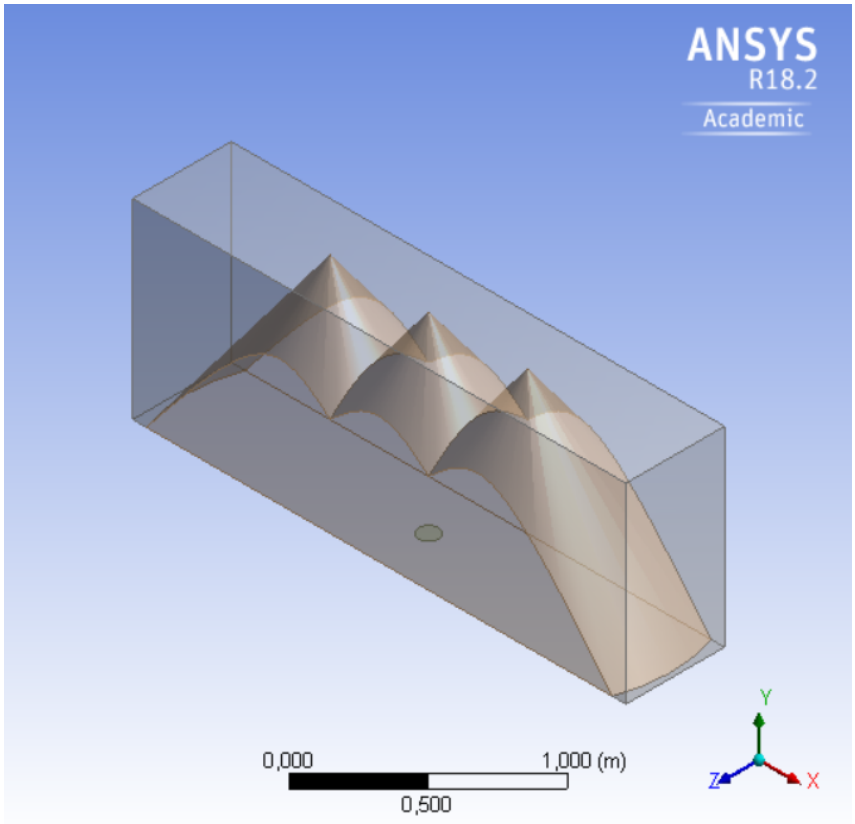

Figure 9.5: Box geometry.

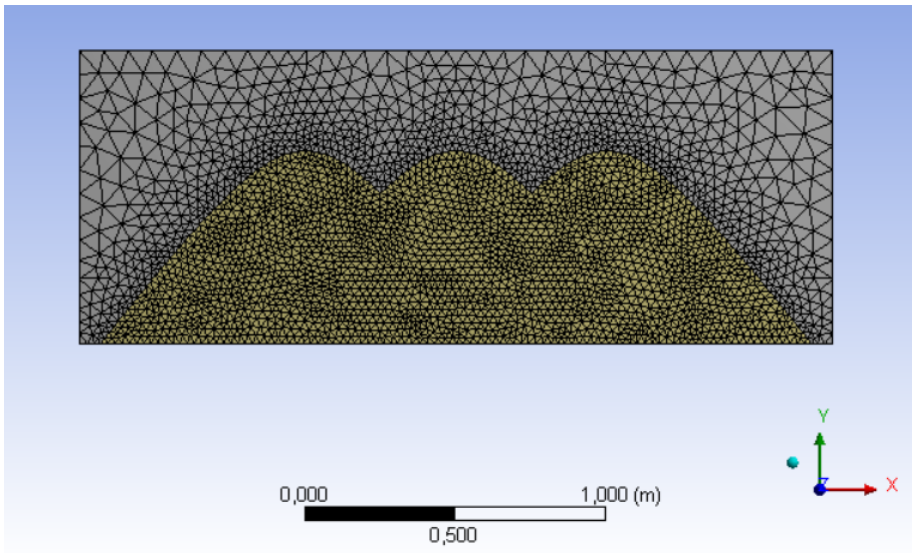

Figure 9.6: Box mesh - front view.

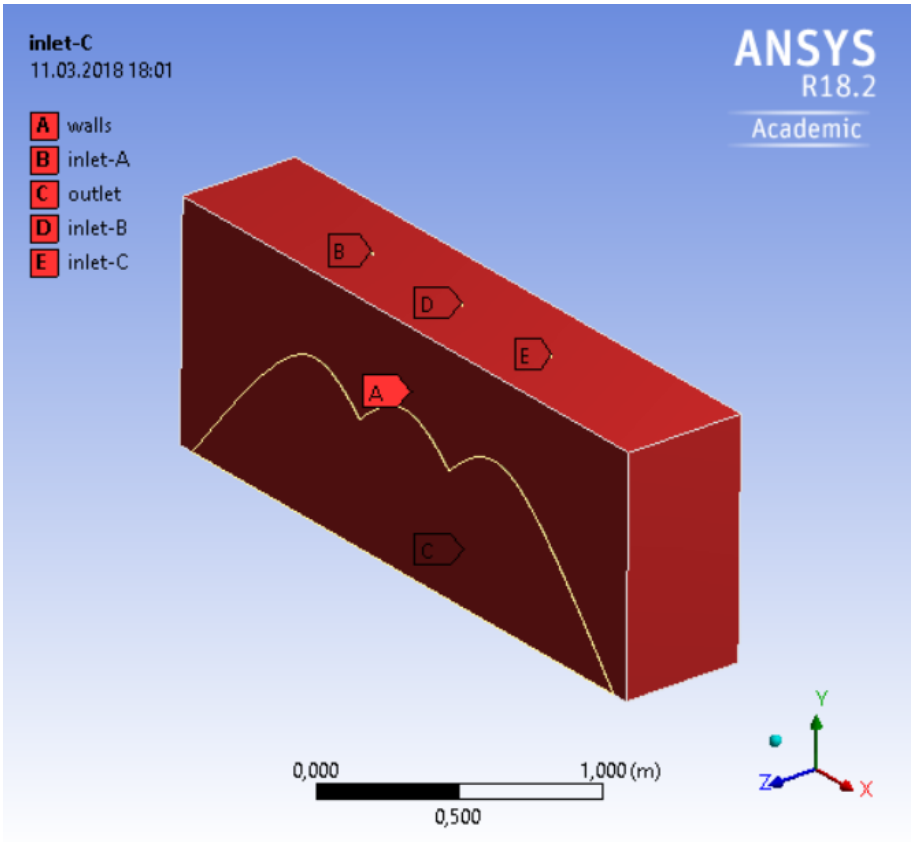

Figure 9.7: Named selections in box.

9.2.5 Setup - Boundary Conditions Specification

Defining multi-phase flow starts in Setup (Fluent computational part). Named selection defined in meshing are transformed into Boundary Specification. It enables to set up many input properties for inlets, outlets, and walls.

For walls, it is important to define the behavior of discrete phase particles while interaction with walls. For given models, it can be distinguished between **trap** and **reflect** model, where the first one "catches" particles at the given position and stops a calculation of the trajectory. The reflect model works like a mirror since all particles are rebound back to free space (continuous phase).

Boundary conditions consist of three inlet orifices as well. These inlets define continuous phase (one of the phase the in multi-phase model). The velocity and direction of phase propagation has to be defined.

9.2.6 Setup - Discrete Model Defining

9.2.6.1 Injection Type Selection

The software offers several injection types for a discrete phase modeling. The goal was to choose to right one(s) to fit our needs. The most important models for the spray/nozzle injection are grouped into:

- cone (point, hollow, ring, solid),
- plain orifice atomizer,
- pressure swirl atomizer,
- air blast atomizer.

Each of these models offers different input parameters. Individual cone types are shown in Figure 9.8.

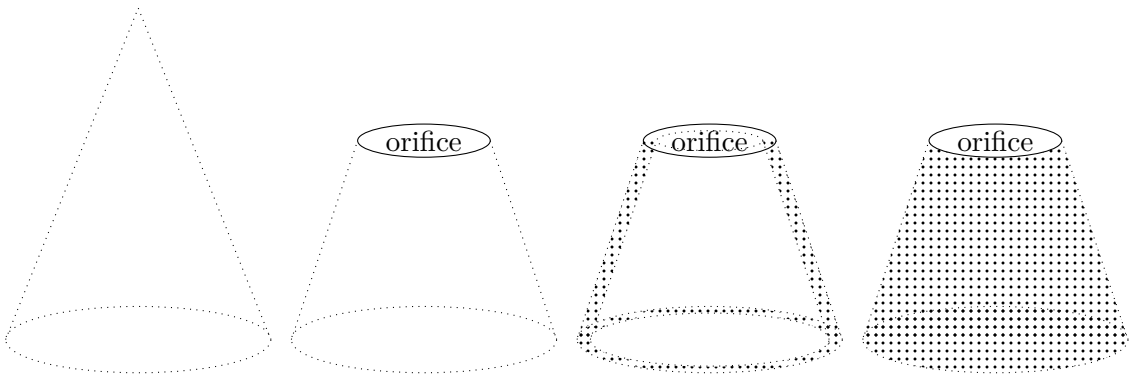

Figure 9.8: Cone injection types.

The selection of the proper combination of injection types is a key to solve the simulation. Nozzle description available in datasheet [31] and photographs captured by a high-speed camera are in a mutual conflict. By the datasheet, the nozzle generates a full cone shape distribution of droplets. It is difficult to make a decision for nozzles with a small orifice (90B1FP1/3/3.5) due to a markable swirl caused by an inner geometry of the nozzle and the high density of droplets. But it is obvious that droplets are distributed along the cone shell in case of 90B2FP6.5 type (see Figure 9.4). Anyway, based on this observation, the final solution of used injection type is ***pressure swirl atomizer***, which fit the given nozzle the best. Cone injections are not suitable for this application since they generate droplets of fixed diameter. By ANSYS Theory Guide [21], the droplets must be randomly distributed for realistic atomizer simulations, both spatially through a dispersion angle and in their time of release. For nonatomizer types of injections in ANSYS Fluent, all of the droplets are released along fixed trajectories at the beginning of the

time step. The atomizer models use stochastic trajectory selection and staggering to attain a random distribution.

9.2.6.2 Pressure Swirl Atomizer

This type of atomizer accelerates the liquid through nozzles known as swirl ports into a central swirl chamber. The swirling liquid pushes against the walls of the swirl chamber. It then emerges from the orifice as a thinning sheet, which is unstable, breaking up into ligaments and droplets. The pressure-swirl atomizer is very widely used for liquid-fuel combustion in gas turbines, oil furnaces, etc. The transition from internal injector flow to fully-developed spray can be divided into three steps: film formation, sheet breakup, and atomization.

The pressure-swirl atomizer model used in ANSYS Fluent is called the Linearized Instability Sheet Atomization (LISA) model of Schmidt et al. The LISA model is divided into two stages: film formation and sheet breakup and atomization. For further information about the used model, see ANSYS Fluent Theory Guide [21].

Spray Half Angle and Atomizer Dispersion Angle

The meaning of these parameters is shown in the Figures 9.9 and 9.10 in ANSYS Fluent, where $\delta_1 = 30°$ is half angle (the orange arrows), and $\delta_2 = 30°$ is the dispersion angle (the pink arrows). The colorful vectors play only a helping role in a setup preparation, as can be seen in results, the distribution does not take place strictly between these two angles.

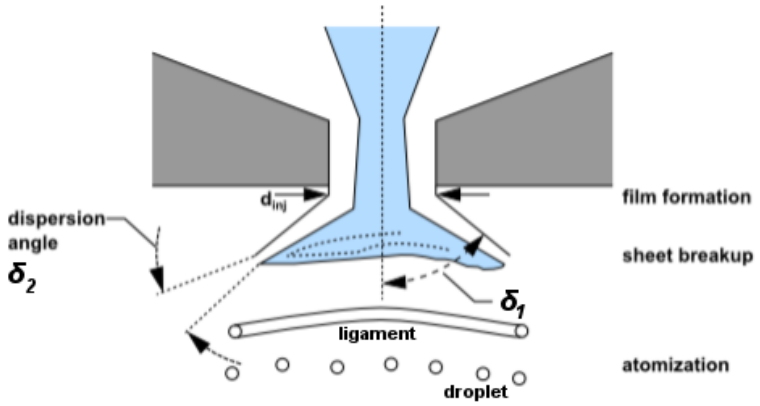

Figure 9.9: Atomization in pressure swirl atomizer, edited [21].

In the case of the use of the selected atomizer, the problem of the distribution of water droplets has to be solved, since at least 90B2FP6.5 nozzle does not generate a full cone shape. Partial simulations with different input angles have provided a closer understanding of the droplet distribution as seen in Figure 9.11. As the angle difference increases, the droplets spread to larger volumes in space.

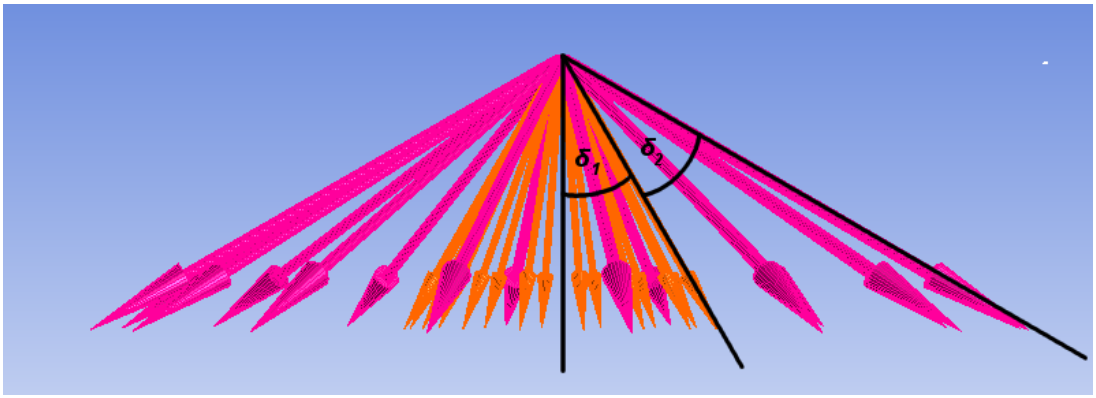

Figure 9.10: Spray Half Angle and Atomizer Dispersion Angle visual definition.

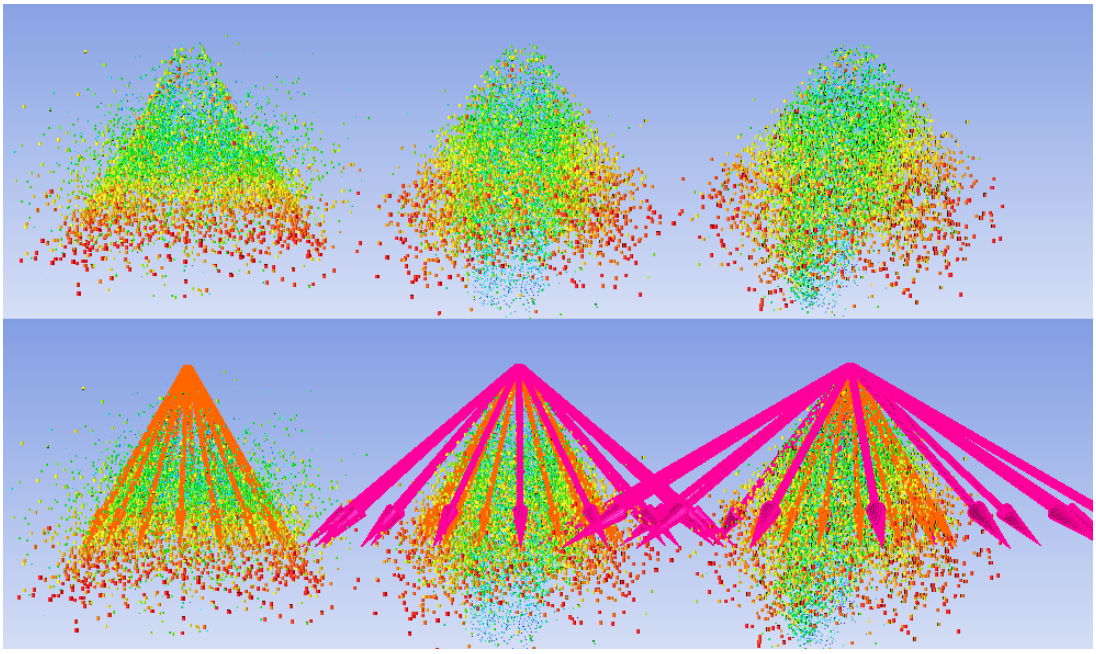

Figure 9.11: Droplet simulation for $\delta_2 = 0°, 20°, 30°$ for $\delta_1 = 30°$.

Another approach - if the nozzle generated full cone as specifications says, it would be necessary to spread distribution. The observation provided a key to the solution - a double value of Atomizer Dispersion Angle was set ($\delta_2 = 60°$), and Spray Half Angle $\delta_1 = 0°$ (see Figure 9.12). It was found out that the droplet distribution in simulation takes place approximately only in a half of δ_2 area. The final dispersion area covers 60° ($\delta_3 = 30°$). For used nozzles, this approach is not used and both of the angles can be set with measured values ($\delta_1 = 30°$, $\delta_2 = 0°$).

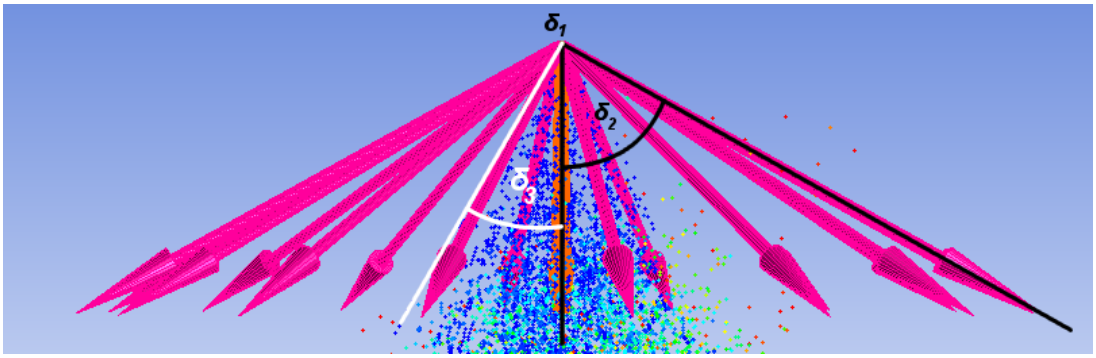

Figure 9.12: Solution of injection with $\delta_1 = 0°$ and $\delta_2 = 60°$ with full cone dispersion.

Flow Rate

To calculate the mass flow, it was necessary to determine the value from the flowmeter and calculate the value for one nozzle by the respective operations. For instance, 8.33 l/min was measured by a flow simulation for one box with FP90B2FP6.5 nozzles attached. For mass flow rate, this value is 0.04628 kg/s for each nozzle.

Upstream Pressure

Pressure gauge B+B Thermo-Technik DRTR-AL-10V-R10B was used to get the value of water pressure near the nozzle. Measured values were used for simulation purposes.

9.2.6.3 Breakup and Coalescence

Fluent also offers setup for the secondary breakup. The TAB model is mostly used for low Weber numbers. The wave model is recommended for Weber numbers greater than 100 [21]. KHRT and the SSD models are also available. Coalescence of discrete water particles can be set as well for each injection defined in the model.

9.2.6.4 Other Parameters

An essential part of each simulation is to set the number of iterations and its time interval. Depending on the iteration count, the number of DPM injections is defined.

9.3 Results

To speed up the calculation process at the beginning, simulations were generated only for 30° part at the beginning of simulation process by View setup multiplied by 12 around Y axis of an inlet. This cannot be done for the simulation of all of three nozzles, since breakup and coalescence phenomena would not be taken into account.

9.3.1 Nozzle Changing

When changing the nozzle it is necessary to modify the model to suit the new conditions. First of all, it will be the hydraulic diameter defined in the injection. Changing the nozzle changes the pressure and water flow, too. These empirical findings must also be applied to the model. For consistent simulation, adjusting the geometry, thus setting a new angle for the cone, would be appropriate. In Figure 9.13, simulation for the nozzle with the largest diameter is presented.

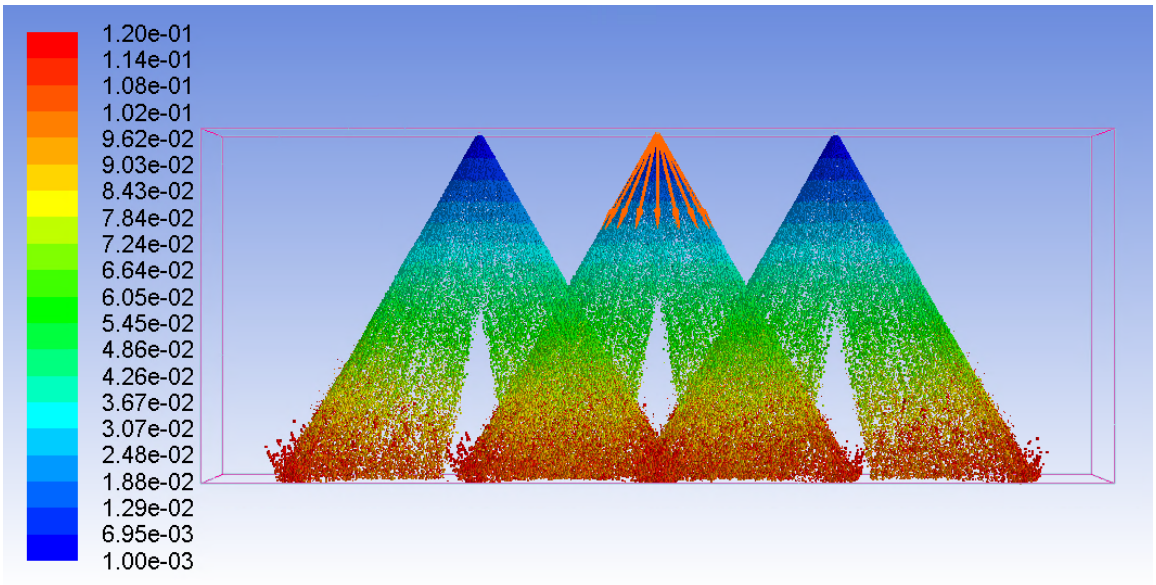

Figure 9.13: Simulation colored by residence time (s) for 90B2FP6.5.

Several tests were done for a reduced low rate. From the empirical point of view, collapse of the model took place, a cone character of the rain was replaced by a "shower". This was not fully proofed by the mathematical model.

Summarization of all important setup parameters of empirical observing for each nozzle is described in Table 9.1

Table 9.1: Setup parameters for nozzles.

Nozzle	90B1FP1	90B1FP3	90B1FP3.5	90B2FP6.5
Half Angle	30°	55°	65°	60°
Dispersion Angle	0°	0°	0°	0°
Injector Inner Diameter (mm)	1	1.5	1.85	2.75
Upstream Pressure (bar)	11.21	6.95	6.17	2.5
Flow Rate (kg/s)	$9.278 \cdot 10^{-3}$	$3.889 \cdot 10^{-2}$	$4.072 \cdot 10^{-2}$	$4.628 \cdot 10^{-2}$

9.3.2 Verification

Based on the nozzle analysis, it can be confirmed that the droplets diameter distribution generated by 90B2FP6.5 most resembles the rain distribution under real atmospheric conditions. In terms of authentic imitation of the actual state of injected droplets, differences can be observed, especially at the nozzle orifice. Based on simulations, the primary breakup area cannot be fully imaged (see Figure 9.14). Although the Pressure swirl atomizer model provides the **ligament constant** and **sheet constant** parameters, on the basis of experiments, the resulting model is inflated to a small extent.

Another significant difference is evident in the density of the generated particles. This effect is affected by the **Number of Streams** parameter.

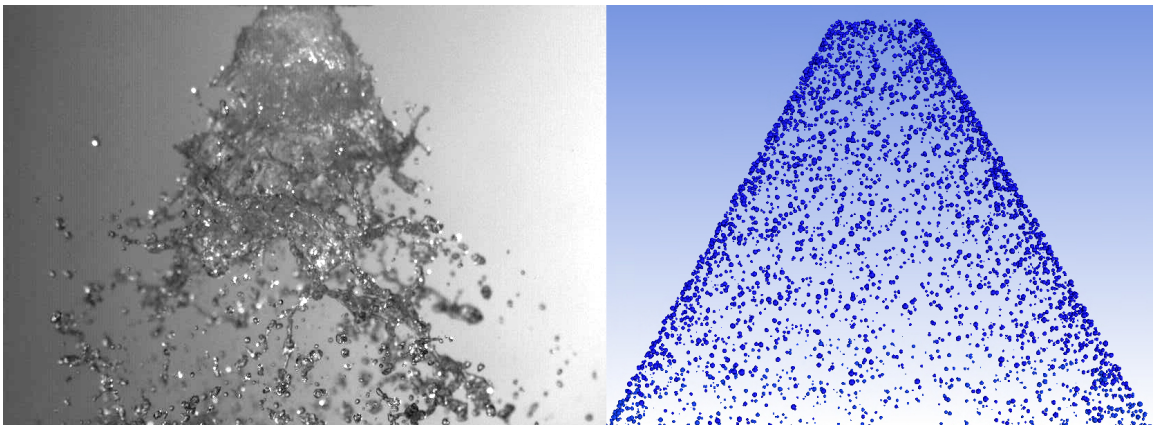

Figure 9.14: Compare of an injection for 90B1FP1 near the orifice.

10 Conclusion

The atmosphere must be understood as an unstable and inhomogeneous environment. Unfavorable and unpredictable effects have to be taken into account in the field of telecommunications. The physical laws in the non-turbulent, as well as rainy conditions for free space optical link has been described.

This work summarizes the knowledge about the creation of a mathematical model of water droplet formation using industrial nozzles. With CFD software, a model describing spray injection with nozzles was successfully created. The basic and most important assumption was to understand multi-phase modeling topic and find a suitable approach and mathematical model describing the injection of water droplets into the gas phase. The Euler-Lagrange approach with the set of pressure swirl atomizers is close to real-world observation. The resulting procedure can be used as a method for solving a similar type of tasks where the discrete phase injection into the free space takes the key role. It should be noted, however, that it is impossible to precisely shape all states of breakup and dispersion of droplets (especially primary breakup) with this model, and the secondary interaction of water droplets on the wall as a boundary condition is not taken into account since the third liquid phase is formed (a film of water). The turbulence played a small influence in this case, as the turbulent flow was not detected (verified) by a numeric assumption.

Models created by simulation are useful but very sensitive to input parameters. For good and credible results, frequent observations of model behavior and eventual parameter adjustments are required. During the creation of this work I came across a model providing the theoretically more feasible simulated environment - (VOF) Volume of Fluid to DPM CFD spray, but available in ANSYS Fluent version 19, which is not accessible in the academic license yet.

When capturing images using a high-speed camera, it was observed that the droplet distribution did not form a full cone as specified by the manufacturer. The droplet distribution formed a hollow cone at high pressure. This fact had to be put into the simulation software. Changing the nozzles affects the resulting model mainly in terms of the orifice size since the large orifice generates large drops more dispersed in the gaseous phase and vice versa. Images were really important for evaluating of droplet size. Based on the observation the right nozzle simulating the real nature conditions could have been chosen as a reference.

This part also included experimental measurement of the free space optical link under the unfavorable influence of water droplets simulating the rainfall. The evaluation was performed in terms of attenuation of the transmitted optical power and degradation of the signal modulation - MER value. Fluctuation of optical intensity captured by LabVIEW software and the oscilloscope is detailed shown in the Appendix D. There are obvious pitches in the receiving power caused by the unsteady distribution of water droplets. Eye diagrams prove quality degradation in high rain

rates too. Besides the not surprising result that the increasing rain rate increases the attenuation value, it has been shown that the droplet size and distribution has a significant effect on the optical beam as well.

The measured results of the attenuation differed from the theoretical values obtained by the calculation using available formulas. These differences could arise due to several factors. The main and the most basic is the assembly of the laboratory environment itself. The critical area has been modeled to mimic realistic natural conditions as faithfully as possible. Here, however, we encounter restrictions on the lab box. In particular, it is the generation of droplets.

Thanks to the photos mentioned above, we could conclude that the realistic droplet size is determined by the nozzle with the largest orifice, but the question is if the size and space distribution is still comparable to real conditions. It is also apparent that droplets injected under high pressure to create greater flow and rain rate are dispersed with higher velocity than in nature. As a result, the beam strikes six water clusters or twelve water walls formed by hollow cones under high pressure.

Another important factor influencing the theoretical calculation of the attenuation itself is the rain rate value. It depends on the area of the box where water drops fall. When the surface is enlarged, the rain rate decreases, resulting in a decrease of the theoretical rain rate value. It is possible, that the real rain rate value is much lower than stated. Using the given assembly and the calculation system (and the assumption of the correct calculation system), we were forced to simulate extreme precipitation values that are not real in Czechia so far, and they are similar to those parts of the world with a high rainfall rate, e. g. Malaysia. For more accurate results, I suggest developing a more sophisticated system for a steady distribution of water droplets.

The OOK as one of the simplest modulations is still devastating to transmitting signal to high rain rates. Bit rate up to 40 Mbps has been achieved with the photodetector and the demodulator set. Modulation was evaluated depending on the used nozzle (droplet size), rain rate and bit rate. The similar results as for attenuation were proven; the increasing rain rate or/and the decreasing droplet size decreases significantly the MER value, proved by the statistical analysis. MER is also decreased with the increased bit rates, but differences in values for low bit rates are not significant from a statistical point of view. For further exploration, comparison with other wavelengths and modulations should be done, since existing research has already proven better architecture efficiency with PPM.

References

[1] NEBULONI, Roberto and Carlo CAPSONI. Effects of Adverse Weather on Free Space Optics. UYSAL, Murat, Carlo CAPSONI, Zabih GHASSEMLOOY, Anthony BOUCOUVALAS and Eszter UDVARY, ed. *Optical Wireless Communications* [ebook]. Cham: Springer International Publishing, 2016, 2016-08-26, s. 47-68 [Accessed 2018-01-21]. Signals and Communication Technology. DOI: 10.1007/978-3-319-30201-0_3. ISBN 978-3-319-30200-3. Available at: http://link.springer.com/10.1007/978-3-319-30201-0_3

[2] Atlas, D., Srivastava, R.C., Sekhon, R.S. . *Droppler radar characteristic of precipitation at vertical incidence*. Rev. Geophys. Space Phys. 2, 1-35, 1973.

[3] Basahel, A., Rafiqul, I. M., Habaebi, M. H., & Suriza, A. Z. (2015). A proposed rain attenuation prediction method for free space optical link based on rain rate statistic. *ARPN Journal of Engineering and Applied Sciences*, 10 (23). Retrieved from http://www.arpnjournals.org/jeas/research_papers/rp_2015/jeas_1215_3175.pdf

[4] Recommendation ITU-R P.530-17: Propagation data and prediction methods required for the design of terrestrial line-of-sight systems [online]. In: Geneva: International Telecommunication Union, 12/2017 [Accessed 2018-01-10]. Available at: https://www.itu.int/dms_pubrec/itu-r/rec/p/R-REC-P.530-17-201712-I!!PDF-E.pdf

[5] WILLIAMS, C. R. and K. S. GAGE. *Raindrop size distribution variability estimated using ensemble statistics* [online]. Univ. Colorado, USA: Cooperative Institute for Research in Environmental Sciences (CIRES), 2009 [cit. 2018-01-11]. Dostupné z: https://www.ann-geophys.net/27/555/2009/angeo-27-555-2009.pdf

[6] Recommendation ITU-R P.1814 (08/07). In: Geneva: International Telecommunication Union. [online]. 2007 [Accessed 2017-11-15]. Available at: https://www.itu.int/dms_pubrec/itu-r/rec/p/R-REC-P.1814-0-200708-I!!PDF-E.pdf

[7] KILLINGER, Dennis K., James H. CHURNSIDE, Laurence S. ROTHMAN. Atmospheric optics. Chapter 3. BASS, Michael et al. *Handbook of optics.* Volume V. 3rd ed. /. New York: McGraw-Hill, 2010. ISBN 978-0-07-163313-0.

[8] VITÁSEK, J. *Optické atmosférické komunikace*. Elektronické skriptum. Ostrava: FEI VŠB-TUO, 2017.

[9] Interactions with the Atmosphere. In: University of Bristol: Student & Staff Interactive Server [online]. [Accessed 2018-12-26]. Available at: http://seis.bris.ac.uk/~ggjlb/teaching/ccrs_tutorial/tutorial/chap1/c1p4e.html

[10] BAYKAL, Yahya Kemal. Optical Propagation in Unguided Media. UYSAL, Murat, Carlo CAPSONI, Zabih GHASSEMLOOY, Anthony BOUCOUVALAS a Eszter UDVARY, ed. *Optical Wireless Communications* [online]. Cham: Springer International Publishing, 2016, 2016-08-26, s. 25-45 [Accessed 2018-01-21]. Signals and Communication Technology. DOI: 10.1007/978-3-319-30201-0_2. ISBN 978-3-319-30200-3. Available at: http://link.springer.com/10.1007/978-3-319-30201-0_2

[11] CARRASCO-CASADO, Alberto, Verónica FERNÁNDEZ and Natalia DENISENKO. Free-Space Quantum Key Distribution. UYSAL, Murat, Carlo CAPSONI, Zabih GHASSEMLOOY, Anthony BOUCOUVALAS and Eszter UDVARY, ed. *Optical Wireless Communications* [ebook]. Cham: Springer International Publishing, 2016, 2016-08-26, s. 589-607 [Accessed 2017-11-18]. Signals and Communication Technology. DOI: 10.1007/978-3-319-30201-0_27. ISBN 978-3-319-30200-3. Available at: http://link.springer.com/10.1007/978-3-319-30201-0_27

[12] Free Space Optical Communications — Theory and Practices - Scientific Figure on ResearchGate [online]. [Accessed 2018-01-05]. Available from: https://www.researchgate.net/figure/Figure-8-Patterns-of-Rayleigh-Mie-and-Non-selective-scattering_268804484_fig7

[13] MAKS, Kolman and Kosec GREGOR. *Attenuation due to liquid water content in the atmosphere* [online]. 2016 [Accessed 2018-02-05]. Available at: http://www-e6.ijs.si/ParallelAndDistributedSystems/MeshlessMachine/wiki/index.php/Attenuation_due_to_liquid_water_content_in_the_atmosphere. Jožef Stefan Institute, Department of Communication Systems, Ljubljana.

[14] FISER, Ondrej and Vladimir BRAZDA. Experimental Validation of FSO Channel Models. UYSAL, Murat, Carlo CAPSONI, Zabih GHASSEMLOOY, Anthony BOUCOUVALAS a Eszter UDVARY, ed. *Optical Wireless Communications* [ebook]. Cham: Springer International Publishing, 2016, 2016-08-26, s. 69-86 [Accessed 2018-01-21]. Signals and Communication Technology. DOI: 10.1007/978-3-319-30201-0_4. ISBN 978-3-319-30200-3. Available at: http://link.springer.com/10.1007/978-3-319-30201-0_4

[15] Recommendation ITU-R P.837-7: Characteristics of precipitation for propagation modelling [online]. In: Geneva: International Telecommunication Union, 06/2017 [Accessed 2018-01-21]. Available at: https://www.itu.int/dms_pubrec/itu-r/rec/p/R-REC-P.837-7-201706-I!!PDF-E.pdf

[16] VAVOULAS, Alexander, Harilaos G. SANDALSDIS and Dimitris VAROUTAS. *Weather Effects on FSO Network Connectivity.* Journal of Optical Communications and Networking. 4. 734-740, 2012. DOI:10.1364/JOCN.4.000734.

[17] PECHAČ, Pavel and Stanislav ZVÁNOVEC. *Základy šíření vln pro plánování pozemních rádiových spojů.* Praha: BEN - technická literatura, 2007. ISBN 978-80-7300-223-7.

[18] SALEH, Bahaa E. A. and Malvin CARL. TEICH. *Fundamentals of photonics.* 2nd ed. Hoboken, N.J.: Wiley Interscience, 2007. ISBN 978-0-471-35832-9.

[19] AVIV, David G. *Laser space communications.* Boston: Artech House, c2006. ISBN 978-1-59693-028-5.

[20] ARNON, Shlomi. *Advanced optical wireless communication systems.* Cambridge: Cambridge University Press, 2012. ISBN 978-0-521-19787-8.

[21] SAS IP, Inc. *ANSYS FLUENT Theory Guide.* Release 18.2. Canonsburg, August 2017. Available from ANSYS web support.

[22] BRENNEN, Christopher E. *Fundamentals of multiphase flow* [online]. New York: Cambridge University Press, 2005 [Accessed 2018-02-20]. ISBN 05-218-4804-0.

[23] KHARE P., Shanwu WANG, and Vigor YANG, *Modeling of finite-size droplets and particles in multiphase flows.* Chinese Journal of Aeronautics, Volume 28, Issue 4, 2015, Pages 974-982, ISSN 1000-9361. DOI: https://doi.org/10.1016/j.cja.2015.05.004. Available at: `http://www.sciencedirect.com/science/article/pii/S1000936115001004`

[24] KOZUBKOVÁ, Milada, Tomáš BLEJCHAŘ and Marian BOJKO. *Modelování přenosu tepla, hmoty a hybnosti: učební text.* Ostrava: VŠB - Technická univerzita Ostrava, 2011. ISBN 978-80-248-2491-8.

[25] CLAYTON T. CROWE. *Multiphase Flow Handbook.* Hoboken: CRC Press, 2005. ISBN 9781420040470.

[26] ALKHOLIDI, Abdulsalam Ghalib and Khaleel Saeed ALTOWIJ. Free Space Optical Communications — Theory and Practices. KHATIB, Mutamed, ed. *Contemporary Issues in Wireless Communications* [online]. InTech, 2014, 2014-11-26 [cit. 2018-02-26]. DOI: 10.5772/58884. ISBN 978-953-51-1732-2. Available at: `http://www.intechopen.com/books/contemporary-issues-in-wireless-communications/free-space-optical-communications-theory-and-practices`

[27] BOUCHET, Olivier. *Free-space optics: propagation and communication.* Newport Beach, CA: ISTE, 2006. ISBN 978-1-905209-02-6.

[28] MAJUMDAR, Arun K. and Jennifer Crider RICKLIN. *Free-space laser communications: principles and advances*. New York, NY: Springer, c2008. ISBN 978-0-387-28652-5.

[29] WILLEBRAND, Heinz. and Baksheesh S. GHUMAN. *Free space optics: enabling optical connectivity in today's networks.* Indianapolis, Ind.: SAMS, c2002. ISBN 0-672-32248-x.

[30] MAJUMDAR, Arun K. *Advanced Free Space Optics (FSO): A Systems Approach*. New York: Springer, 2015. Springer series in optical sciences, v.186. ISBN 978-1-4939-0917-9.

[31] Boomless Flat Fan Nozzles - XT-Boom X Tender - Pentair Hypro [online]. [Accessed 2018-03-05]. Available at: `http://hypro.pentair.com/~/media/websites/fluid%20motion/downloads/catalogs/02-f%20-%20specialty%20spray%20nozzles.pdf`

[32] NI USB-6001: Specifications. National Instruments[online]. Available at: `http://www.ni.com/pdf/manuals/374369a.pdf`

[33] AFSHAR, Ali. *Evaluation of Liquid Fuel Spray Models for Hybrid RANS/LES and DLES Prediction of Turbulent Reactive Flows* [online]. 2014 [Accessed 2018-03-10]. Available at: `https://tspace.library.utoronto.ca/bitstream/1807/68086/1/Afshar_Ali_201411_MAS_thesis.pdf`. University of Toronto.

[34] MOVAHEDNEJAD, Ehsan, Fathollah OMMI and S. Mostafa HOSSEINALIPOUR. *Prediction of Droplet Size and Velocity Distribution in Droplet Formation Region of Liquid Spray*. Entropy [online]. 2010, 12(12), 1484-1498 [Accessed 2018-03-10]. DOI: 10.3390/e12061484. ISSN 1099-4300. Available at: `http://www.mdpi.com/1099-4300/12/6/1484`

[35] BAI, Fuqiang, Qing CHANG, Shixing CHEN, Jinpeng GUO, Kui JIAO and Qing DU. *Experimental investigation on the spray characteristics of power-law fluid in a swirl injector*. Fluid Dynamics Research [online]. 2017, 49(3), 035508- [Accessed 2018-03-10]. DOI: 10.1088/1873-7005/aa6726. ISSN 0169-5983. Dostupné z: `http://stacks.iop.org/1873-7005/49/i=3/a=035508?key=crossref.99197b3f769c42e4358a374d10da7fea`

[36] *ANSYS Fluent Software: CFD Simulation* [online]. [cit. 2018-03-11]. Available at: `https://www.ansys.com/Products/Fluids/ANSYS-Fluent`

[37] Spray Guns and Applicators Information. In: *IEEE GlobalSpec: Engineering360* [online]. [Accessed 2018-03-16]. Available at: `https://www.globalspec.com/learnmore/manufacturing_process_equipment/surface_coating_protection/coating_paint_spray_guns`

[38] FISCHER, Walter. *Digital television: a practical guide for engineers*. New York: Springer, c2004. ISBN 978-3540011552.

[39] PENTTINEN, Jyrki T. J. *The telecommunications handbook: engineering guidelines for fixed, mobile, and satellite systems*. Chichester, West Sussex, United Kingdom: Wiley, 2015. ISBN 9781119944881.

[40] *The TimIQ Synchronization System for Sub-Picosecond Delay Adjustment*. In: ResearchGate [online]. [Accessed 2018-03-17]. Available at: https://www.researchgate.net/publication/322504895_The_TimIQ_Synchronization_System_for_Sub-Picosecond_Delay_Adjustment

[41] *Digital modulation: Phase shift keying(PSK)*. In: Circuit Design, Inc. [online]. [Accessed 2018-03-17]. Available at: http://www.cdt21.com/resources/Modulation/modulation_PSK.asp

[42] SAS IP, Inc. *ANSYS FLUENT User's Guide*. Release 18.2. Canonsburg, August 2017. Available from ANSYS web support.

[43] Recommendation ITU-R P.838–3, R Specific Attenuation Model for Rain for Use in Prediction Methods (2005). In: Geneva: International Telecommunication Union (2005) [Accessed 2018-01-21]. Available at: https://www.itu.int/rec/R-REC-P.838-3-200503-I/en

[44] Ionosphere | NOAA / NWS Space Weather Prediction Center. *National Oceanic and Atmospheric Administration: Space Weather Prediction Center* [online]. [Accessed 2018-03-22]. Available at: https://www.swpc.noaa.gov/phenomena/ionosphere

[45] GAUSSIAN BEAM OPTICS. In: *CVI Laser Optics* [online]. [Accessed 2018-03-22]. Available at: https://www.cvilaseroptics.com/file/general/All_About_Gaussian_Beam_OpticsWEB.pdf

[46] BOUCHAL, Zdeněk. *Svazková optika* [online]. [Accessed 2018-03-22]. Available at: http://optics.upol.cz/userfiles/file/OPT_SO.pdf

[47] KAUSHAL, Hemani. *Free space optical communication*. New York, NY: Springer Berlin Heidelberg, 2016. ISBN 978-81-322-3689-4.

[48] JIA, Zhuanhong, Qinglin ZHU and Faliang AO. Atmospheric Attenuation Analysis in the FSO Link. In: 2006 *International Conference on Communication Technology* [online]. IEEE, 2006, 2006, s. 1-4 [Accessed 2018-03-23]. DOI: 10.1109/ICCT.2006.341919. ISBN 1-4244-0800-8. Available at: http://ieeexplore.ieee.org/document/4146520/

[49] HECHT, Eugene. *Optics*. 4th ed. San Francisco: Addison-Wesley, c2002. ISBN 0-321-18878-0.

[50] *Turbulence Modeling: Introduction to Introduction to ANSYS FLUENT, Lecture 6* [online]. ANSYS, 2010 [Accessed 2018-03-10]. Available at: `http://imechanica.org/files/fluent_13.0_lecture06-turbulence.pdf`

[51] *Aerosol Transport – Inertia: Aerosol Science & Engineering* [online]. University of Florida [Accessed 2018-02-17]. Available at: `https://aerosol.ees.ufl.edu/aerosol_trans/section02.html`

[52] OMOTOSHO, T. V., J. S MANDEEP, M. ABDULLAH and A. T. ADEDIJI. *Distribution of one-minute rain rate in Malaysia derived from TRMM satellite data.* Annales Geophysicae [online]. 2013, 31(11), 2013-2022 [Accessed 2018-03-18]. DOI: 10.5194/angeo-31-2013-2013. ISSN 1432-0576. Available at: `http://www.ann-geophys.net/31/2013/2013/`

[53] KUMAR, Vickal V., Ravinesh C. DEO and Visagaperuman RAMACHANDRAN. *Total rain accumulation and rain-rate analysis for small tropical Pacific islands: a case study of Suva, Fiji.* Atmospheric Science Letters [online]. 2006, 7(3), 53-58 [Accessed 2018-04-01]. DOI: 10.1002/asl.131. ISSN 1530-261X. Available at: `http://doi.wiley.com/10.1002/asl.131`

[54] *Mean Annual Precipitation 1950 - 2000* [online]. In: Water Systems Analysis Group, Complex System Research Center, Institute for the Study of Earth, Oceans and Space, University of New Hampshire, USA [Accessed 2018-04-18]. Available at: `http://atlas.gwsp.org/index.php?option=com_content&task=view&id=94`

[55] ZVANOVEC, S. Diversity Statistics of Free Space Optical Links Affected by Rain. *PIERS ONLINE.* Department of Electromagnetic Field, Czech Technical University in Prague, Czech Republic, 2011, (VOL. 7, NO. 7), 637-640.

[56] AZADEH, Mohammad. *Fiber optics engineering.* New York: Springer, c2009. Optical networks series. ISBN 978-1-4419-0303-7.

[57] *Modulation Error Ratio (MER) and Error Vector Magnitude (EVM)* [online]. In: . [Accessed 2018-04-24]. Available at: `http://www.ni.com/white-paper/3652/en/`

A CD

The appedix includes CD.
Content:

- ANSYS Models
- Camera Images
- Measured Values
  - Data
  - Diagrams

B Lab Box

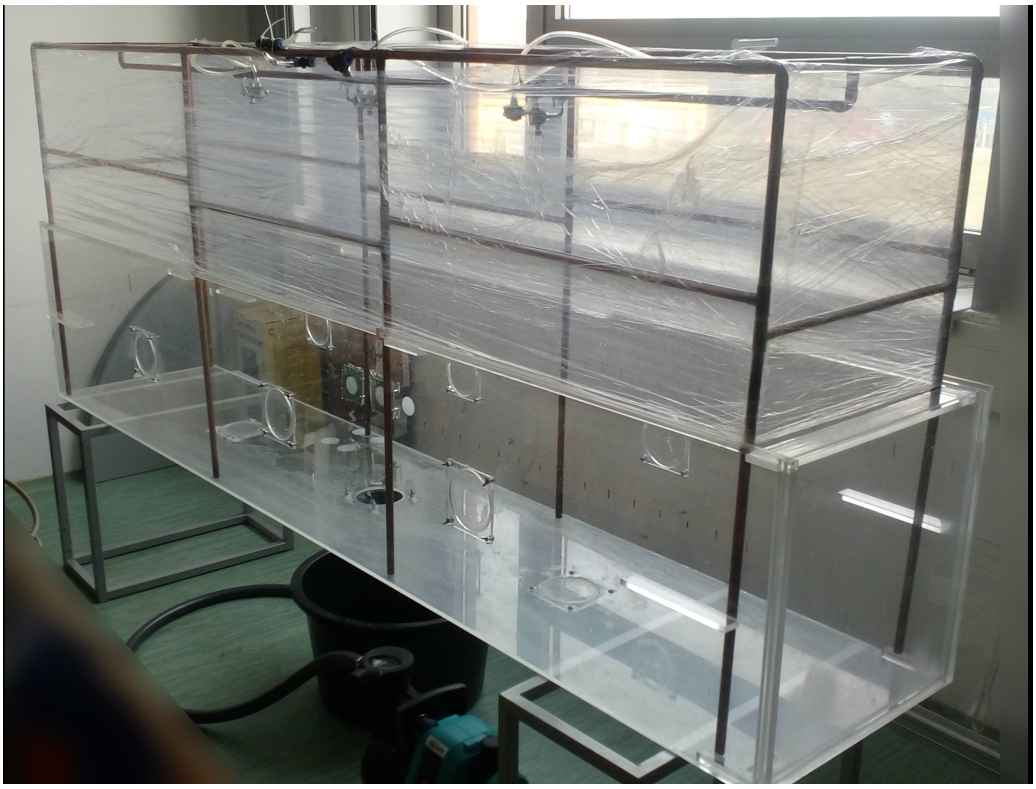

Figure B.1: A half of the lab box.

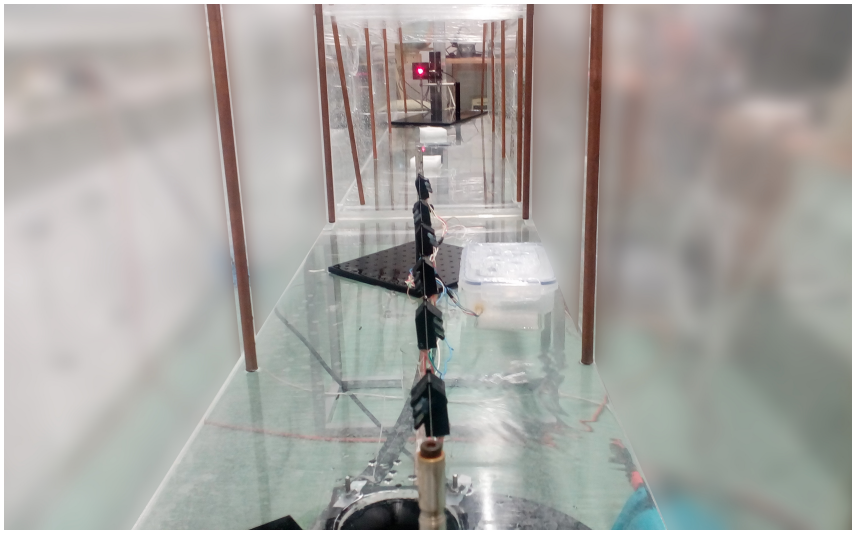

Figure B.2: Optical path inside the box with attached sensor set.

C Control Tools and Used Software

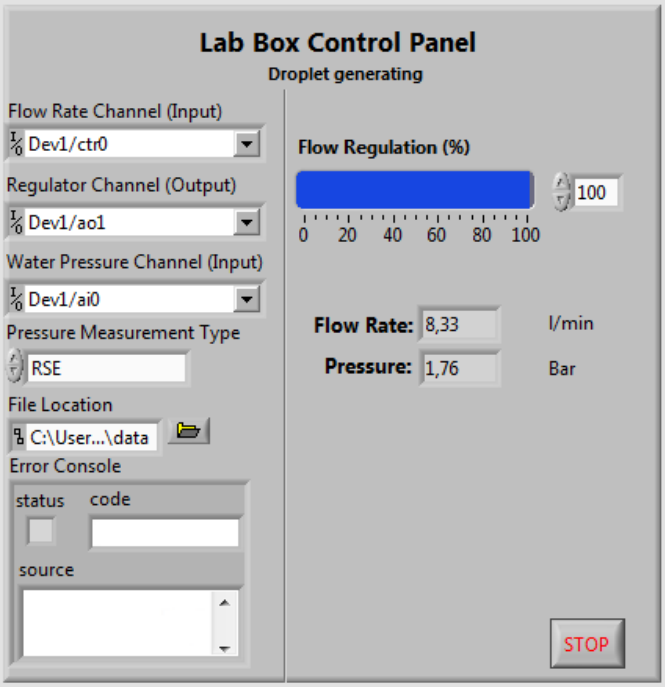

Figure C.1: Control panel for rain generating.

Used software

- ANSYS Fluent 18.2
- FiJi
- GIMP 2.8.20
- National Instruments^{TM} LabVIEW 14
- MATLAB R2017b
- RStudio 1.1.423
- Thorlabs Optical Power Meter Utility 5.9

Used hardware

- Osciloscope LeCroy 204Xi
- Optical detector Thorlabs PDA 10A-EC
- Optical powermeter Thorlabs S120VC
- Windows 7/10 Servers for simulation purposes

D Modulation Comparsion of Signal Degradation

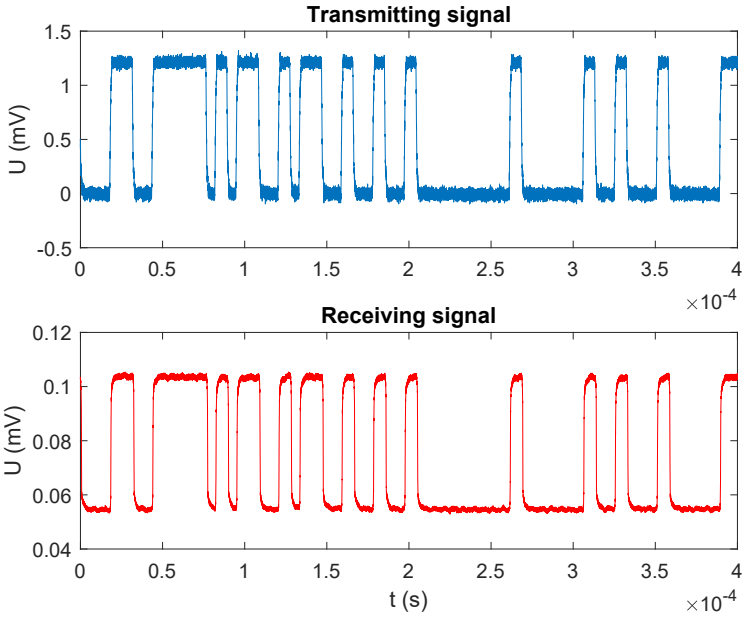

Figure D.1: Signal degradation in rain rate $R = 48$ mm/h by 90B1FP3. Bit rate $B = 20$ Mbps.

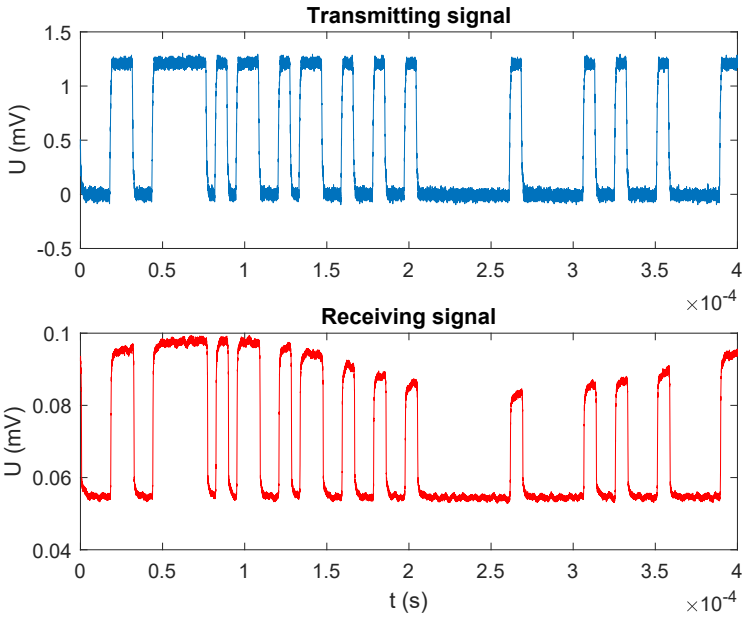

Figure D.2: Signal degradation in rain rate $R = 120$ mm/h by 90B1FP3. Bit rate $B = 20$ Mbps.

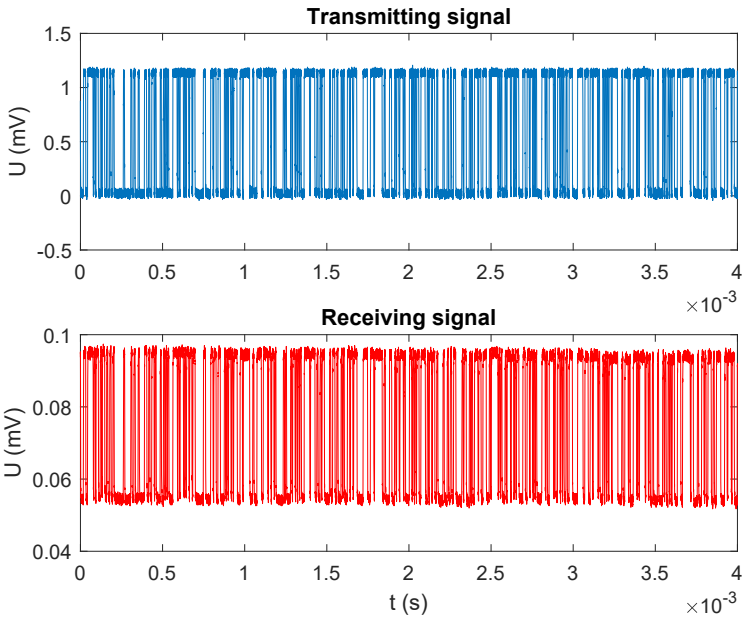

Figure D.3: Signal degradation in rain rate $R = 48$ mm/h by 90B2FP6.5. Bit rate $B = 20$ Mbps.

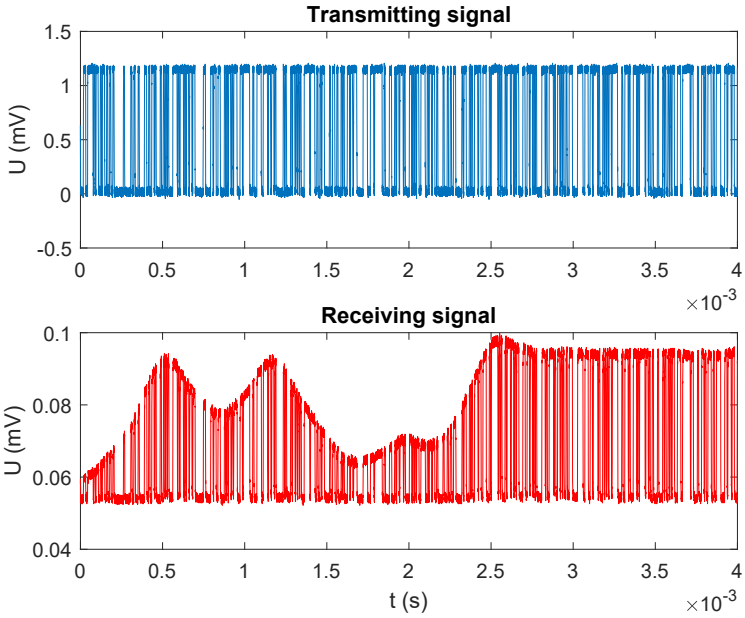

Figure D.4: Signal degradation in rain rate $R = 120$ mm/h by 90B2FP6.5. Bit rate $B = 20$ Mbps.

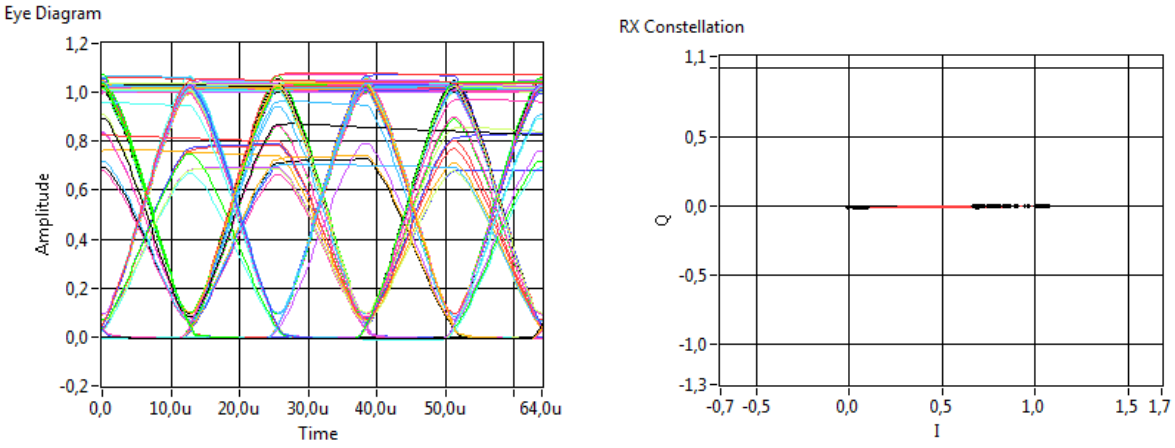

(a) $R = 64$ mm/h

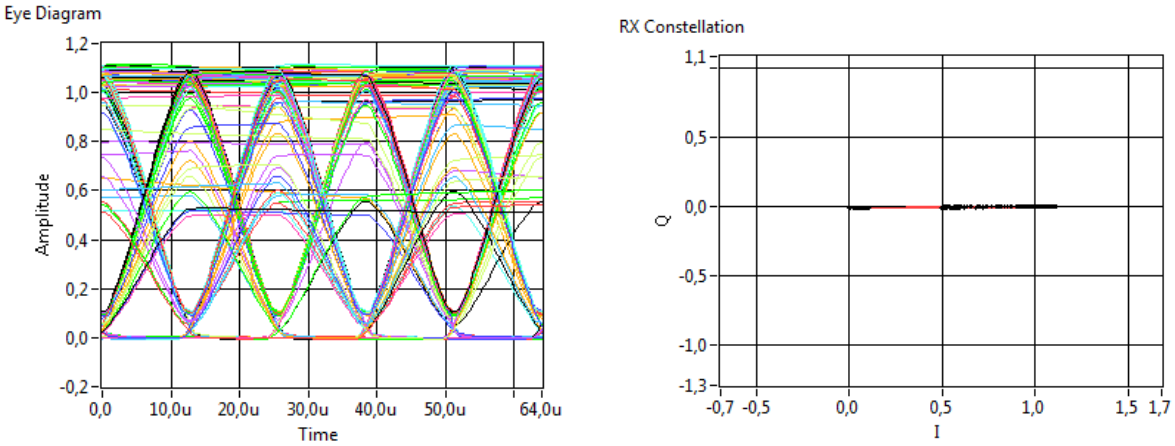

(b) $R = 80$ mm/h

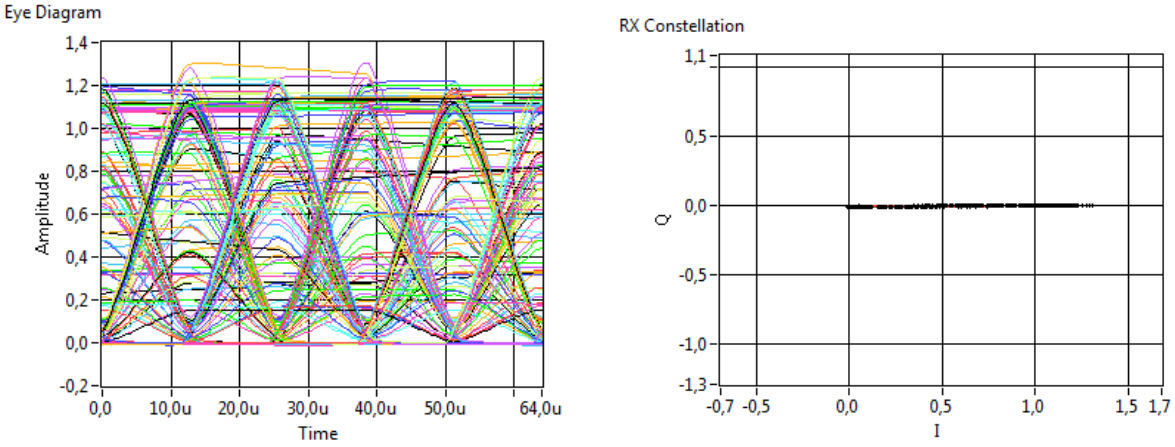

(c) $R = 120$ mm/h

Figure D.5: Eye and I-Q diagrams 90B2FP6.5 for 10 Mbps.

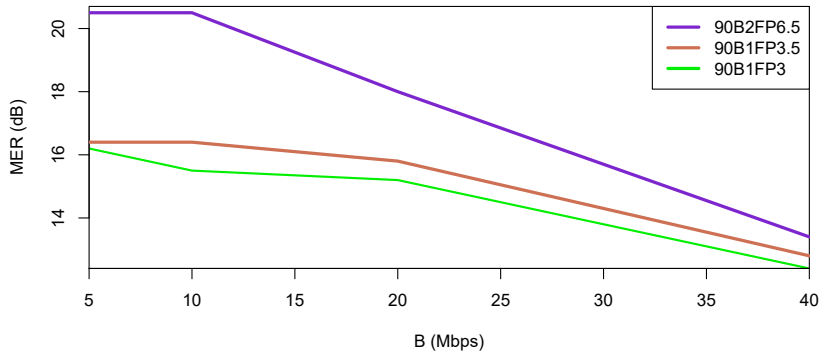

Figure D.6: MER dependence on bit rate, $R = 64$ mm/h.

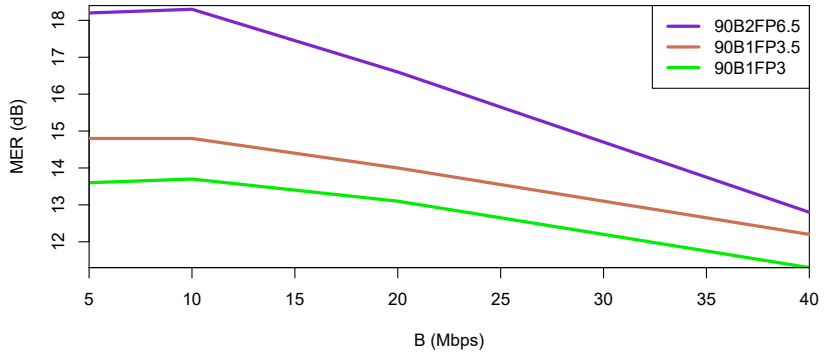

Figure D.7: MER dependence on bit rate, $R = 80$ mm/h.

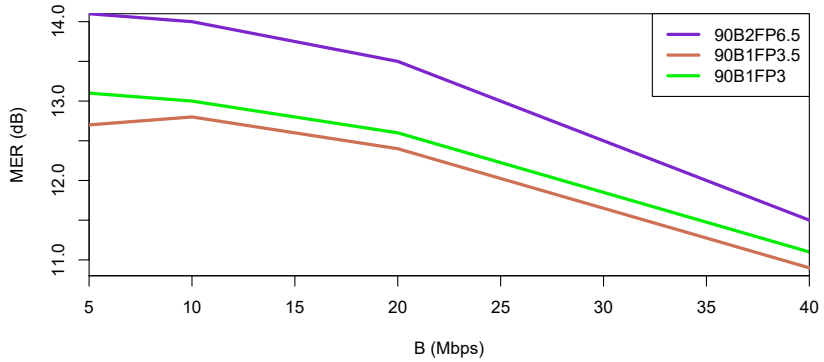

Figure D.8: MER dependence on bit rate, $R = 144$ mm/h.

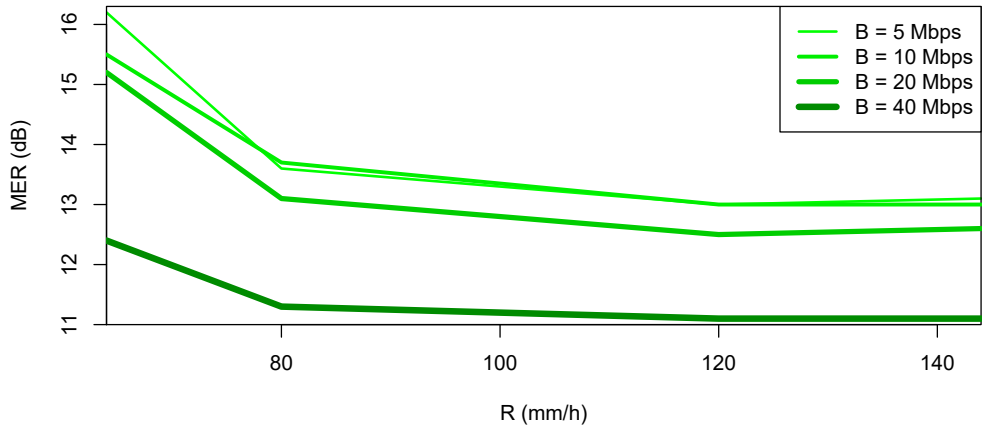

Figure D.9: MER dependence on rain rate for 90B1FP3.

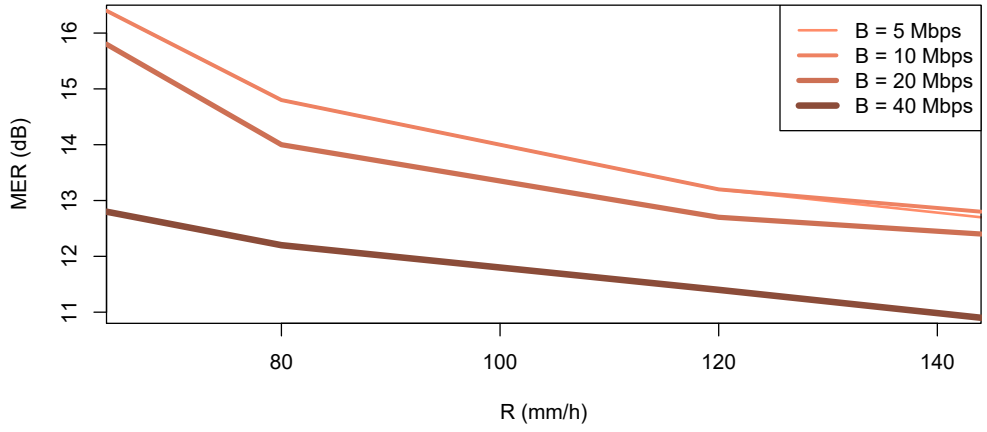

Figure D.10: MER dependence on rain rate for 90B1FP3.5.

Table D.1: Overview of MER values for all types of nozzles and precipitations.

	B (Mbps)	5				10				20				40			
	R (mm/h)	64	80	120	144	64	80	120	144	64	80	120	144	64	80	120	144
90B1FP3	$\bar{M}$	16.2	13.6	13.0	13.1	15.5	13.7	13.0	13.0	15.2	13.1	12.5	12.6	12.4	11.3	11.1	11.1
	s_M	1.2	0.8	0.5	0.6	1,6	1.2	0.8	0.7	2.0	1.4	0.9	1.0	1.4	1.2	0.9	0.8
90B1FP3.5	$\bar{M}$	16.4	14.8	13.2	12.7	16.4	14.8	13.2	12.8	15.8	14.0	12.7	12.4	12.8	12.2	11.4	10.9
	s_M	1.5	1.0	0.7	0.6	1.9	1.5	1.0	0.8	2.4	1.8	1.2	1.0	1.4	1.3	1.1	1.0
90B2FP6.5	$\bar{M}$	20.5	18.2	14.6	14.1	20.5	18.3	14.5	14.0	18.0	16.6	14.1	13.5	13.4	12.8	11.6	11.5
	s_M	2.0	2.0	1.3	1.1	3.2	2.6	1.8	1.5	2.3	2.4	2.0	2.0	1.3	1.6	1.7	1.5

E High-Speed Camera Images

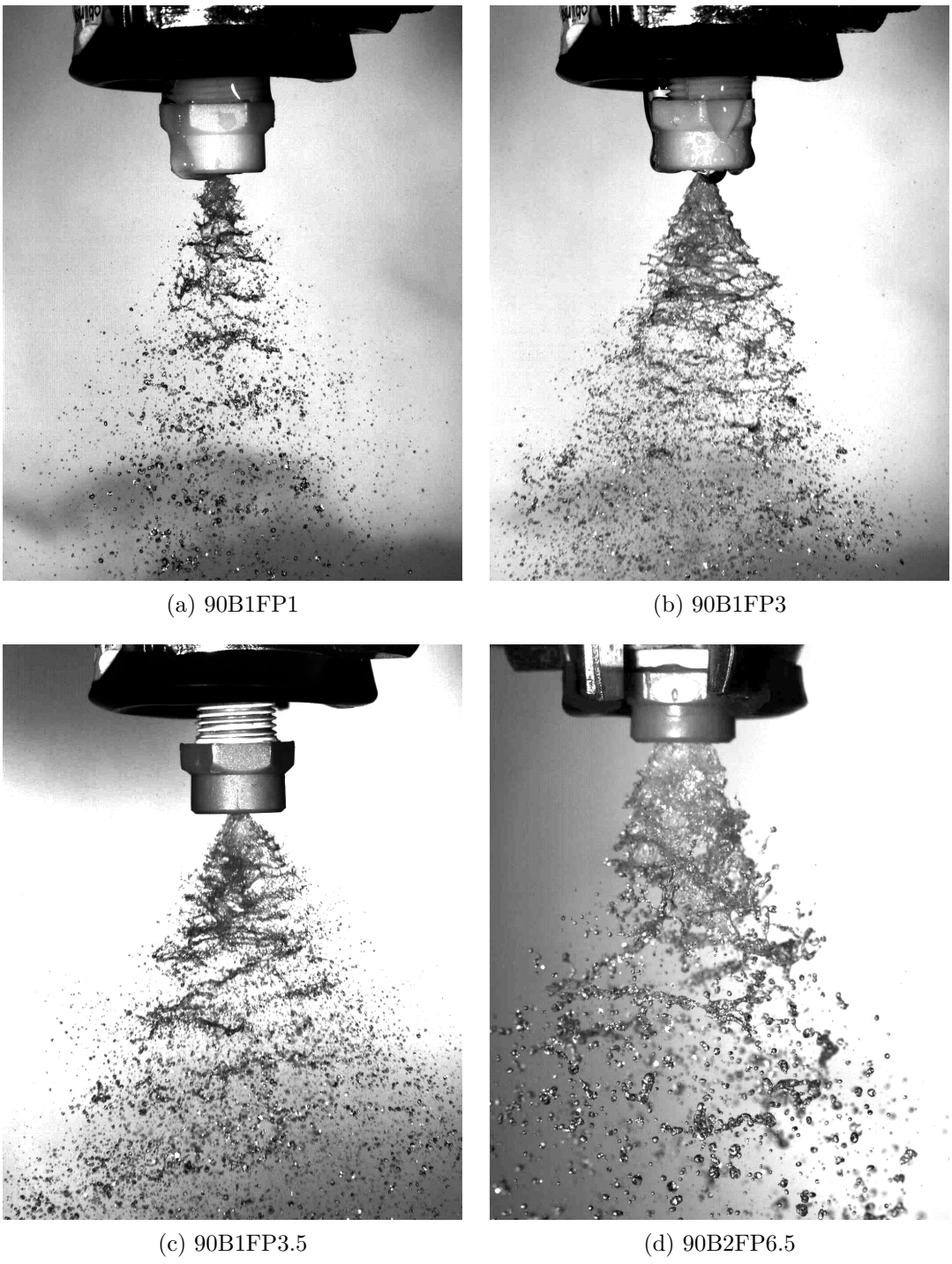

(a) 90B1FP1

(b) 90B1FP3

(c) 90B1FP3.5

(d) 90B2FP6.5

Figure E.1: Droplet injection.